DIRECT CAUSTICIZING OF SODIUM CARBONATE WITH MANGANESE OXIDE

A thesis submitted by

Douglas J. Eames

B.S. 1991, University of Maine, Orono

M.S. 1994, University of California, Berkeley

in partial fulfillment of the requirements

for the degree of Doctor of Philosophy

from the Institute of Paper Science and Technology

Atlanta, Georgia

July 2000

TABLE OF CONTENTS

LIST OF FIGURES

LIST OF TABLES

ABSTRACT

The goal of this thesis was to evaluate manganese oxides as direct causticizing agents for kraft chemical recovery. The primary objective of the research was to develop an understanding of how the rate of reaction between sodium carbonate and manganese oxide is affected by temperature, particle size, and the initial concentration of reactants. A secondary goal was to examine the overall process efficiency of converting sodium carbonate into sodium hydroxide. Another secondary goal was to determine how the direct causticizing reaction is affected by the presence of sodium sulfide.

The reaction kinetics were studied by performing isothermal experiments and monitoring the conversion of the reactants by CO_2 evolution and weight loss. SEM and XRD analysis were used to characterize the reactants and products and verify reaction mechanisms. Reaction products were subjected to hydrolysis to determine overall process efficiencies.

Results show that Mn_3O_4 is the correct manganese oxide for use in direct causticizing. The reaction between Mn_3O_4 and Na_2CO_3 was found to occur with 1:1 stoichiometry. The reaction was well described by the Ginstling-Brounshtein product layer diffusion controlled model with Na_2CO_3 acting as the diffusing species. In the solid state, from 650 – 830 °C, the activation energy is 206 kJ/mol. With molten Na_2CO_3, from 870 – 950 °C, the activation energy is 174 kJ/mol. The transition from solid to molten Na_2CO_3 increases the reaction rate constant by 40 times. An increase in the

Mn_3O_4 particle size reduces the overall reaction rate, while excess Mn_3O_4 in the reaction mixture increases the rate of Na_2CO_3 conversion. Hydrolysis of the direct causticizing product forms a caustic solution. Neither the direct causticizing nor hydrolysis reactions were equilibrium limited. Overall conversions approaching 100% were obtained. Sodium sulfide had a negative impact on the direct causticizing reaction. Na_2S reduced Mn_3O_4 to MnO, an ineffective direct causticizing agent. This also produced Na_2SO_4, an inactive pulping agent.

INTRODUCTION

In kraft chemical pulping processes, the resulting spent liquor contains organics and inorganics. The organic material is recovered for its energy through a combustion process. The inorganic chemicals need to be reclaimed for reuse in the pulping cycle. The inorganics are typically obtained as sodium carbonate and sodium sulfide molten smelt following the combustion of the spent liquor. Further processing of this stream is needed to convert the sodium carbonate into sodium hydroxide, the primary pulping liquor component. Currently this conversion is done with the lime based recovery cycle.

Molten smelt from the recovery boiler is dissolved in water and mixed with a slurry of calcium hydroxide, the calcium hydroxide having been formed by the addition of calcium oxide to water. The calcium hydroxide reacts with the sodium carbonate to form sodium hydroxide and calcium carbonate as a precipitate. The calcium carbonate is washed, filtered, and sent to the lime kiln where it undergoes thermal decomposition to regenerate the calcium oxide. This process is demonstrated by the following equations.

Equation 1 $$CaO + H_2O \Rightarrow Ca(OH)_2$$

Equation 2 $$Na_2CO_3 + Ca(OH)_2 \Leftrightarrow 2NaOH + CaCO_3$$

Equation 3 $$CaCO_3 \Rightarrow CaO + CO_2$$

The reaction in Equation 2 is an equilibrium reaction. In practice, the reaction occurs at temperatures between 70-100 °C with conversions of 75-85%.[1] The reaction is slightly endothermic with a heat of reaction close to zero. Changing the temperature does not have a big enough impact on the conversion to drive the reaction to completion. The remaining unconverted sodium carbonate is part of what is known as dead load in the pulping cycle. The sodium carbonate does not participate in the pulping reaction and is detrimental because additional energy is needed to heat it and evaporate the water accompanying it during the processes of pulping, evaporation, and combustion. It would be of benefit from capacity and energy efficiency considerations to have a process that reaches higher efficiencies in the conversion of sodium carbonate to sodium hydroxide.

With the lime based causticizing system, the causticizing reaction takes place in an aqueous environment. This requires that the molten smelt be cooled and that the calcium carbonate subsequently be heated to convert it to calcium oxide. The thermal decomposition of the calcium carbonate to calcium oxide requires approximately 5-7 MMbtu/ton CaO.[2] The lime kiln is therefore one of the biggest energy users in a chemical pulp mill. Elimination of this step could be beneficial. An energy advantage might be obtained with an alternative process.[3]

Alternative ways to convert sodium carbonate to sodium hydroxide have been known for many years. In the pulp and paper industry, the Direct Alkali Regeneration System (DARS) has been commercialized in Tasmania for use with the soda-anthraquinone pulping process.[4,5] In this system, sodium carbonate reacts with iron

oxide at high temperatures in a fluidized bed reactor. The resulting product, sodium ferrite, is subsequently dissolved in water and undergoes a hydrolysis reaction to form sodium hydroxide and iron oxide as demonstrated in the following reaction sequence.

Equation 4 $$Na_2CO_3 + Fe_2O_3 \Rightarrow Na_2O \cdot Fe_2O_3 + CO_2$$

Equation 5 $$Na_2O \cdot Fe_2O_3 + H_2O \Rightarrow 2NaOH + Fe_2O_3$$

This process is known as direct causticizing because the number of reaction steps have been reduced when compared to the lime based system. The simplified process chemistry also results in fewer process operations when compared to the lime based system. Unfortunately, the iron oxide based direct causticizing system does not work with kraft pulping liquors. DARS is used for soda-anthraquinone pulping which does not contain the sodium sulfide found in kraft systems. If sulfides are added to the DARS process, they undergo a negative side reaction with the iron oxide to produce stable iron sulfides.[5]

Other metal oxides have been identified as possible direct causticizing agents for use with kraft recovery systems. Titanium dioxide has been investigated and found to be an acceptable compound that does not react unfavorably with sulfur components.[6,7] It has also been suggested in a Canadian Patent by Budney that manganese oxides could be used for direct causticizing.[8] Because there was no support for this claim in the literature, it became the focus of this work.

It was the intention of this investigation to study the reaction between sodium carbonate and manganese oxides. Little was known about reaction stoichiometry, mechanisms, and kinetics of this system. In addition, for application to a kraft system, the influence of sodium sulfide on the reaction was also to be investigated.

LITERATURE REVIEW

A review of several topics related to the thesis investigation is presented. Previous work in direct causticizing is presented first to highlight some of the issues that are relevant specifically to direct causticizing. Because of the nature of the reaction under study, a discussion of general solid-solid reactions is also included. Additionally, a section is included on previous work specifically related to the reaction between sodium carbonate and manganese oxides.

DIRECT CAUSTICIZING

General Principles

A general representation of the direct causticizing reaction is given below.

Equation 6 $$aNa_2CO_3 + bM_xO_y \Rightarrow Na_{2a}M_{bx}O_{a+by} + aCO_2$$

Equation 7 $$Na_{2a}M_{bx}O_{a+by} + (a+bz)H_2O \Rightarrow 2aNaOH + bM_xO_y \cdot zH_2O$$

In the above equations M_xO_y represents a generic amphoteric metal oxide. The characteristics of the metal oxide lead to different classifications of the causticizing reaction. If the metal oxide is soluble in the pulping liquor that is produced, the system is called autocausticizing. In the case where the metal is insoluble it is termed direct causticizing. Examples of soluble metal oxides include B_2O_3 and P_2O_5.[9]

Autocausticizing

The borate and phosphate systems have previously been studied by Janson.[10] The temperature range was between 725 and 875 °C for borates and 325 and 875 °C for phosphates. He concluded that the decomposition of sodium carbonate followed approximate first order kinetics. However, because of their soluble nature, the use of borate and phosphate based autocausticizing agents would require that the pulping system be based on these components. A new pulping system was beyond the scope of this work so the focus remained on direct causticizing agents.

TiO_2 – Sulfur Free

Metal oxides that are insoluble have been identified as TiO_2, Fe_2O_3, $FeTiO_3$, and MnO_2.[11] Early work in direct causticizing for the pulp industry was done by Kiiskila and Virkola[9], Kiiskila[12,13,14,15,16], and Kiiskila and Valkonen[17]. Their studies focused on the non-sulfur containing soda pulping system in a combustion based recovery process. Their work looked at a variety of different operating conditions and the kinetics of the hydrolysis reaction.

Kiiskila found that the decomposition of Na_2CO_3 by TiO_2 in an air environment starts around 500 °C and is initially a solid-solid reaction[12,13]. The rate of reaction is relatively slow until the melting point of sodium carbonate, ~850 °C, is reached, at which point it is no longer a solid-solid reaction. The sodium titanates that formed had a variety of stoichiometries, depending on the reaction temperature. Ratios of Na_2O:TiO_2 of 1:1, 4:5, and 1:3 were possible. It was found that as the reaction temperature increased, the ratio of TiO_2 to Na_2O in the final product also increased.

Hydrolysis of the reaction products was done at 30, 60, and 90 °C. The rate of hydrolysis was found to be dependent on the stoichiometry of the titanate and the temperature.[12] As the molar ratio of TiO_2 to Na_2O increased, the hydrolysis rate decreased. As temperature increased the rate of hydrolysis increased. However, hydrolysis did not go to completion. The remaining product was Na_2O-$3TiO_2$. The conclusion was that in a real application, the active material for direct causticizing would have to be Na_2O-$3TiO_2$.

Fe_2O_3 – Sulfur Free

The decomposition of Na_2CO_3 by Fe_2O_3 was studied from 700 to 1100 °C with Na_2CO_3:Fe_2O_3 ratios of 0.8, 1.0, and 1.25.[17] Hydrolysis was done at 45, 75, and 95 °C. The direct causticizing temperature was found to have a large effect on the formation of the sodium ferrite. At 700 °C, in the solid state, with an equal molar ratio of Na_2CO_3 and Fe_2O_3, 5% of the carbonate reacted after 30 minutes. At 900 °C, with molten carbonate, >95% of the carbonate reacted. The initial molar ratio of Na_2CO_3 to Fe_2O_3 also has a large effect on the reaction. Increasing the amount of Fe_2O_3 increased the rate of conversion of Na_2CO_3.

The rate of the hydrolysis reaction of the sodium ferrite reaction products increased with increasing temperature, as in the case of the sodium titanates. Complete hydrolysis of the sodium ferrite did not occur however, with a maximum of 84% being hydrolyzed. This indicates that some dead load would be recirculating in a commercial process. The material was still active when recycled and reacted with Na_2CO_3. When

rehydrolyzed, similar causticities were obtained suggesting no continuing loss in activity.[17]

Ilmenite – Sulfur Free

Ilmenite, the double oxide of iron oxide and titanium dioxide, was also investigated by Kiiskila.[14] The performance of the ilmenite was found to have characteristics of the iron oxide and titanium dioxide systems. A comparison amongst the materials showed TiO_2 to give highest reaction rate, followed by ilmenite, then iron oxide.[15]

Commercial Application – Sulfur Free

The application of direct causticizing in chemical recovery was first commercially installed in full scale by the Associated Pulp and Paper Mills in Burnie, Tasmania.[5] The black liquor for the process comes from the soda-AQ pulping of a mixed chip furnish. It is burned in a fluidized bed reactor at 1000 °C. The direct causticization material is mineral grade iron oxide, hematite. The use of iron oxide rather than TiO_2 in the DARS system, according to Covey, was based in part on the following observations:[4] 1) Fe_2O_3 is cheaper than mineral grade TiO_2, 2) there is higher sodium volatilization with TiO_2 than Fe_2O_3, leading to concerns of fouling problems, and 3) the recovered ferric oxide from the hydrolysis step is drier than the TiO_2 because the titanates form a much finer product upon hydrolysis. An increase in thermal efficiency is realized with the drier metal oxide.

$Fe_2O_3 – Na_2SO_4$

A major drawback to the DARS process is its incompatibility with kraft black liquors. In the combustion atmosphere, the sulfur containing components can react with the iron oxide to form iron sulfides. Work by Seymour at IPST on the application of

DARS to the kraft pulping process appears to confirm this.[18] The reaction of sodium carbonate with iron oxide in the presence of sodium sulfate was studied at 1000 °C in air and inert atmospheres. The reaction product was hydrolyzed for 1 hour at 90 °C. The remaining Na_2CO_3 was measured to determine the conversion of the initial sodium carbonate. The recovered solid material from the hydrolysis step was recycled and reacted with fresh Na_2CO_3 and Na_2SO_4. The conversion of Na_2CO_3 decreased with each recycle for three cycles. A blank experiment without Na_2SO_4 appeared to level off after two cycles. The author speculated that the activity of the iron oxide was decreased due to the presence of Na_2SO_4 in the reaction mixture.

Kraft - Thermodynamics

Zou, et al. conducted thermodynamic equilibrium calculations to evaluate Fe_2O_3, Al_2O_3, and TiO_2 as causticizing agents for kraft black liquor.[6] The chemical species present in the calculations included sodium sulfides and sulfates. The simulations were done for inert and reducing atmospheres. They found that iron oxide reacts with sodium sulfide to form FeS. In addition, the iron oxide can also be reduced to Fe or FeO. Al_2O_3 and TiO_2 were not influenced by the presence of sulfur and could be used as direct causticizing agents. However, the Al_2O_3 is somewhat soluble in strong bases, putting it in the category between direct causticizing and autocausticizing. It was listed as unsuitable for direct causticizing because it can not be easily separated from the pulping liquor.

From the calculations two process configurations were suggested.[6] One was the combustion of kraft black liquor in the presence of TiO_2 followed by a reduction step.

The oxidizing atmosphere would form Na_2SO_4, requiring the reduction to Na_2S to produce the correct pulping liquor. The other process was based upon the gasification of kraft black liquor in the presence of TiO_2. In gasification, the black liquor is reacted with sub-stoichiometric amounts of oxygen. This leads to a reducing atmosphere and the production of a product gas rich in CO and H_2. The calculations suggested that in this scenario, the sulfur would stay in the reduced form, either as Na_2S or H_2S. The further reduction step would not be needed.

TiO_2 - Kraft - Combustion

Zou pursued the combustion and direct causticizing of kraft black liquor with TiO_2 as an alternative chemical recovery method.[19,20] He first studied the reaction between Na_2CO_3 and TiO_2. This was followed by the addition of Na_2SO_4. Next he used kraft black liquor as the starting material. The reaction between Na_2CO_3 and TiO_2 first produced $4Na_2O\text{-}5TiO_2$, then $Na_2O\text{-}TiO_2$ in the temperature range 750 to 925 °C. The reaction appeared to be controlled by diffusion of the Na and O species through the product layer. He reported an activation energy of 216 kJ/mol. The reaction was not influenced significantly by the presence of Na_2SO_4.

For the combustion of black liquor with $Na_2O\text{-}3TiO_2$, Zou found that very high process efficiencies could be obtained. For combustion at 890 °C for 60 minutes, followed by hydrolysis at 80 °C for 90 minutes, overall causticizing efficiencies of 95% were reported.[19]

TiO_2 - Kraft - Gasification

Zeng studied direct causticization with TiO_2 in conjunction with kraft black liquor gasification.[7,21,22] His work focused on the pilot scale development of the process at temperatures between 700 and 900 °C. Kraft black liquor solids of 75 μm diameter and TiO_2 of 75 to 250 μm diameter were used. He investigated the effects of temperature, initial concentration of reactants, and amount of air used for gasifying on the direct causticizing reaction. The three parameters did not appear to have a large impact on the overall causticizing efficiency. Values were typically near 97%. However, the air ratio did affect the quality of the outlet gas. High temperatures resulted in higher CO/CO_2 ratios. The lack of sensitivity to changes in parameters for the causticizing efficiency is probably because the unit was operated in a semi-batch mode with relatively long residence times. The time was probably sufficient under all conditions to reach the maximum conversion, within experimental limits.

Sulfur containing species did not appear to react with the TiO_2. With the gasification system, it would be ideal if all of the sulfur were reduced to sulfide. Zeng found that he could achieve a sulfur reduction of 75 to 85%.[7] Reduced sulfur species were primarily divided between gas phase H_2S and solid Na_2S. As the temperature was increased from 700 to 900 °C, the gas phase H_2S concentration decreased from 9000 to less than 2000 ppm.

MnO_2 – Kraft – Combustion

A Canadian Patent describes a direct causticizing process for soda or kraft chemical recovery using MnO_2 as the preferred causticizing agent.[8] MnO_2 was selected

as the direct causticizing agent because it does not readily form manganese sulfide, MnS. No data were presented with the patent.

ABB Combustion Engineering did some small-scale laboratory trials with MnO_2 as a direct causticizing agent.[23] These indicated that direct causticizing would occur. A mill trial, comprised of adding MnO_2 to the recovery boiler prior to a shut down, did not yield positive results.

SOLID-SOLID KINETICS

Sodium carbonate has a melting point close to 850 °C. Manganese oxides are solid up to 1600 °C. Below the melting point of sodium carbonate, the direct causticizing reaction will occur in the solid state.

Heterogeneous solid state reactions are described by two solids, A and B, in contact reacting to form a solid product C, sometimes with evolution of gas D. In order for the reaction to occur, there has to be contact between the two solid surfaces. The rate-determining step in solid-solid reactions can be either the chemical reaction or diffusion. The chemical reaction describes a bond redistribution step occurring at the reaction interface. For the diffusion limitation, the transport of the reactants through the product layer is slower than the chemical reaction. Most solid-solid reactions are diffusion controlled.[24]

The primary difference between the mechanism of diffusion in solids and fluids is that in the solid state, atoms are more constrained in the lattice structure. Diffusion in solids occurs when atoms or molecules jump from one atomic site to another. For a pure compound there are two primary types of diffusion, interstitial and vacancy diffusion. For ionic compounds diffusion requires that electroneutrality be maintained. In ionic species diffusion primarily occurs by Frenkel or Schottky disorder within the solid.[25] In addition, for both pure and ionic compounds, paths of high diffusivity can exist at grain boundaries and dislocations.

Atoms in crystals have spaces between them known as interstices. Interstitial diffusion occurs when small atoms of another species move around in the solid, squeezing between atoms in the interstices as shown in Figure 1. The diffusing species moves by travelling from one interstices to another. C, O, N, and H diffuse interstitially in most crystals.[26]

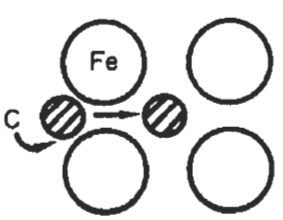

Figure 1 Interstitial diffusion of carbon in iron.

A missing atom in the lattice structure creates a vacancy. Vacancy diffusion occurs when atoms that are too large to fit in interstices travel in these lattice vacancies as

shown in Figure 2. This is the mechanism by which most diffusion in crystals takes place.[26]

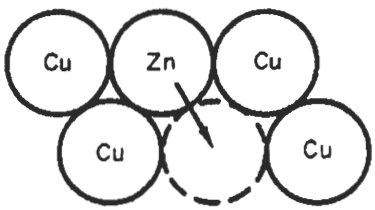

Figure 2 Vacancy diffusion of zinc in copper to form brass.

For an ionic species AB, a Frenkel disorder occurs when a component moves to an interstitial site, leaving a corresponding hole in the lattice. A Schottky disorder occurs when equal number of vacancies of each component occur as shown in Figure 3. In both cases the charge neutrality is maintained.[25] The diffusion of component CD through AB, can occur by either Frenkel or Schottky mechanisms, as long as there is not an accumulation of charge.

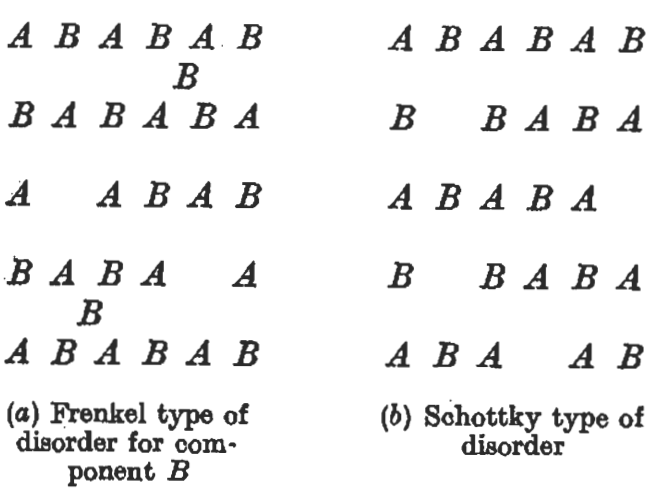

Figure 3 Frenkel (a) and Schottky (b) disorders in ionic compound AB.

The overall rate of diffusion can be increased due to high-diffusivity paths in the material. Grain boundaries and dislocation cores are examples of areas that result in increased rates of diffusion.[27] Diffusion rates along grains or dislocation cores can be 10^6 times greater than in the bulk material.[26] The contribution to the total diffusivity depends on the number of grain boundaries and dislocations in the material. Small grains or numerous dislocations increases their contribution.

When two solids are in contact, the chemical reaction starts at nucleation centers. These nucleation centers are usually defects or weaknesses in the solid surface that result in increased reactivity. The rate of nucleation formation has been described by four models: a) instantaneous nucleation; b) exponential model of nucleation; c) linear model of nucleation; d) the power model of nucleation. Instantaneous nucleation implies that nucleation occurs instantly at all pre-existing nucleation sites. The exponential model describes random, single step nucleation amongst the pre-existing sites. The linear model results in slow, single step formation, while the power model describes multi-step nucleus formation.[28,29]

From the nucleation centers, a product layer grows. The growth of the nuclei interface is generally accepted to have a constant interface advance.[24] The growth of the nuclei occurs until the product layer from adjacent nuclei overlap. The overlapping nuclei lead to an interface connecting the initial reaction centers. The initial part of a solid-solid reaction is therefore limited by nucleation and growth of the nuclei until a uniform product layer is formed as illustrated below.

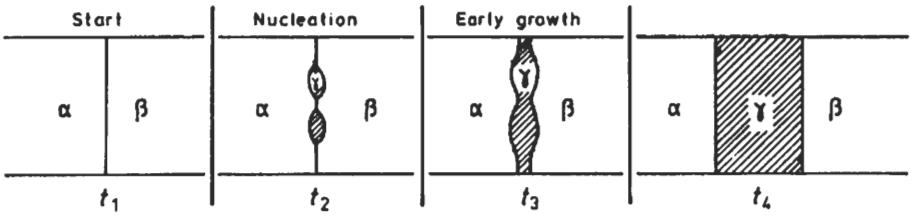

Figure 4 Schematic of nucleation and early growth leading to a uniform product layer.

Nucleation and initial growth kinetics combine a nucleation model with a growth model to describe the process leading to a uniform product layer. The two simplest developments of nucleation and growth models are described by a power model and exponential model. In the first case a multi-step nucleation is assumed, followed by a constant rate of interface advance. This leads to an expression relating the conversion of a reactant to the time of reaction.[24]

Equation 8

$$\alpha^{1/n} = kt$$

α is the conversion and k represents the kinetic rate constant. The power, n, is usually between 2 and 4. Likewise, if random nucleation is assumed with a constant rate of interface advance, the exponential model is developed.[24]

Equation 9

$$\ln\alpha = kt$$

The two expressions above are grouped into a class known as acceleratory rate equations. The rate of conversion keeps increasing with time. These equations assume

that each nucleation site produces product that are independent from each other. There is no accounting for products combining, and thus slowing the rate of conversion. It is unrealistic to imagine that a crystal of finite size is capable of maintaining a continuous increase in reaction rate up to 100% conversion. For this reason, these equations should only be valid at low conversions.

A broader treatment of nucleation and growth was independently developed by Avrami[30] and Erofe'ev[31]. They took into account the impingement and coalescence of developed nuclei and the ingestion of undeveloped nucleation sites. In this treatment, two adjacent nuclei with product growth could coalesce and reduce the overall interface available for reaction. Ingestion refers to the elimination of a nucleation site by the growth of developing nuclei. The resulting equation is called the Avrami-Erofe'ev (A-E) equation.

Equation 10 $$[-\ln(1-\alpha)]^{1/n} = kt$$

Equation 11 $$n = \beta + \lambda$$

The exponent n is comprised of two components with β representing the number of steps involved in nucleus formation, and λ represents the number of dimensions in which the nuclei grow. Typical values for β are 0 or 1, with 0 corresponding to instantaneous nucleation. For λ, 3 represents spheres or hemispheres, 2 is for discs or cylinders, and 1 is for linear development. Typically, it is found that $2 < n < 4$.[24] The A-E equation yields a sigmoidal curve when conversion, α, is plotted versus time. The initial part of the curve

is acceleratory due to the nucleation. As the reaction progresses and the growing nuclei interfere, the rate of conversion decelerates.

The third type of rate equation used to describe solid-solid kinetics is deceleratory. Deceleratory reactions yield an α versus time curve that is steadily rising, yet concave down. Deceleratory rate equations are based on diffusion mechanisms or geometric models.

If a cube of edge a is considered to undergo complete nucleation simultaneously on all faces, then the volume of reactant remaining at time t is a cube of edge (a-2kt). This assumes a constant linear advance of the reaction product with rate k. The following relationship is known as the contracting volume equation.[28,29]

Equation 12

$$1-(1-\alpha)^{1/3} = kt$$

This equation is strictly based on geometry with the assumption that every site on the surface is a nucleation site. Because of this, the rate of conversion can only decrease with time due to a decrease in surface available for reaction. Similarly, for a rectangular body that undergoes reaction in two dimensions, the contracting area relationship applies.

Equation 13

$$1-(1-\alpha)^{1/2} = kt$$

Another attempt to describe solid-solid reactions is adapted from the well-known parabolic law of Wagner[32], which is used to describe tarnish reactions. Wagner

considered a planar metal surface exposed to air with a constant concentration of oxygen, C_o. The oxygen reacts with the metal to form a product layer tarnish of thickness X. With time, oxygen diffuses through the product layer to the reaction interface at the unreacted metal surface. This is shown schematically in Figure 5. The rate of chemical reaction is assumed to be much faster than the rate of diffusion of oxygen through the product layer. The reaction between the oxygen and metal causes the product layer to grow according to the following expression.

Equation 14

$$X = (2DC_oV_Mt)^{1/2}$$

D is the diffusion coefficient of the diffusing species through the product layer. V_M is the molar volume of the product. Many tarnish reactions are in good agreement with this model.[33]

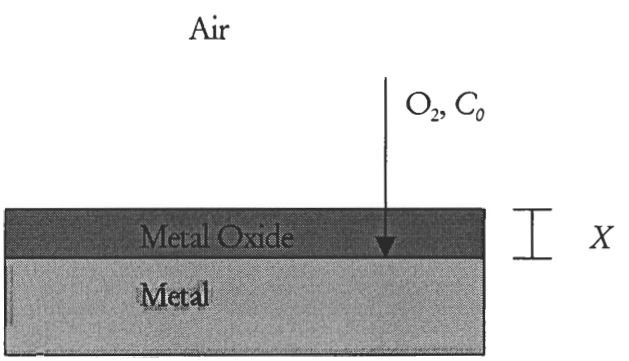

Figure 5 Schematic of tarnish reaction.

A diffusion limited solid-solid reaction can also be described by Equation 14 if certain assumptions are made. Jander is credited for adapting the above equation to the

solid-solid reactions taking place between spherical particles.[34] In this case, two spherical powdered reactants are mixed together. The lower melting point species becomes the diffusing species. At reaction initiation, it is assumed that the diffusing species undergoes surface diffusion to cover the higher melting point particles with a uniform layer. This is a good assumption for the temperatures at which most solid-solid reactions take place.[24] This uniform layer has a concentration equivalent to the molar volume of the diffusing species corresponding to C_0 in Equation 14.

If a sphere of initial radius r, reacts to a depth of radius s, the thickness is:

Equation 15

$$X = (r - s).$$

From geometry the conversion can then be represented as,

Equation 16

$$\alpha = 1 - \left(s^3 / r^3\right).$$

Substituting Equation 15 and Equation 16 into Equation 14 yields

Equation 17

$$\left[1 - (1 - \alpha)^{1/3}\right]^2 = kt$$

and

Equation 18

$$k = 2DC_oV_M / r^2.$$

These equations, developed from Fick's Law of diffusion, describe a diffusion-controlled reaction between spherical particles. One of the drawbacks of the equation development is that it does not take into account the crossing of the diffusion paths in spherical geometry as the reaction proceeds. The parabolic law is for a planar surface so this equation should be valid only at small conversions. The application of Jander's equation is often misunderstood. Geiss[35] recommends that it not be used for $\alpha > 0.15$.

Modifications to the equation, by solving the whole problem in spherical coordinates, were done by Ginstling and Brounshtein.[36] This treatment results in an equation of similar form. Because of the geometry modifications to this model, the range of applicability is theoretically from $0<\alpha<1$. However, in practice, it is over a much more limited range. The limitations occur because time is needed to establish a uniform surface coverage of the diffusing species around the reacting particle. Additionally, at the end of the reaction, the surface coverage can become non-uniform due to reactant consumption, resulting in deviation from the model.

Equation 19 $$1 - \tfrac{2}{3}\alpha - (1-\alpha)^{2/3} = kt$$

The Jander and Ginstling-Brounshtein (G-B) equations both assume that surface diffusion rapidly covers the reactant particles with a continuous layer of the diffusing reactant during the initial stage of the reaction. They also assume that the rate of reaction at the higher melting point reactant-product layer interface is much higher than the rate of diffusion of the lower melting point reactant through the product layer. A schematic of the reaction sequence is shown in Figure 6.

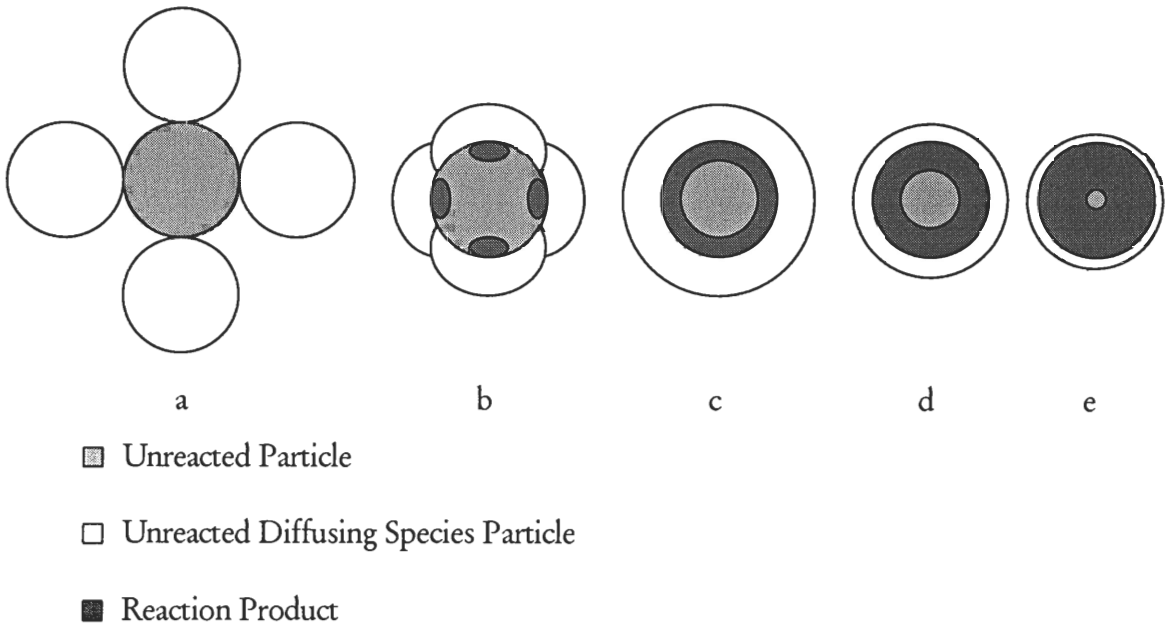

Figure 6 Schematic of the product layer diffusion controlled model for reactions between spherical solid particles. a) Particles prior to reaction. b) Nucleation and reaction initiation at initial contacts. Surface diffusion of coating species. c) Established uniform layer of diffusing species and product layer. The model assumptions are satisfied at this point. d) Continued diffusion of reactant through product layer. Consumption of reactants. e) Reaction near completion.

PREVIOUS SODIUM CARBONATE – MANGANESE OXIDE WORK

Gasik, et al.[37] applied differential thermal analysis (DTA) and thermogravimetric (TG) methods to the study of the reaction between manganese oxides and sodium carbonate in an air atmosphere. They concluded that MnO_2, when reacted with Na_2CO_3, also undergoes a change in oxidation state to become Mn_2O_3 in the temperature range 525-700°C. They were not able to explain thermal effects occurring at temperatures from 765-840 °C. When Mn_2O_3 was the starting material, it reacted directly with Na_2CO_3 from 450-730 °C. Weight losses in the temperature range 730-900 °C were attributed to the reaction of Na_2CO_3 with the initial reaction product. The reaction of Mn_3O_4 with Na_2CO_3 lost weight in the temperature range 400-760 °C. This was attributed to a

reaction between Mn_2O_3 and the carbonate. It is not clear if the Mn_2O_3 is assumed to be part of the Mn_3O_4, which is a mixed oxidation state component. They did not determine quantitative values to describe the reaction kinetics. They did conduct isothermal experiments at 820 °C with several different particle size mixtures. They qualitatively found that pulverized powders reacted quicker than particles or particles mixed with powder.

Another study of sodium carbonate and oxides of transition metals was investigated using TG techniques.[38] For MnO_2 the authors found three maximums in the rate of reaction during heating from 500 to 1400 °C. The first maximum between 500 and 700 ° was attributed to the reaction of MnO_2 with Na_2CO_3. The second maximum between 800 and 950 °C was attributed to the decomposition of Na_2CO_3. The third stage of the reaction was described as "corresponding to the formation of polynuclear complexes of manganese with elimination of oxygen."[38] Activation energies and pre-exponential factors were determined for the three stages of reaction. Activation energies estimated from the maximum rate were reported as 262, 162, and 125 kJ/mol for the three stages respectively. An alternate method of analysis based on the time to reach the maximum rate gave values of 191, 160, and 130 kJ/mol. Pre-exponential factors were calculated as $4.8E^{13}$, $1.7E^{4}$, and $9.4E^{2}$ min^{-1}. The alternate method of analysis yielded $3.3E^{11}$, $1.7E^{7}$, and $6.5E^{4}$ min^{-1} for the three stages.

The two studies above suggested that MnO_2 would be reduced to Mn_2O_3 in the presence of Na_2CO_3. Giovanoli investigated the thermal reduction of MnO_2 alone in

oxygen.[39] Several samples of MnO_2 were heated at an unknown rate in a TG furnace microbalance apparatus. The samples exhibited weight loss from 500 to 700 °C corresponding to the following equation.

Equation 20 $$4MnO_2 \Leftrightarrow 2Mn_2O_3 + O_2$$

With further heating, another transition took place from 900 to 950 °C corresponding to the further reduction shown below.

Equation 21 $$6Mn_2O_3 \Leftrightarrow 4Mn_3O_4 + O_2$$

These reductions occurred in the presence of oxygen. If done in nitrogen, it is quite probable that the transformations could take place at lower temperatures.

PROBLEM ANALYSIS

Direct causticizing is a technology that has potential to simplify the kraft chemical recovery process. Direct causticizing has already been applied to soda-anthraquinone based chemical recovery in the form of DARS, the Fe_2O_3 based direct causticizing agent. The problem with DARS is that the Fe_2O_3 reacts unfavorably with sulfur components, therefore making it unacceptable for use with kraft chemical recovery.

TiO_2 has also been studied as a direct causticizing agent. It has been investigated for soda liquor under combustion conditions, and kraft black liquors under combustion and gasification conditions. The mechanism of reaction and kinetics for the TiO_2 system have been well described in the literature. TiO_2 has solid potential for use as a direct causticizing agent with soda and kraft liquors, particularly when combined with gasification. A drawback to TiO_2 based direct causticizing is the reaction stoichiometry. Upon hydrolysis of the reaction product, one sodium oxide remains associated with three TiO_2 molecules. This 1:3 complex is the actual direct causticizing agent. The reaction of Na_2CO_3 with the 1:3 complex yields a 4:5 complex that then undergoes hydrolysis. Even though high causticizing efficiencies are obtained, there is a deadload of Na_2O and TiO_2 that is not fully utilized. The ideal situation would be a metal oxide that undergoes complete hydrolysis and is able to complex with one or more Na_2O species.

Manganese oxide, as MnO_2, has been suggested as a potential direct causticizing agent that would not react unfavorably with sulfur components. A Canadian patent describes a process for direct causticizing with MnO_2, yet there is no supporting work

confirming its potential. The previous work that was presented for the reaction between manganese oxide and sodium carbonate suggested that the MnO_2 would, in addition to reacting with the Na_2CO_3, simultaneously undergo a change in the oxidation state upon heating in air. The mechanism and stoichiometry of the reaction was not clearly determined. In addition, the kinetic analysis did not include information on reactant particle size and initial concentration effects. With so many unanswered questions, an investigation of manganese oxides as direct causticizing agents could be a significant contribution to the literature on direct causticizing.

PROBLEM VERIFICATION

In order to validate that MnO_2 was a potential direct causticizing reagent, some initial qualitative experiments were completed. Sodium carbonate as a 90μm fine powder was dried at 300 °C. TiO_2 of <1μm was combined in a 1.25:1 molar ratio with the Na_2CO_3. MnO_2 of <325μm was mixed with the Na_2CO_3 in a 1:1 molar ratio. Approximately 1 gram of the mixtures were placed in open top ceramic crucibles. Two temperatures were used in the experiments, 700 and 800 °C. The crucibles were placed in a pre-heated, nitrogen purged muffle furnace. The crucibles were removed at 30-minute intervals, up to 3 hours. The weight loss was recorded and a Na_2CO_3 conversion was calculated based on the assumption that all weight loss was due to CO_2 evolution. At the time, it seemed like a good assumption for the MnO_2 system, but now it is known that a fraction of the weight loss is due to the reduction of MnO_2. The assumed reactions were

Equation 22 $$5TiO_2 + 4Na_2CO_3 \Rightarrow 4Na_2O \cdot 5TiO_2 + 4CO_2$$

and

Equation 23 $$MnO_2 + Na_2CO_3 \Rightarrow Na_2O \cdot MnO_2 + CO_2.$$

The resulting conversions are presented in Figure 7. The conversions for the TiO_2 system are correct, while the MnO_2 conversions have the wrong magnitude.

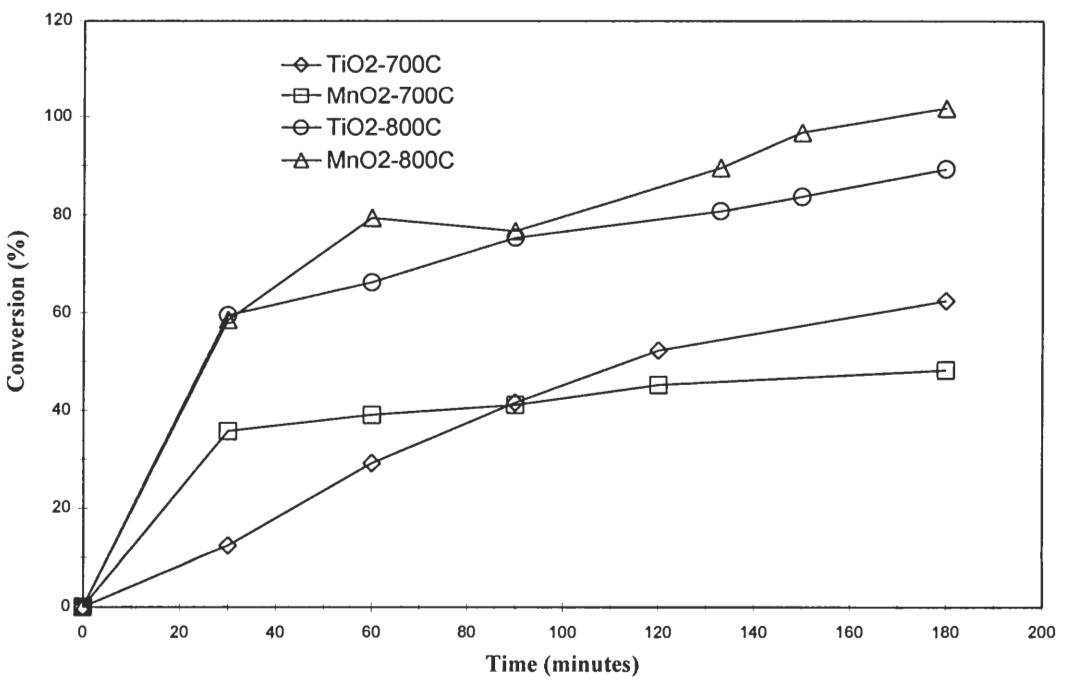

Figure 7 Conversion of Na_2CO_3 versus time of reaction. MnO_2:Na_2CO_3 1:1 and TiO_2:Na_2CO_3 1.25:1

In order to confirm that the direct causticizing did take place, a portion of the reaction product was dissolved in water and heated for 90 minutes at 90 °C to complete the hydrolysis step. The liquor was qualitatively analyzed and found to contain NaOH.

A second set of experiments was conducted to see if Na_2S could be present in the reaction mixture without interfering with the direct causticizing reaction. This was done at 800 °C for 60 and 120 minutes with the MnO_2. A 1:1 molar mixture of MnO_2:Na_2CO_3 was prepared. Na_2S, as $Na_2S \cdot 9H_2O$, was added to the mixture in a 0.33:1 Na_2S:Na_2CO_3 ratio. After reaction, the mixtures underwent hydrolysis and analysis by the ABC titration. The titration results indicated that NaOH and Na_2S were present in the liquor. The amounts were not determined quantitatively because the hydrolysis water was not pre-treated to remove CO_2 and the liquors were not blanketed with nitrogen and immediately analyzed.

The next initial question to answer was whether MnO_2 was the species of interest, or manganese in another oxidation state. MnO_2 was heated in a thermogravimetric apparatus at 10 °C/min. The sample was immersed in a nitrogen atmosphere. The MnO_2 underwent a weight loss corresponding to the transition to Mn_2O_3 in the range 400 to 600 °C. Further weight loss corresponding to the reduction of Mn_2O_3 to Mn_3O_4 took place between 650 and 700 °C. Mn_3O_4 appeared stable up to 820 °C, the operational limit of the equipment. These results confirm that the absence of oxygen reduces the temperature at which manganese changes oxidation state.

From the literature and above experiments, it was determined that MnO_2 would not be the primary manganese oxide involved in the direct causticizing reaction. It undergoes thermal reduction in nitrogen and air above 400 and 500°C, respectively. Although it might react initially with the Na_2CO_3, it will simultaneously be reduced.

Mn_2O_3 should be stable as a reactant in oxidizing atmospheres up to 900 °C. However, in the presence of nitrogen, it was reduced to Mn_3O_4 below 700 °C. Mn_2O_3 could also react with Na_2CO_3, with simultaneous reduction to Mn_3O_4 taking place. Mn_3O_4 was found to be a stable compound at room temperatures up to at least 820 °C in an inert atmosphere. For this reason it was decided that Mn_3O_4 would be the compound of interest in the direct causticizing reaction.

If a process were to be developed using Mn_3O_4 as a direct causticizing agent, there are several things that would be useful to know. The reaction stoichiometry for both the direct causticizing reaction and the hydrolysis step should be understood. The kinetics of the direct causticizing reaction should also be determined. The rate of reaction is usually dependent on the temperature, particle size, and initial concentration of reactants.

The primary objective of this thesis was to obtain kinetic data for the direct causticizing reaction between sodium carbonate and Mn_3O_4. Isothermal experiments were done in the temperature range from 650 to 950 °C. Three particle sizes of the Mn_3O_4 were used to confirm that a decrease in particle size results in a faster reaction. The initial molar ratios of reactants were varied to see if it has an effect on the reaction rate. The conversions of reactants were measured by weight loss and CO_2 evolution. A kinetic model was established that is consistent with the data.

The goal of chemical recovery is to efficiently convert Na_2CO_3 to NaOH. Therefore, a secondary objective was to determine an overall process efficiency for direct causticizing. The reaction product was hydrolyzed to determine NaOH production and subsequently the overall conversion of Na_2CO_3.

In order to be applicable to the kraft process, the manganese oxide should not react unfavorably with sulfur species. Another secondary objective was to determine what effect Na_2S has on the direct causticizing reaction.

The choice of experimental conditions is based on the potential commercial application of the process. Most of the current work on alternative chemical recovery processes is aimed at black liquor gasification. The choices for experimental conditions were therefore primarily selected to be compatible with the gasification process. The temperatures for gasification are typically lower than combustion temperatures. A range from 650 to 950 °C was selected, with the primary focus to be on the solid-solid reaction that would occur in a low temperature fluidized-bed gasification process. Commercially, there are tradeoffs on the particle size. Small particles are desired for quicker reactions, while larger particles would benefit the solids separation during the hydrolysis step. Target sizes of 10, 100, and 225 μm were selected to give a good overall representation. The initial molar ratio of the reactants was selected after some preliminary experiments were done to determine the stoichiometry of the reaction. Choices of 1, 2, and 3 times the stoichiometric requirement of Mn_3O_4 were selected, to ensure complete reaction of the Na_2CO_3.

SPECIFIC OBJECTIVES

Primary: Obtain kinetic data for the direct causticizing reaction between Na_2CO_3 and Mn_3O_4. Establish a kinetic model to explain the data.

Experimental Conditions

Temperature: 650 - 950 °C

Particle size: <38 μm, 90-125 μm, 212-250μm

Mn_3O_4:Na_2CO_3 initial molar ratio: 1.0, 2.0, 3.0

Monitor conversion by measuring CO_2 evolution with IR detector and weight loss.

Secondary: Hydrolyze reaction product to determine NaOH formation and process efficiencies.

Secondary: Determine effect of Na_2S on the reaction between Na_2CO_3 and Mn_3O_4 and compare to sulfur-free system. Modify model as necessary. Continue to monitor conversion with CO_2 evolution.

EXPERIMENTAL APPROACH

OVERALL

In order to study the kinetics of the direct causticizing reaction, an apparatus was developed that would allow the rapid heating of the reactants to a steady temperature, thus allowing essentially isothermal reactions. The reactants were to be swept with a carrier gas that would remove the CO_2, allowing continuous analysis of the reaction progress. A horizontal muffle furnace with cylindrical bore was used to heat the reactants. The furnace had an alumina retort that housed a stainless steel tube. The stainless steel tube was used as the reaction chamber. A 2.6 cm^3 alumina boat was connected to a plunger system that allowed rapid insertion of the reactants into the core of the furnace. The stainless steel tube was purged with nitrogen that was directed to infrared CO_2 detectors. The data acquisition integrated the CO_2 and flow rate signals to yield the total CO_2 evolved versus time. This was converted to Na_2CO_3 conversion, α, versus time for kinetic analysis. After completion of the reaction, the weight loss was determined and a fraction of the material was analyzed with x-ray diffraction (XRD) and scanning electron microscopy (SEM) for product identification and characterization. Additional reaction product was hydrolyzed and filtered. The solid hydrolysis product was also analyzed with XRD and SEM. The aqueous component was titrated to determine NaOH, Na_2CO_3, and Na_2S concentrations.

MATERIALS

Sodium carbonate from Mallinckrodt (Analytical Reagent 99.9%) was used. This material was classified as a fine powder. Before use, it was dried in a nitrogen purged

oven at 290 °C to remove any bound water. The dried material was stored in a dessicator when not in use.

Baker MnO_2 (Reagent Grade 99.99% < 325μm) was also dried at 290 °C and stored in a dessicator prior to use.

Alfa Aesar Mn_3O_4, Manganese (II,III) Oxide, 97+ %, as a 2μm fine powder was also dried at 290 °C and stored in a dessicator prior to use.

Additional Mn_3O_4 was prepared by the thermal reduction of MnO_2. The MnO_2 was placed in an open-top alumina crucible and heated in air at 1075 °C for 2 hours. The resulting material was analyzed by XRD to confirm the conversion to Mn_3O_4. The powdered Mn_3O_4 was mechanically fractionated with 8" diameter stainless steel sieves. Two fractions were retained: 212-250μm and 90-125μm. A third fraction was obtained by grinding Mn_3O_4 of <90μm diameter with a mortar and pestle. The material was sieved and the <38μm fraction was saved for experimental use.

Sodium sulfide as $Na_2S \cdot 9H_2O$ was supplied by EM Science as fused flakes. The flakes were ground into a fine powder with a mortar and pestle and stored in a dessicator.

Activated carbon from Norit Chemicals, Norit SX4, was acid washed and steam activated by the manufacturer. It was a fine powder and used as received.

The sodium carbonate and Mn_3O_4 were sent to Micromeritics in Norcross, GA for particle size distribution analysis. The Elzone apparatus was used to determine volume and number distributions for the particles. With this equipment, an electric field is established in an electrolyte solution in which the particles are dispersed. The electric field is directed through a small orifice. The suspension is drawn through the orifice and the disruption in the electric field when a particle is present is measured. The length of the pulse from the disruption is used to calculate the equivalent spherical diameter. The particle size range for the instrument is 0.4 to 1200μm.

The nitrogen used as the purge gas was supplied by Holox. It was Ultra High Purity grade with a purity of 99.999%. Air Products supplied calibrated standards of CO_2 in nitrogen at 1799ppm and 9.98% for the IR analyzer calibration.

REACTOR

Furnace

The furnace for the reactor was a Lindberg 115V 1400-watt unit. It is a horizontal furnace of clamshell design. The furnace was 30.5 cm in length and had a 5.1 cm bore. The furnace temperature was controlled by an Applied Test Systems (ATS) PID controller. The ATS controller is a single setpoint controller, without any ramping functions.

An open ended 45.0 cm long alumina retort with 4.8 cm outside diameter and 0.3 cm wall thickness was used to shield the reactor from direct contact with the furnace heating elements. The retort was positioned with 10.0 cm exposed from the furnace on the end that the purge gas entered. This is called the cold end of the reactor. Two stainless steel endcaps with 2.0 cm holes were attached to the alumina retort to act as supports for the reactor and to insulate the retort from outside air. A schematic is shown in Figure 8.

Reactor Vessel

A 75.0 cm long by 1.9 cm diameter 316 stainless steel tube was used as the reactor vessel. It was placed in the retort, supported by the endcaps. 20.0 cm of the tube was exposed past the endcap on the cold end. Swagelok fittings were connected to both ends of the reactor. The fittings resulted in a t-type connection with a 0.3175 cm straight through tube connector parallel to the reactor used for the plunger and thermocouple wells. A 0.635 cm tube connector formed the other branch of the t and was connected to the purge gas inlet and outlet.

Temperature Control

0.3175 cm diameter stainless steel tubing was sealed with silver solder at one end and used as the thermocouple well. Another one was made to function as a combined thermocouple well and sample boat plunger. The modification included a 0.25 cm diameter stainless steel wire silver soldered into the end of the tubing. This semi-flexible wire was attached to the sample boat.

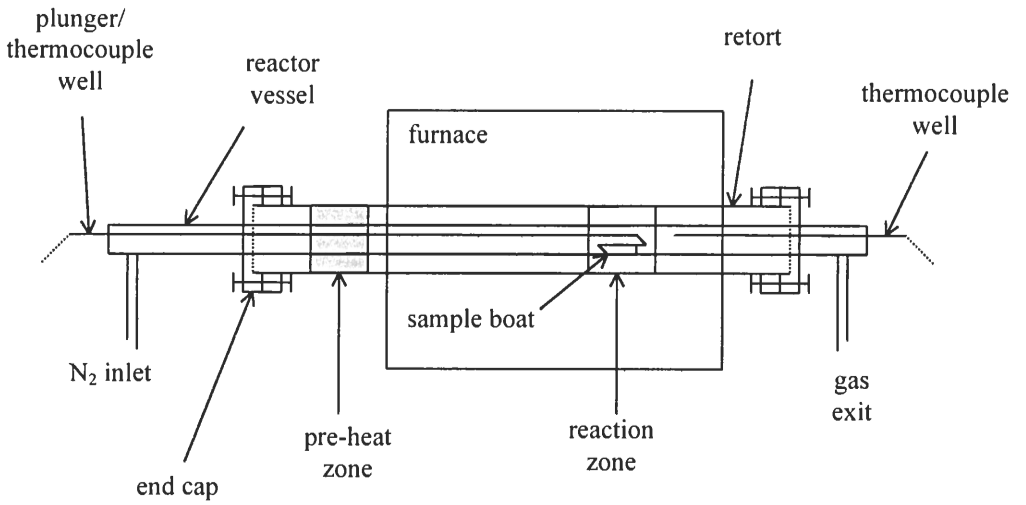

Figure 8 Schematic of reactor used for isothermal experiments.

0.16 cm diameter grounded type K nickel-chromium vs. nickel aluminum thermocouples from Omega were inserted into each of the thermocouple wells. One thermocouple well was inserted through the connector at the end of the reactor where the purge gas exited. This thermocouple well was a fixed position unit that controlled the reactor temperature prior to the start of the reaction. The other combined thermocouple/sample boat plunger was used to insert the reactants into the furnace quickly at the start of the reaction. The thermocouple was positioned to be directly over the reactants. Both thermocouples were connected to a switch with the output going to the furnace temperature controller. The switch was used to allow temperature control to be switched from the reactor to the sample at the initiation of the reaction.

Sample Boat

Alumina was chosen as the best material to use with the reaction system. Al_2O_3 reacts with Na_2CO_3 to form $NaAlO_2$, a dense protective layer.[40] This layer becomes an

effective barrier against further reaction between Na_2CO_3 and the Al_2O_3. An alumina sample boat was purchased from Alfa Aesar. It is an Al-23 combustion boat 4.8 cm long by 0.9 cm wide and 0.6 cm deep. It weighed approximately 9.2 g. The composition is 99.7% alumina and it has zero porosity. It was pre-treated prior to use by filling it with Na_2CO_3 and heating at 900 °C for 30 minutes. During regular use, the boat did not lose or gain weight. The boat was sometimes cleaned in water. Following this, the pre-treatment was repeated. The total weight of the reactants used in the experiments was in the range of 0.2500 to 1.2500 g.

Gas Flow

The carrier and calibration gasses were connected with a header. The outlet of the header passed through a 0-1 SLPM Teledyne Hastings mass flow meter and into the reactor inlet. The gas exiting the reactor passed through another 0-1 SLPM Teledyne Hastings mass flow meter and into the IR-CO_2 detectors. The gas exited the detectors and was purged to the hood. All tubing was 0.635 cm 316 stainless steel.

CO_2 Analysis

Two Infrared Industries model IR702 dual channel nondispersive infrared gas analyzers were coupled in series. The first unit measured CO_2 from 0-30% in the high range and 0-10% on the low range setting. The second unit had detection ranges of 0-6000 and 0-2000 ppm CO_2.

Diatomic and noble gasses do not absorb radiation in the infrared region of the electromagnetic spectrum while other gasses do. Nitrogen does not adsorb infrared while CO_2 does. In the CO_2 analyzer, spectral filters are used to limit the detection to CO_2. An

infrared source operating at about 815 °C emits radiant energy that is directed toward a concave mirror. The reflected energy is collimated into two parallel beams. One beam passes through a reference chamber while the other passes through a sample chamber that contains the flowing gas to be analyzed. The CO_2 attenuates the radiant energy in the sample chamber. Both beams are focused onto a photon detector and the difference in the signals is used to determine the CO_2 concentration. A schematic of the process is shown in Figure 9.

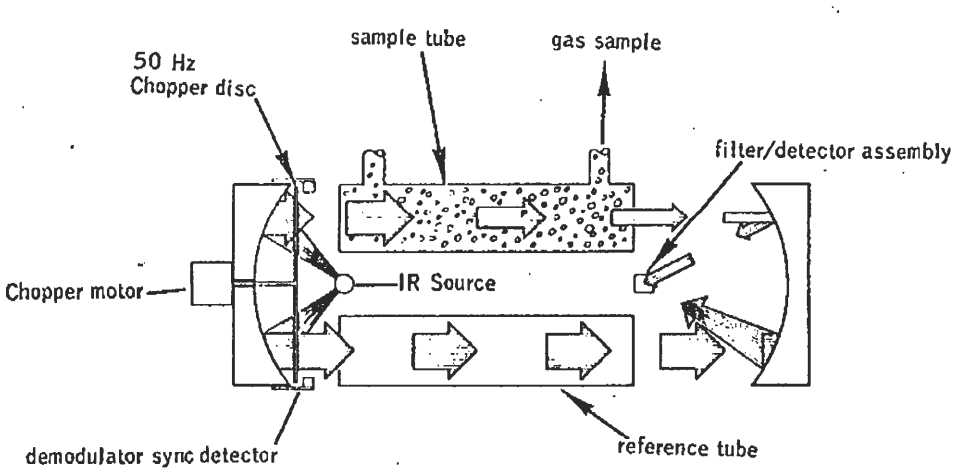

Figure 9 IR Gas Analyzer Schematic.

The low range IR CO_2 analyzer reference tube was purged with nitrogen to improve sensitivity. The detectors output a continuous signal for CO_2 concentration to an analog meter and 0-100 mV output for the data acquisition.

The time lag for the carrier gas to travel from the furnace to the CO_2 analyzer was determined from step change experiments with the CO_2 calibration gas. The time lag was found to be approximately 15 seconds with a carrier gas flow rate of 1 SLPM. This was

insignificant for the solid-solid reactions. For the molten reactions, the CO_2 readings were corrected during the data analysis.

Data Acquisition

A Strawberry Tree Flash 12 Work Mate data acquisition card with eight analog inputs was installed in a Dell 286-12 MHz computer. Work Bench PC Version 2.04 was used to coordinate the data acquisition. Temperatures, flow rates, and CO_2 concentrations were collected as raw data. The sampling rate varied depending on the reaction conditions. The solid-solid reaction was typically sampled every 5 seconds for the first 20 minutes of reaction. It was then switched to sample every 1 to 5 minutes for the remaining reaction. The solid-liquid reactions were typically sampled every second for the duration of the experiment.

The software was developed to correct the flow meter reading exiting the reactor based on the CO_2 concentration in the gas. This corrected flow was then multiplied by the CO_2 concentration and integrated to yield the total moles of CO_2 evolved versus time. All data was then logged to disk. A schematic of the overall experimental set-up is shown in Figure 10.

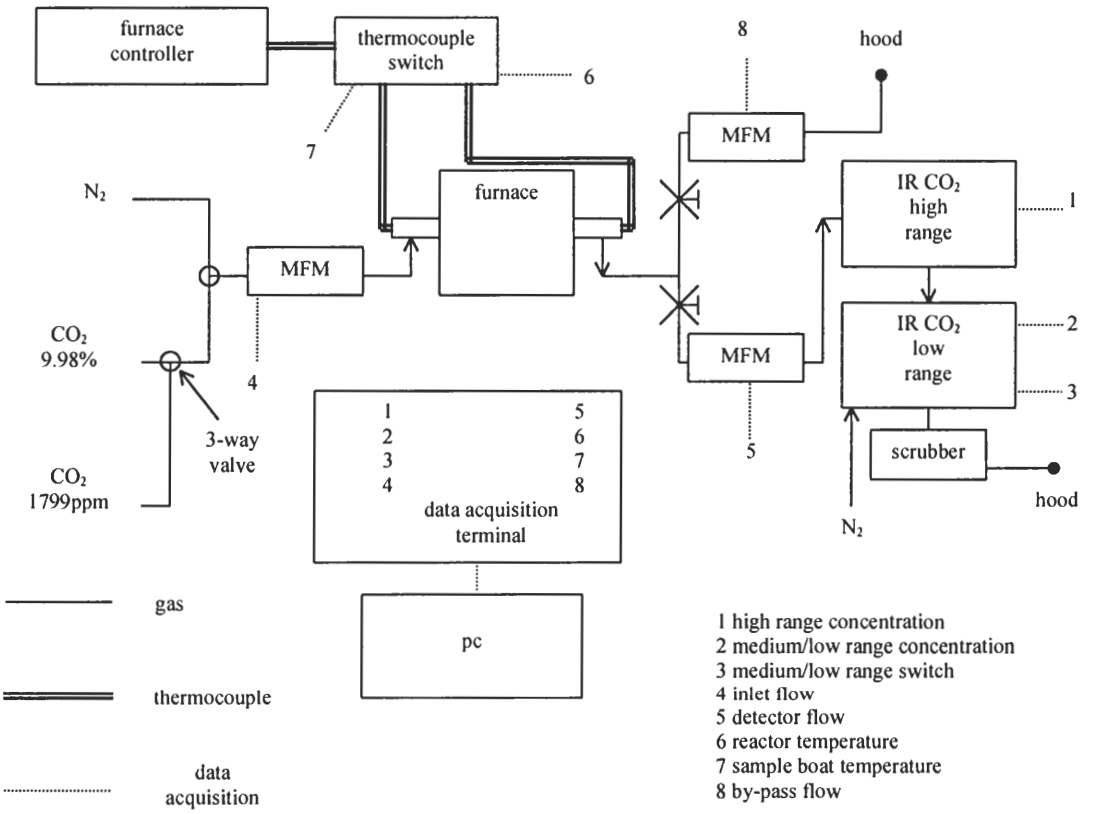

Figure 10 Schematic of experimental apparatus.

ANALYTICAL METHODS

Hydrolysis

A fraction of the reaction product, ~0.25 g, was placed in a 250ml Erlenmeyer flask with a Teflon stir bar. 100 ml of distilled, deionized and boiled water was then added. The mixture was heated to 90 °C for 5 hours under a nitrogen purge while gently stirring. The mixture was then vacuum filtered onto a 4.7cm PTFE membrane filter from Gelman Sciences with 0.2μm openings. Additional aliquots of treated water were used for rinsing and dilution to 250 ml. The filter cake was dried overnight at 105 °C in air.

Sulfur containing filter cakes were dried overnight in a helium-purged oven at 105 °C. The aqueous solution was blanketed with nitrogen and stored in propylene bottles.

Filtrate Analysis

The aqueous filtrate was analyzed for NaOH, Na_2CO_3, and Na_2S with a Mettler DL70ES Auto Titrator. Standard Method 2320 for the determination of alkalinity was used for the sulfur free analysis.[41] Alkalinity is the total acid neutralizing capacity on account of the titratable bases, carbonate and hydroxide. The sample is titrated to a first equivalent point near pH 8.3 to determine the phenolphthalein alkalinity. The total alkalinity is then determined by continued titration to pH 4.5. Calculations yield the total OH^- and CO_3^{-2} concentrations with a standard deviation of 5 mg/L. For the sulfur containing filtrates, the "ABC method" from the Scandinavian Pulp, Paper and Board Testing Committee, SCAN-N 30:85 was used.

X-Ray Diffraction

Solid powder samples were scanned with a Model 3720 Phillips Automated Powder X-Ray Diffractometer. The x-ray generator was a Model 3100 XRG. The x-rays were from a Cu(α) 1.54184 Å Long Fine Focus source. The diffraction patterns were collected with PC-APD Diffraction Software, Version 3.6. Peak searches were conducted with this software. PC-Identify, Version 1.0E was used in conjunction with the International Center for Diffraction Data (ICDD) Powder Diffraction File 1996 PDF-2 Database for component identification. The x-ray generator was typically operated

with a tension of 30kV and 20mA current. It was raised to 40kV and 30mA for some samples requiring higher detection.

Scanning Electron Microscopy

A JEOL JSM-6400 Scanning Microscope was used at 15kV to acquire the SEM images. The samples were first sputter coated with gold-palladium using a Hummer V sputter coater.

MATHEMATICAL ANALYSIS OF THE DATA

The experimental data had to be analyzed in a quantitative manner to determine if it could be described by one of the kinetic models. The primary raw data from the data acquisition computer was in the form of total moles of CO_2 evolved versus elapsed time in seconds. Additionally, the reactor temperature and CO_2 concentration were also obtained. It was assumed that the evolution of CO_2 corresponded directly to the conversion of Na_2CO_3 following the stoichiometry below.

Equation 24

$$Na_2CO_3 \Rightarrow Na_2O + CO_2$$

Knowing the initial number of moles of Na_2CO_3 used in the reaction, the Na_2CO_3 conversion could be calculated versus time by

Equation 25

$$\alpha_{Na_2CO_3} = CO_{2t} / Na_2CO_{3i}$$

where CO_{2t} is the total moles of CO_2 evolved at time t and Na_2CO_{3i} is the initial number of moles of Na_2CO_3.

The conversion from the CO_2 evolution, which was continuous, was checked against the gravimetric conversion determined at the end of the reaction. The gravimetric conversion was considered more accurate, never exceeding 100%. The cumulative CO_2 conversion was found to be above or below the gravimetric conversion within ±8% on some instances, due to measurement errors with the instrument. CO_2 evolution based

conversions were normalized against the gravimetric conversion by making a linear correction for all times regardless of the CO_2 concentration reading. This resulted in Na_2CO_3 conversion versus time curves for each experiment.

The kinetic models described in the literature review all have rate equations of the same form,

Equation 26 $$f(\alpha) = kt,$$

with the kinetic rate constant, k, having units of s^{-1}. To determine which model best agrees with the data, plots of $f(\alpha)$ versus time were constructed. The plot should be linear with a slope of k. It was found that the kinetic models generally were not linear over the entire range of conversion. A method was developed to determine a range of conversions over which the G-B model would be valid.

After examining the plot of $f(\alpha)$ versus time for linearity, the derivative of the function, $f(\alpha)'$, was calculated and plotted versus time. In theory, the derivative should be constant for $f(\alpha)'$ versus time in the linear region. However, because of the generally sigmoidal shape of $f(\alpha)$ versus time plots for the Ginstling-Brounshtein model, the linear region contained an inflection point. The maximum of the derivative, $f(\alpha)'_{max}$, corresponded to the inflection point in the linear region. The maximum of the derivative in the linear region was determined and used as the central point of the linear region. The end limits of the linear region were then determined on both sides of $f(\alpha)'_{max}$ with values of 80% of $f(\alpha)'_{max}$. Using the value of 80% resulted in linear sections that had $r^2 \geq 0.99$

for the least squares linear fit. The corresponding upper and lower times corresponded to the upper and lower ranges of conversion. The kinetic model, f(α), was then replotted versus time over the conversion range of interest. The kinetic rate constant was then determined directly from the slope.

RESULTS AND DISCUSSION

REACTANT CHARACTERIZATION

XRD Of Mn_3O_4

Varying particle sizes of Mn_3O_4 were needed to study the effect of particle size on the kinetics of the direct causticizing reaction. There were four samples of Mn_3O_4 used in this study. The finest size fraction was the as received material supplied by Alfa Aesar. It will be referred to as powdered Mn_3O_4. The other three samples were obtained by sieving and will be called the small, medium, and large samples. The small, medium, and large Mn_3O_4 were produced by the reduction of MnO_2 as described in a previous section. The reduction step was confirmed by XRD analysis of the Mn_3O_4. Figure 11 shows the XRD pattern obtained for the small Mn_3O_4 sample. Reference pattern data is contained in Appendix VI. The first bar below the spectrum represents the peak positions obtained with the filtering software. Below that are graphical representations of peak positions for matching materials selected by the identifying software. A good match with the Mn_3O_4 reference was obtained. The peak at 2θ of 44.8° is attributed to the low background sample holder. The small peak at 38.4° is attributed to trace amounts of unreacted Mn_2O_3. MnO_2 was not identified in the product. A similar pattern is shown in Figure 12 for the large Mn_3O_4. The medium sample was also similarly determined to be essentially pure Mn_3O_4.

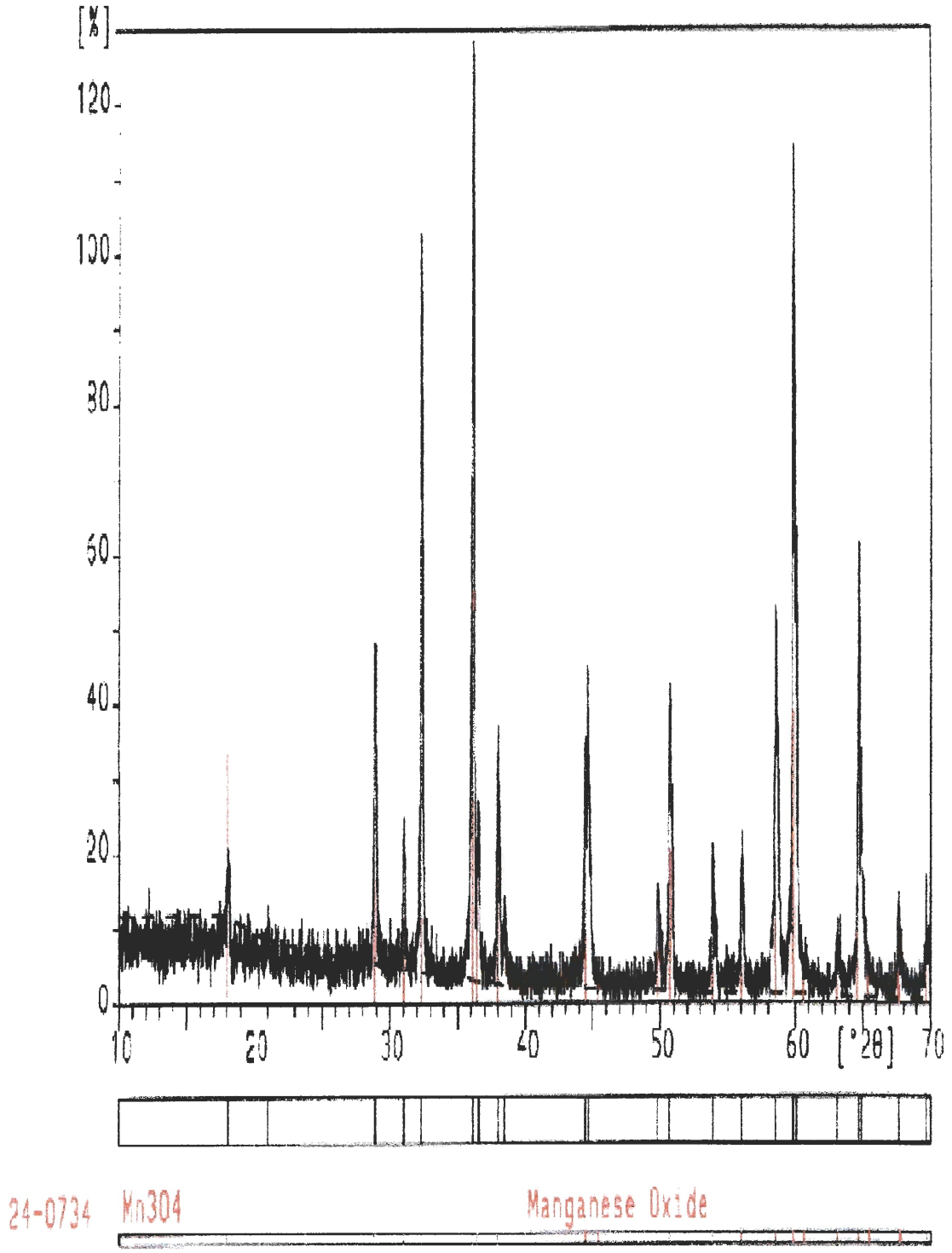

Figure 11 XRD pattern for Mn_3O_4 produced by the reduction of MnO_2. <38µm diameter particles.

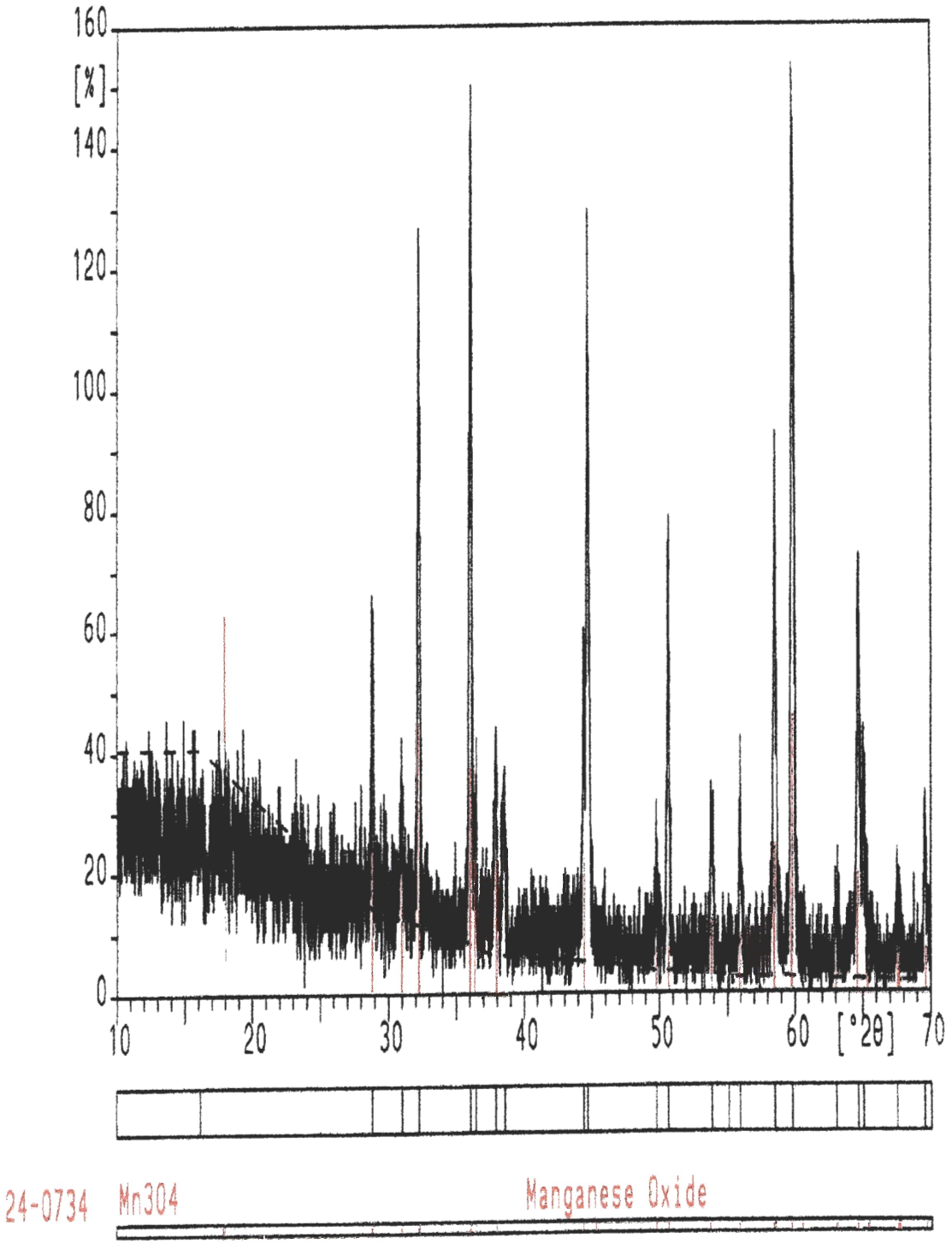

Figure 12 XRD pattern for Mn_3O_4 produced by the reduction of MnO_2. 212-250μm diameter particles.

Particle Size Analysis

The Mn_3O_4 and Na_2CO_3 were analyzed by an outside lab to determine the particle size distributions and mean particle sizes based on the equivalent spherical diameter. The mean particle size was used to determine the effect of particle size on the rate of the reaction. The results are summarized in Table 1. The volume mean gives the dimension of a particle having a volume that is the average of all volumes of all the particles in the sample. The number mean measurement is the dimension of the particle that gives an average diameter for the entire sample. The Sauter mean is also known as the volume surface mean. It is the dimension of the particle which has the average volume per unit surface among the particles sampled.[42]

Table 1 Volume, number, and Sauter mean particle sizes of reactants. *Indicates a partially estimated value.

Species	*Treatment*	*Name*	*Volume Mean Diameter, (μm)*	*Number Mean Diameter, (μm)*	*Sauter Mean Diameter, (μm)*
Mn_3O_4	Sieved 212-250um	Large Mn_3O_4	227	206	225
Mn_3O_4	Sieved 90-125um	Medium Mn_3O_4	104	56	102
Mn_3O_4	Sieved <38um	Small Mn_3O_4	23	3	16
Mn_3O_4	As received	Powdered Mn_3O_4	2*	0.2*	1.2*
Na_2CO_3	As received	Powdered Na_2CO_3	91	23	76

Figure 13 and Figure 14 show the volume and number distributions, respectively, for the large Mn_3O_4. These relative log-linear plots have the cumulative distribution on the right y-axis. Because of the relatively large particle size, a good separation was obtained from sieving. The size distribution is relatively narrow, with some small particles contaminating the sample as seen in the number distribution. However, greater than 80% of the particles, by volume or number, are between 195 and 252μm in diameter.

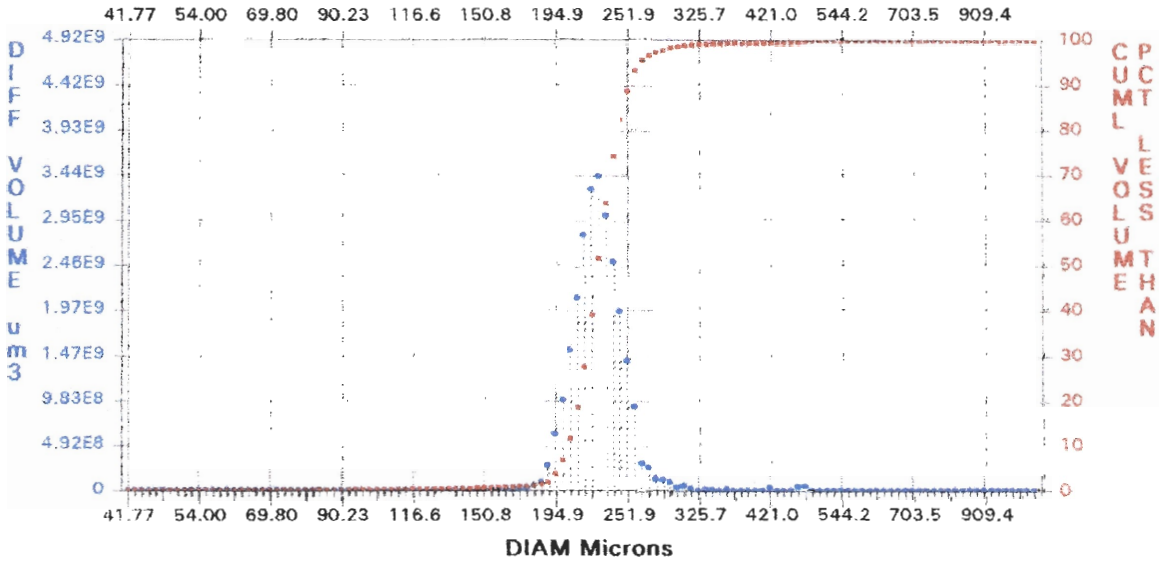

Figure 13 Volume particle size distribution for large Mn_3O_4.

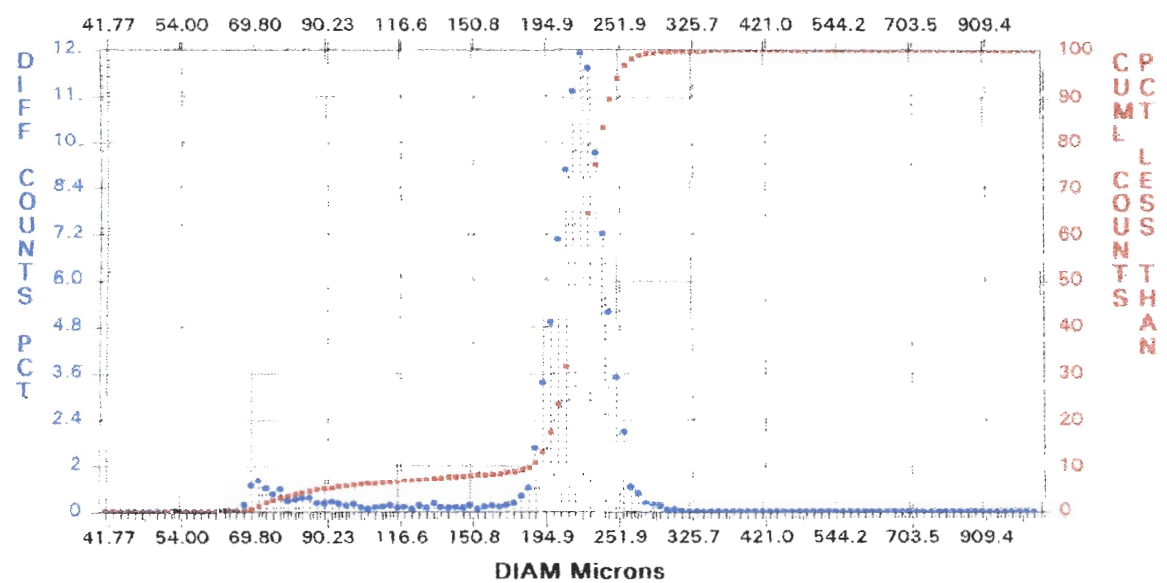

Figure 14 Number particle size distribution for large Mn_3O_4.

The medium fraction, Figure 15 and Figure 16, is also comprised of a relatively narrow distribution. However, there is some contamination with 10-30μm particles as seen in the number distribution, Figure 16. These small particles accounted for 33% of the total number of particles, reducing the number mean size below the lower sieve size of 90μm. Because of the small size of the contaminants, the volume distribution does not appear to be greatly affected.

The small particle size distribution has a highly skewed appearance as seen in Figure 17 and Figure 18. The resulting volume and number mean particle sizes are therefore very different. This material was classified by passing through a 38μm screen, so there is a relatively clean separation at the large end of the distribution. The volume distribution shows that there is some contamination of larger particles, but the numbers appear insignificant. 80% of the material by volume is between 8 and 38μm while 80% of the particles are between 2 and 6μm.

The powdered Mn_3O_4, Figure 19 and Figure 20, was used as received from the manufacturer. The particle sizes below 0.7μm were estimated because they were out of the recommended range of detection for the apparatus. The particle sizes ranged from 0.1 to 15μm. 80% of the material by volume is between 0.5 and 6μm. It is estimated that 80% of the particles are between 0.1 and 0.4μm in diameter.

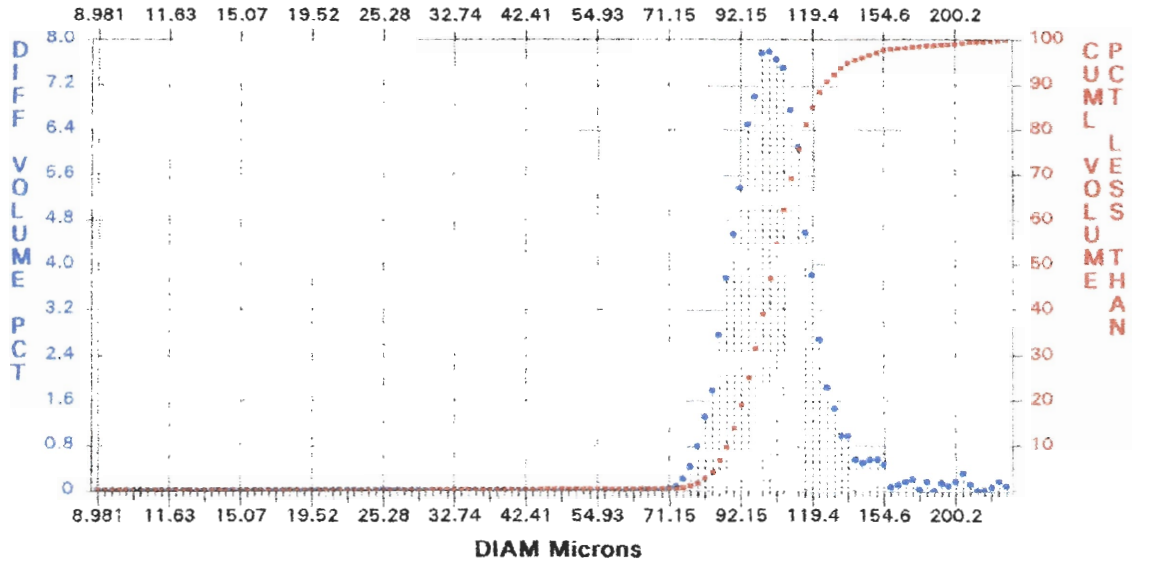

Figure 15 Volume particle size distribution for medium Mn_3O_4.

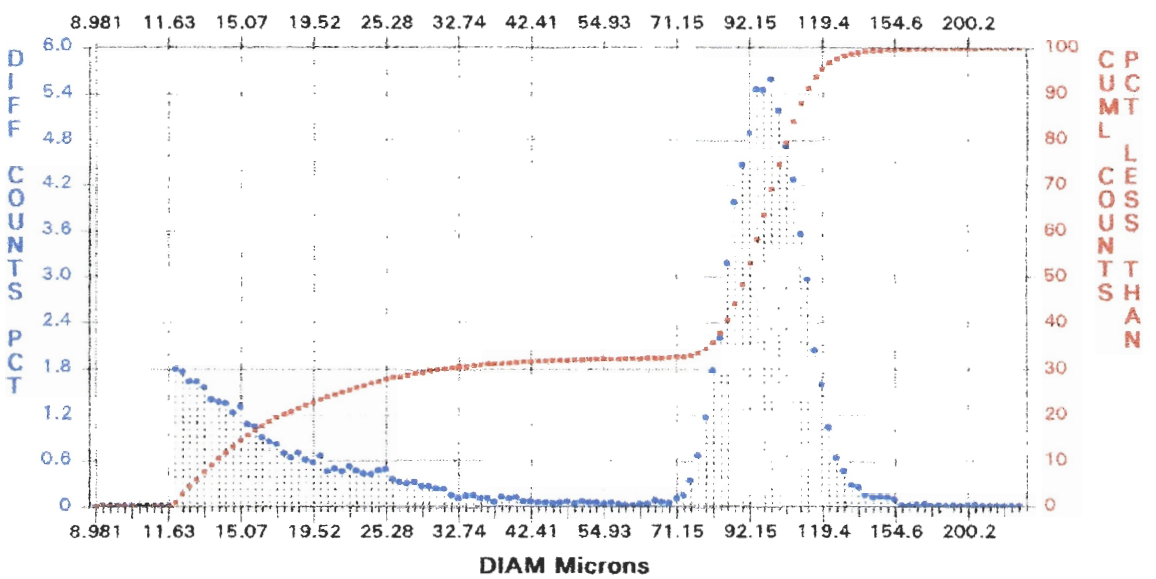

Figure 16 Number particle size distribution for medium Mn_3O_4.

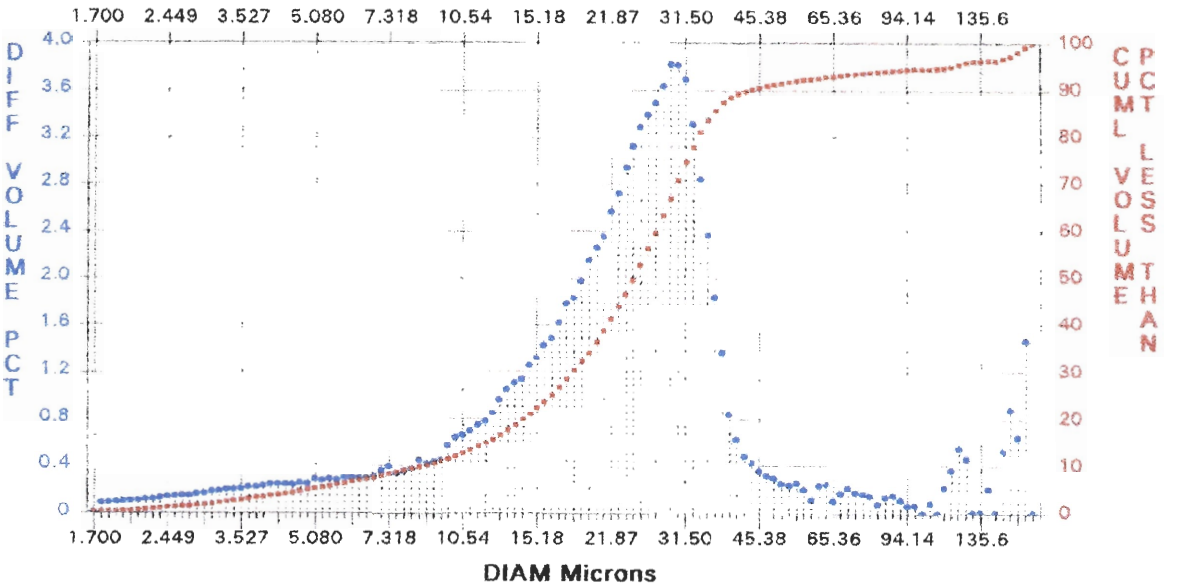

Figure 17 Volume particle size distribution for small Mn_3O_4.

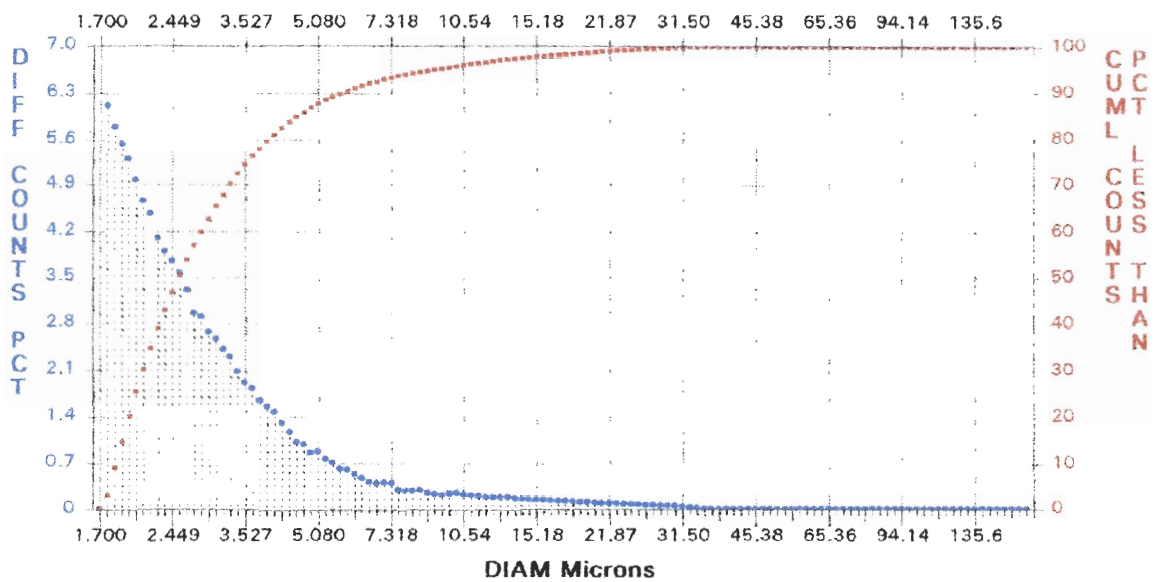

Figure 18 Number particle size distribution for small Mn_3O_4.

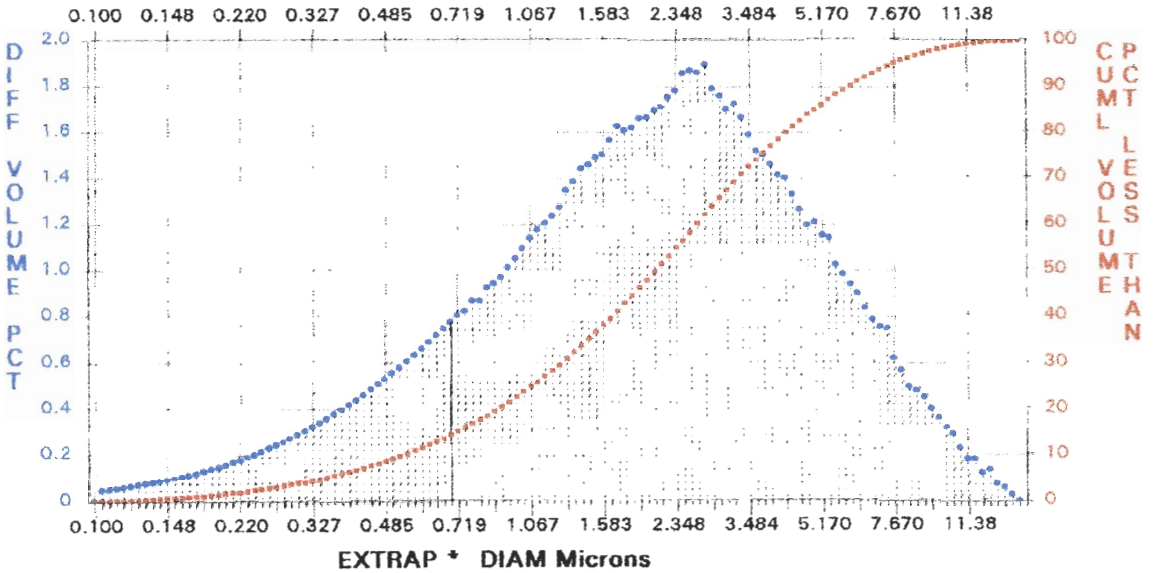

Figure 19 Volume particle size distribution for powdered Mn_3O_4.

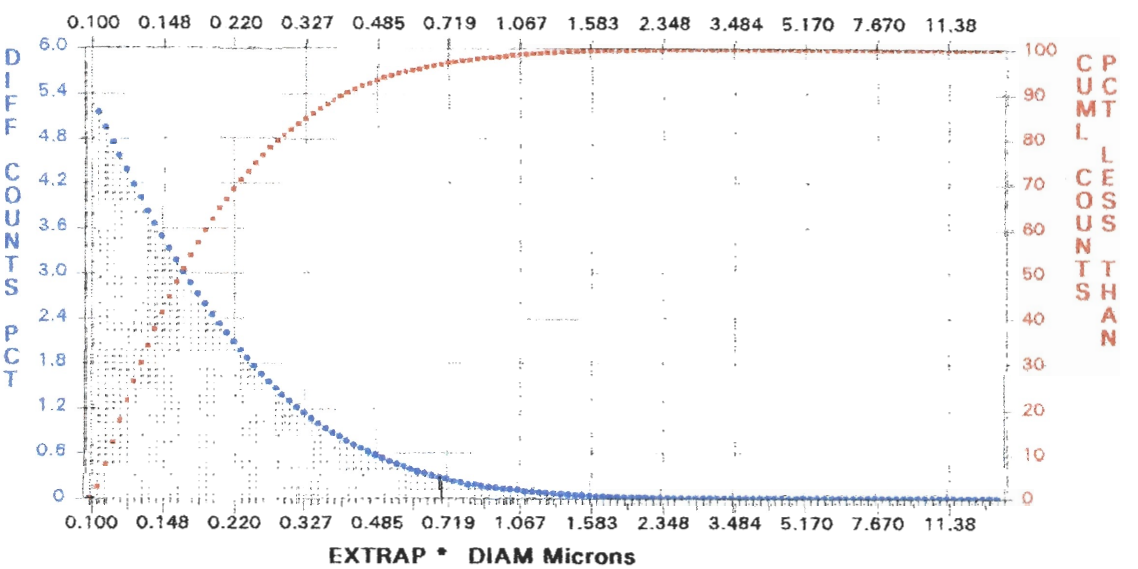

Figure 20 Number particle size distribution for powdered Mn_3O_4.

The Na_2CO_3 was not sieved before use and therefore has a relatively wide distribution of particle sizes as shown in Figure 21 and Figure 22. 80% of the material by volume is between 42 and 185μm while 80% of the particles are between 10 and 57μm in diameter.

SEM Characterization

The reactants were observed with scanning electron microscopy to qualify the surface structure. The Mn_3O_4 was found to have different structures depending on the size fraction. This was due to the mechanical treatment of grinding, and the manufacturing method.

The large Mn_3O_4 is shown in Figure 23 and Figure 24 at 50x and 250x magnification, respectively. These particles are made from groups of elongated rectangular structures that are intertwined in no apparent particular pattern. The normal crystal structure of Mn_3O_4 is the same as MnO_2, tetragonal. Mn_2O_3 and MnO exhibit cubic crystal structures.[43] Some of the pieces of the particles appear plate-like. The surfaces of the particle components appear relatively flat and smooth. The medium Mn_3O_4, Figure 25 and Figure 26, is very similar to the large Mn_3O_4 except for the size.

The small Mn_3O_4, Figure 27 and Figure 28, was obtained from grinding particles that passed through the 90μm screen when fractionating the medium Mn_3O_4. The particles appear to be broken fragments of the larger particles. The small Mn_3O_4 is not made of dismantled larger particles, but rather dismantled and broken larger particle

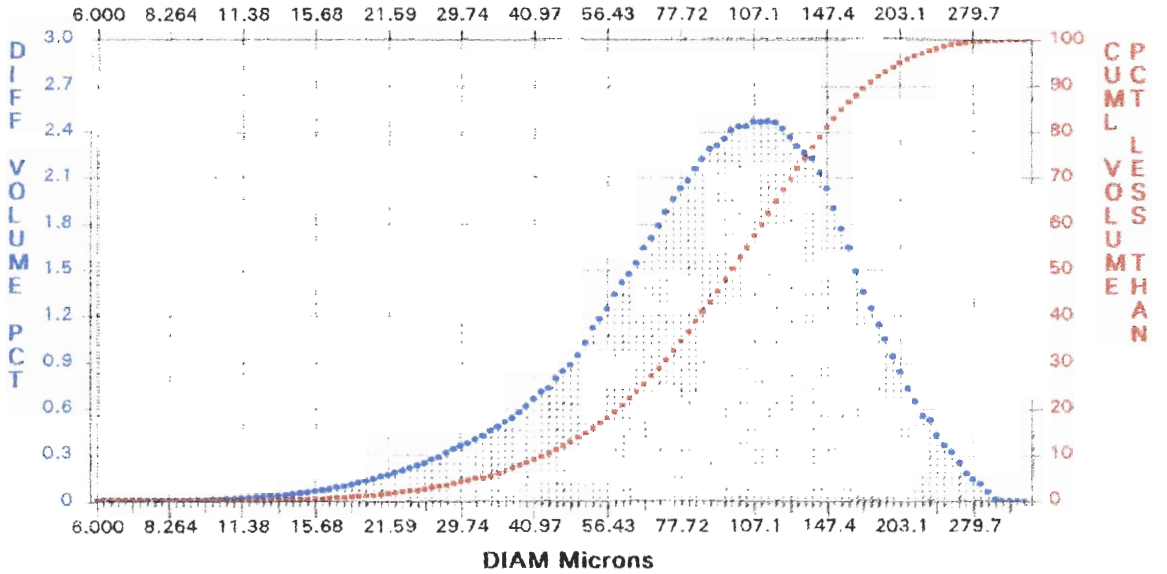

Figure 21 Volume particle size distribution for powdered Na_2CO_3.

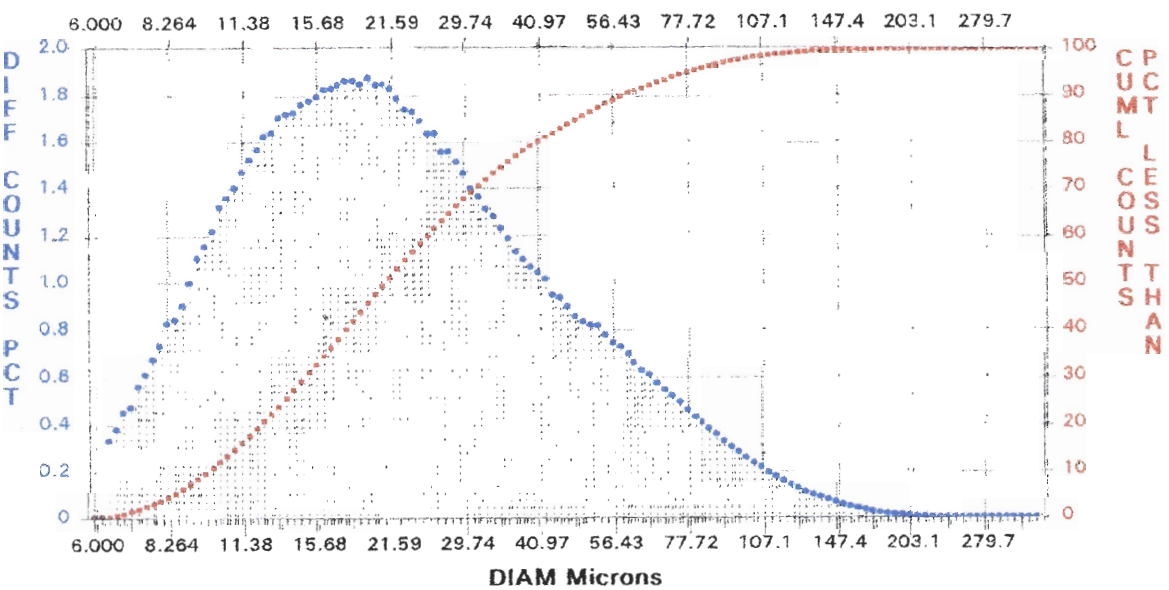

Figure 22 Number particle size distribution for powdered Na_2CO_3.

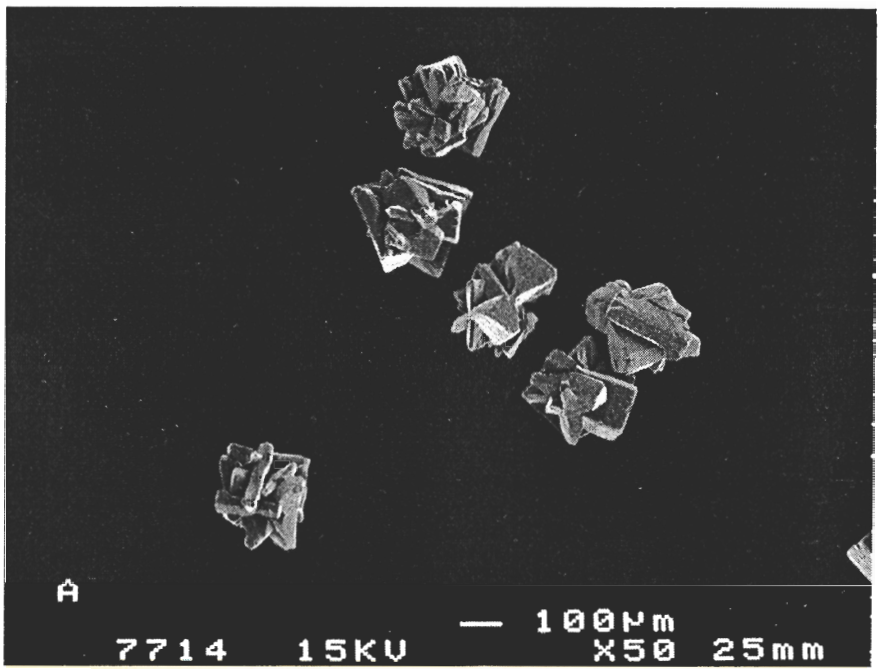

Figure 23 SEM image of large Mn_3O_4. 50x magnification.

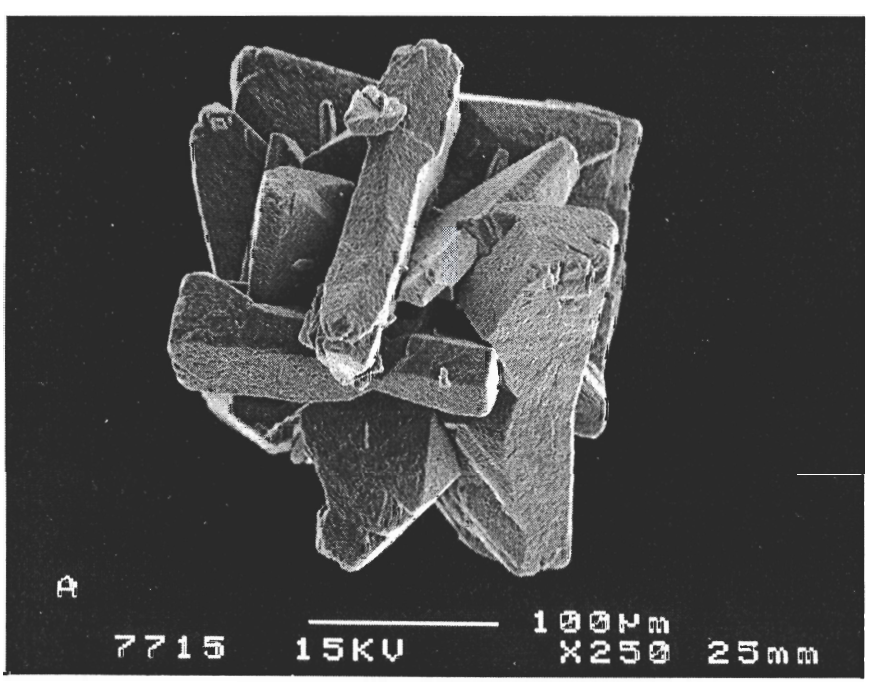

Figure 24 SEM image of large Mn_3O_4. 250x magnification.

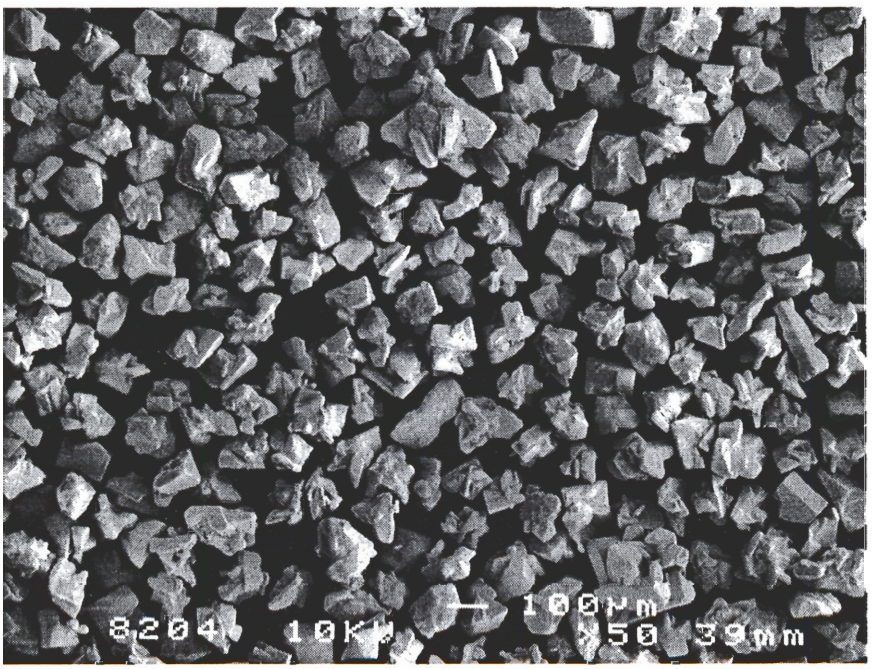

Figure 25 SEM image of medium Mn_3O_4. 50x magnification.

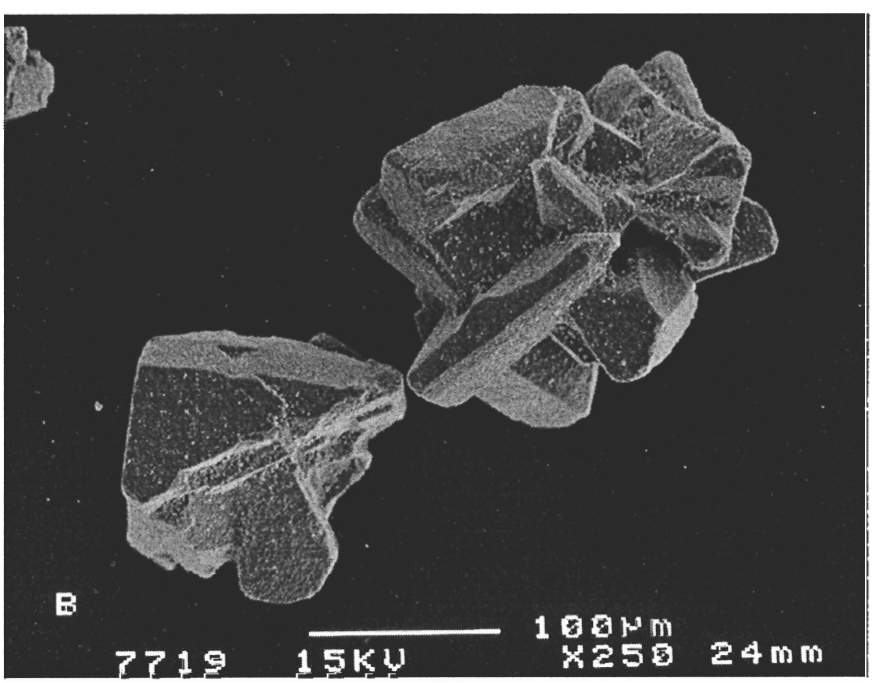

Figure 26 SEM image of medium Mn_3O_4. 250x magnification.

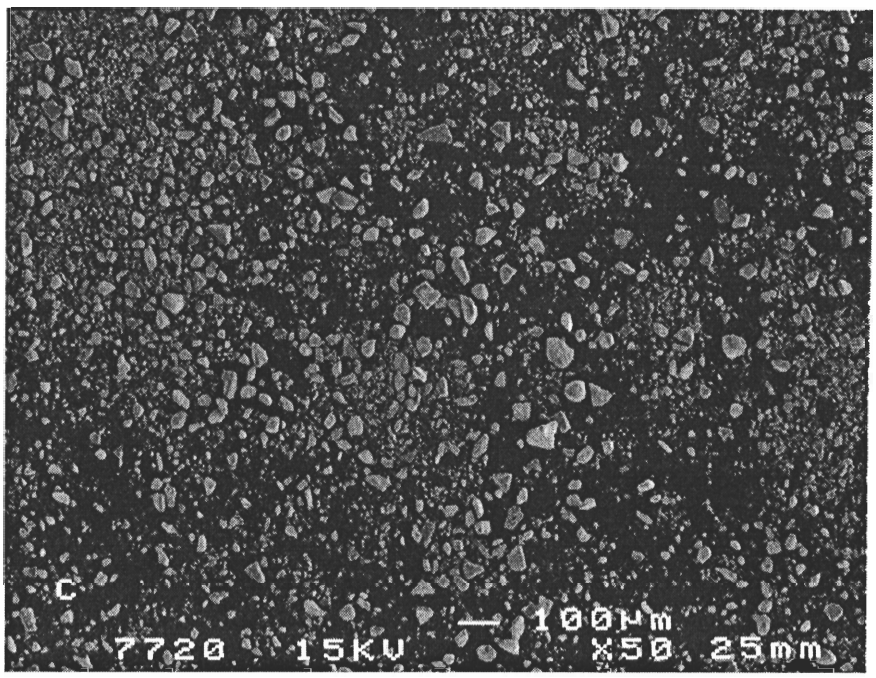

Figure 27 SEM image of small Mn_3O_4. 50x magnification.

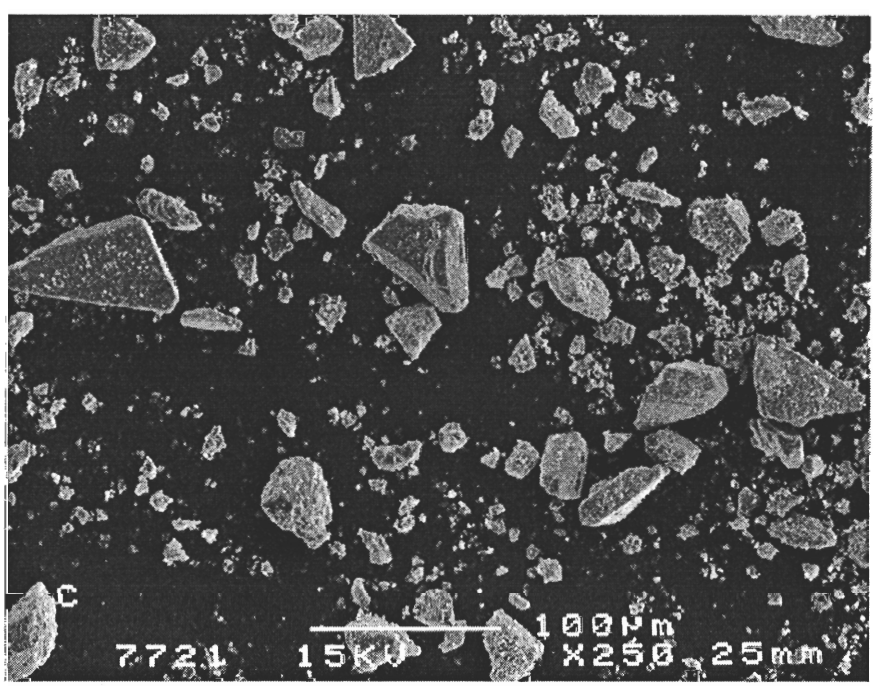

Figure 28 SEM image of small Mn_3O_4. 250x magnification.

structures. The elongated rectangular and plate-like pieces were reduced in size to obtain the small Mn_3O_4 fraction.

The powdered Mn_3O_4 particles, Figure 29 and Figure 30, are primarily less than 1μm in diameter. The powdered Na_2CO_3 particles, Figure 31 and Figure 32, appear similar to the small Mn_3O_4 particles. However, the surface of the powdered Na_2CO_3 has smoother edges than the small Mn_3O_4. The 250x magnification shows that the particle surface is not as smooth as the large and medium Mn_3O_4.

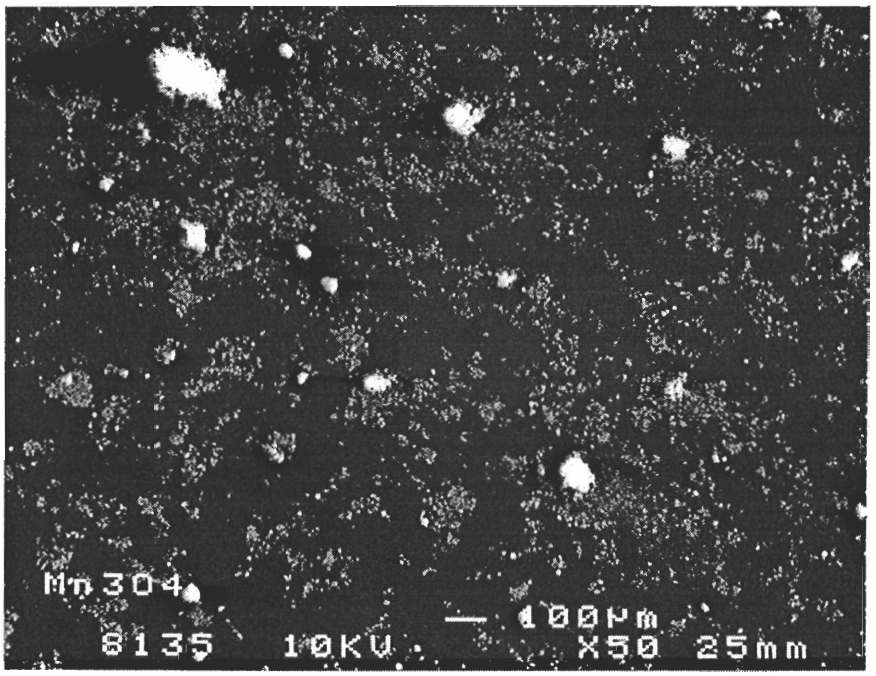

Figure 29 SEM image of powdered Mn_3O_4. 50x magnification.

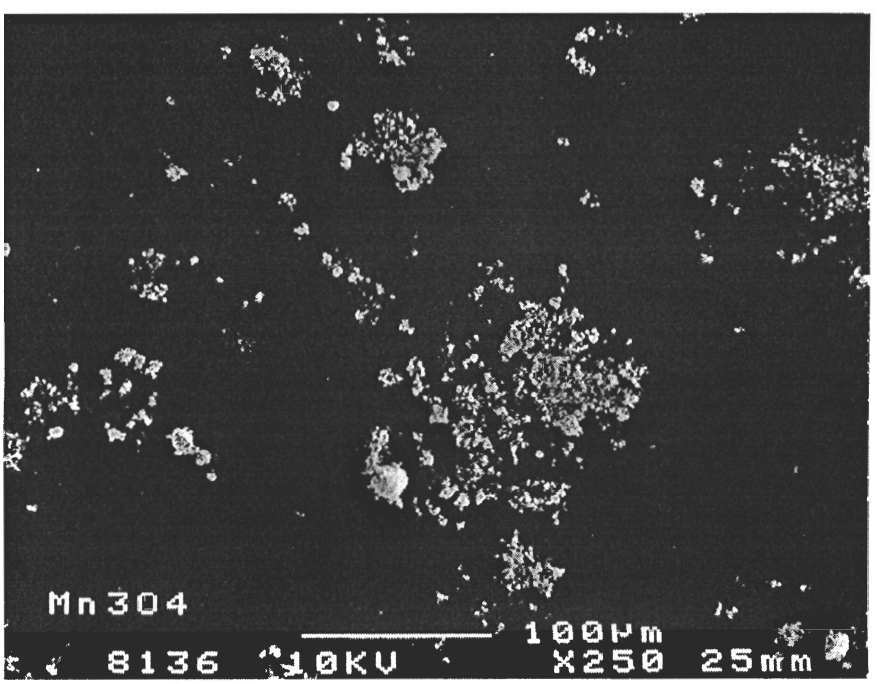

Figure 30 SEM image of powdered Mn_3O_4. 250x magnification.

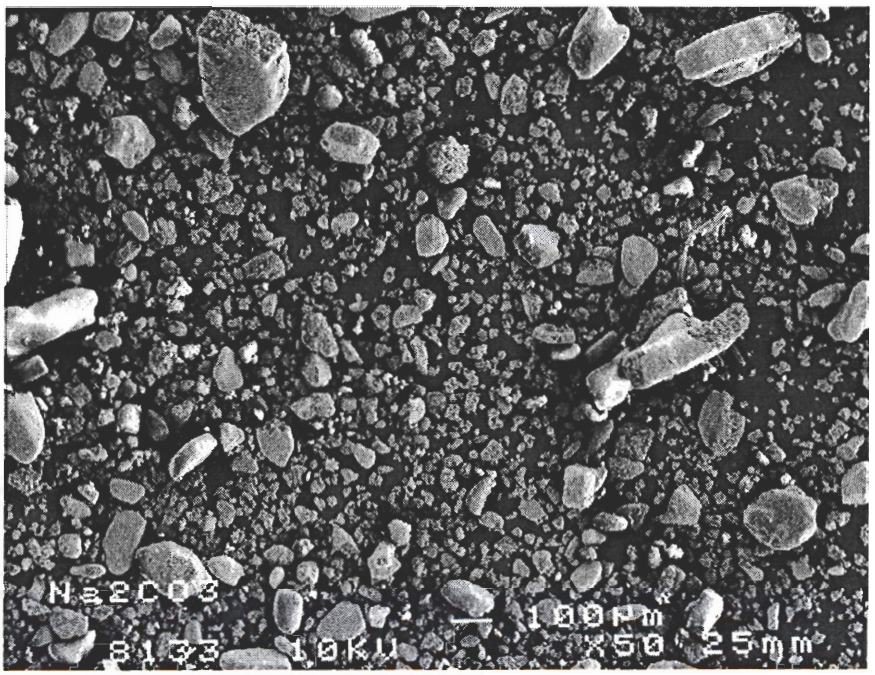

Figure 31 SEM image of powdered Na_2CO_3. 50x magnification.

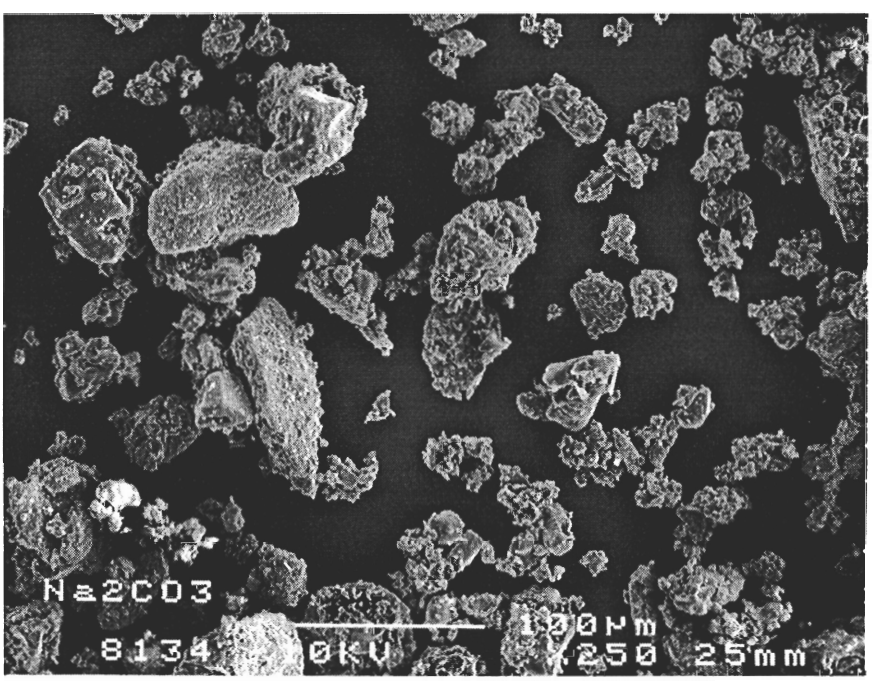

Figure 32 SEM image of powdered Na_2CO_3. 250x magnification.

STOICHIOMETRY OF REACTION

The stoichiometry of the reaction between Na_2CO_3 and Mn_3O_4 was hypothesized to occur according to the following reaction.

Equation 27 $$Na_2CO_3 + Mn_3O_4 \Rightarrow Na_2O \cdot Mn_3O_4 + CO_2$$

The solid product, $Na_2O{\cdot}Mn_3O_4$, was initially assumed to form in a 1:1 ratio, unlike the TiO_2 based direct causticizing system. A series of reactions with different initial molar ratios, Mn_3O_4:Na_2CO_3, at different temperatures was done to try and confirm the above hypothesis. Mixtures of the powdered Mn_3O_4 and Na_2CO_3 were prepared with various initial molar ratios. The samples were placed in alumina crucibles in a nitrogen-purged furnace. Three temperatures were investigated, 700, 800, and 900 °C. The experiments were left to run for 24, 12, and 1 hours respectively to ensure complete conversion of the reactants. Following the heating, the crucibles were cooled in a dessicator then weighed to determine the weight loss. Na_2CO_3 conversions were calculated based on the weight loss, assuming all weight loss was due to the evolution of CO_2. A plot of Na_2CO_3 conversion versus the initial molar ratio of reactants is shown in Figure 33.

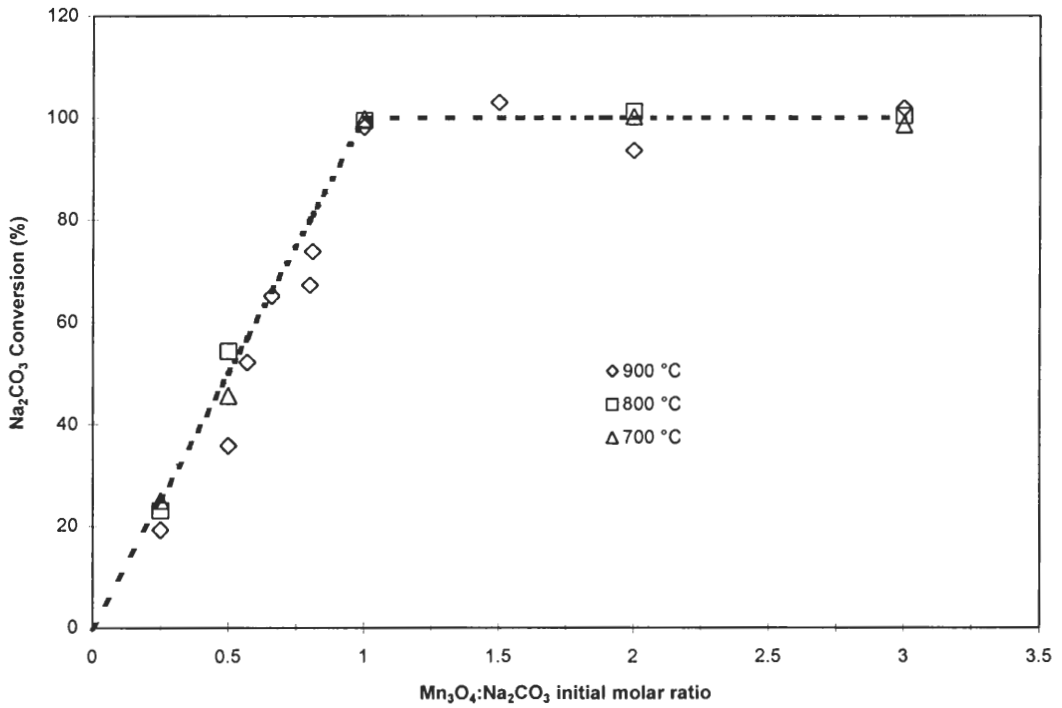

Figure 33 Na_2CO_3 conversion versus Mn_3O_4:Na_2CO_3 initial molar ratio at 700, 800, and 900 °C.

The dashed line in Figure 33 represents the theoretical conversion for 1:1 stoichiometry. When there is an excess of Na_2CO_3 present in the reaction mixture, for Mn_3O_4:Na_2CO_3 less than 1, the Na_2CO_3 conversion approaches the theoretical maximum based on 1:1 reaction stoichiometry. If more Na_2CO_3 were able to react, higher weight losses would have been recorded. For initial molar ratios greater than 1:1, the limiting reactant is Na_2CO_3, resulting in weight loss equivalent to 100% conversion. The same stoichiometry was observed to happen for the three temperatures.

KINETICS

Determining A Suitable Kinetic Model

At the start of the reaction the material must be heated quickly to the temperature of interest, and then maintained for the duration of the experiment. The initial heating is known as an induction period. During heating, the surface diffusion of reactants is starting to occur, along with the nucleation and growth of reaction centers. The models presented in the literature review are all based on isothermal reactions and therefore not applicable in this region. The induction period for experiments in the solid state was a very small fraction of the total experimental time as shown in Figure 34. This figure shows only the first part of the experiment, which continued for over 26,000 seconds.

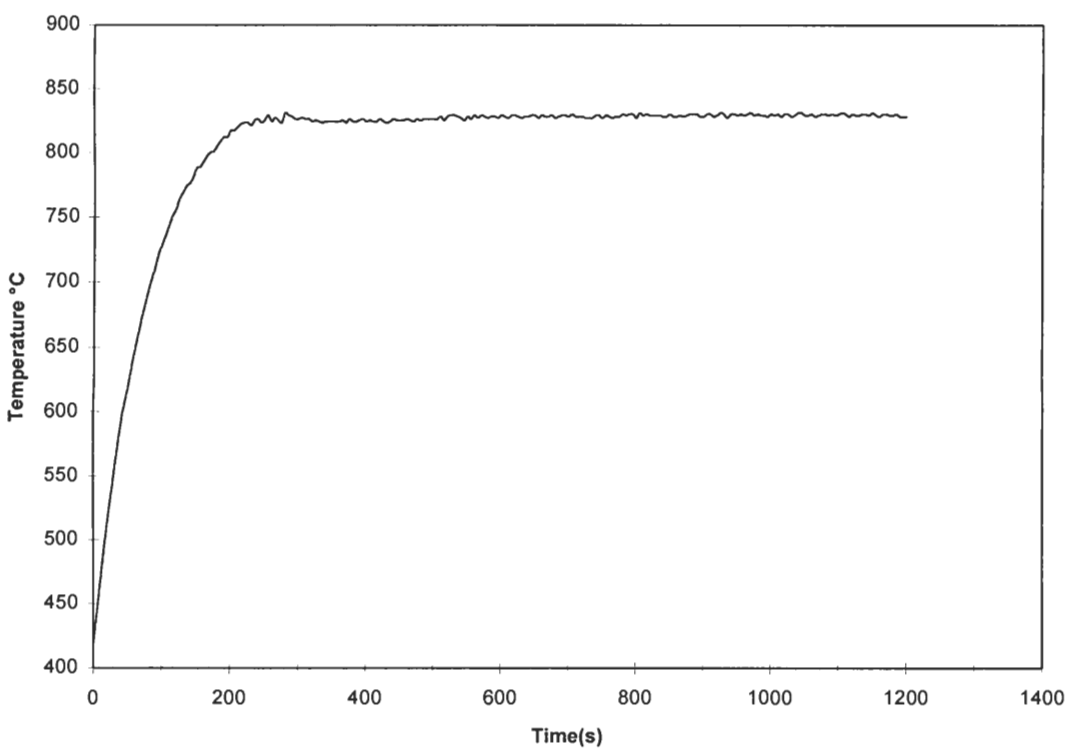

Figure 34 Initial Temperature Profile in Reactor.

In Figure 35 the CO_2 concentration in the gas leaving the reactor for a typical reaction is shown. The concentration rises very quickly then steadily declines. This shows how the reaction is deceleratory. Integration of the area under the CO_2 concentration curve multiplied by the gas flow rate led to the total moles of CO_2 produced.

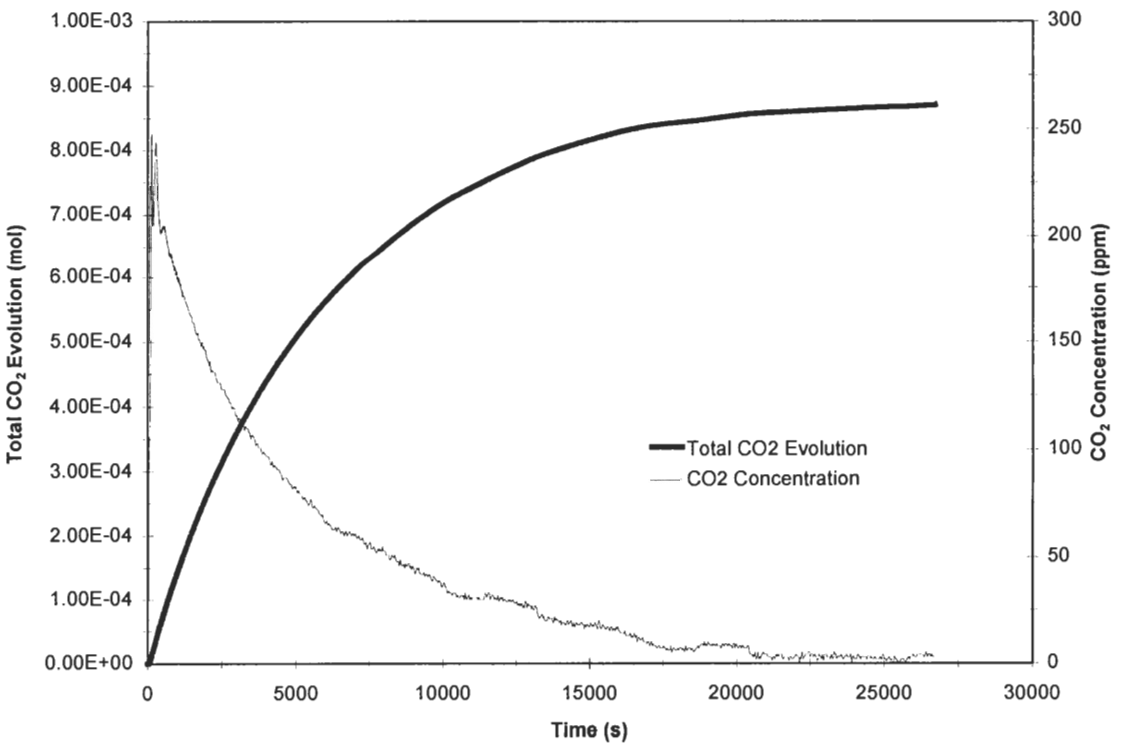

Figure 35 CO_2 Concentration and Total CO_2 Evolution versus time. 827 °C, Mn_3O_4:Na_2CO_3 = 3:1, medium Mn_3O_4, powdered Na_2CO_3.

The total CO_2 evolution data was divided by the initial number of moles of Na_2CO_3 to obtain the Na_2CO_3 conversion. This is shown in Figure 36 along with the Mn_3O_4 conversion that was calculated from stoichiometry. In this case, there was an initial molar ratio of Mn_3O_4:Na_2CO_3 3:1. Complete conversion of the Na_2CO_3 results in

one third of the Mn_3O_4 reacting. Overall the shapes of the curves are deceleratory. The slope decreases with increasing time. This suggests that the reaction is limited by product layer diffusion. As the reaction proceeds, the product layer becomes thicker, increasing the diffusion path and slowing the rate of conversion.

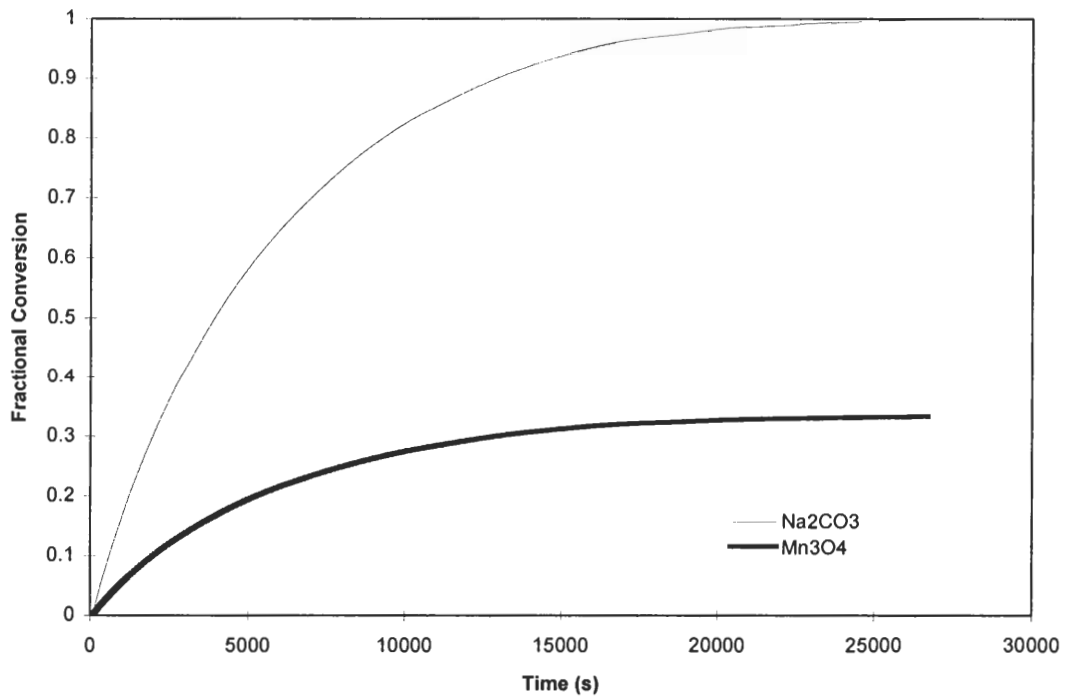

Figure 36 Conversion of Na_2CO_3 and Mn_3O_4 versus time. 827 °C, Mn_3O_4:Na_2CO_3 = 3:1, medium Mn_3O_4, powdered Na_2CO_3.

The conversion versus time data was used to see which kinetic models best described the process. The f(α) versus time curves were constructed to test the models. The geometric model for contracting area and Ginstling-Brounshtein model were found to have linear sections for the initial and middle parts of the reaction, respectively. Figure 37 is a normalized plot for the contracting area (Equation 13) and Ginstling-Brounshtein (Equation 19) models versus time. This was constructed from the raw

conversion versus time data and appears continuous because of the high sampling rate of the data acquisition. From Figure 37 it can be seen that the contracting area model is linear at low conversions. It then has a steady decrease in slope. The G-B model produces a sigmoidal curve with a linear section extending from approximately 2,000 to 10,000 seconds.

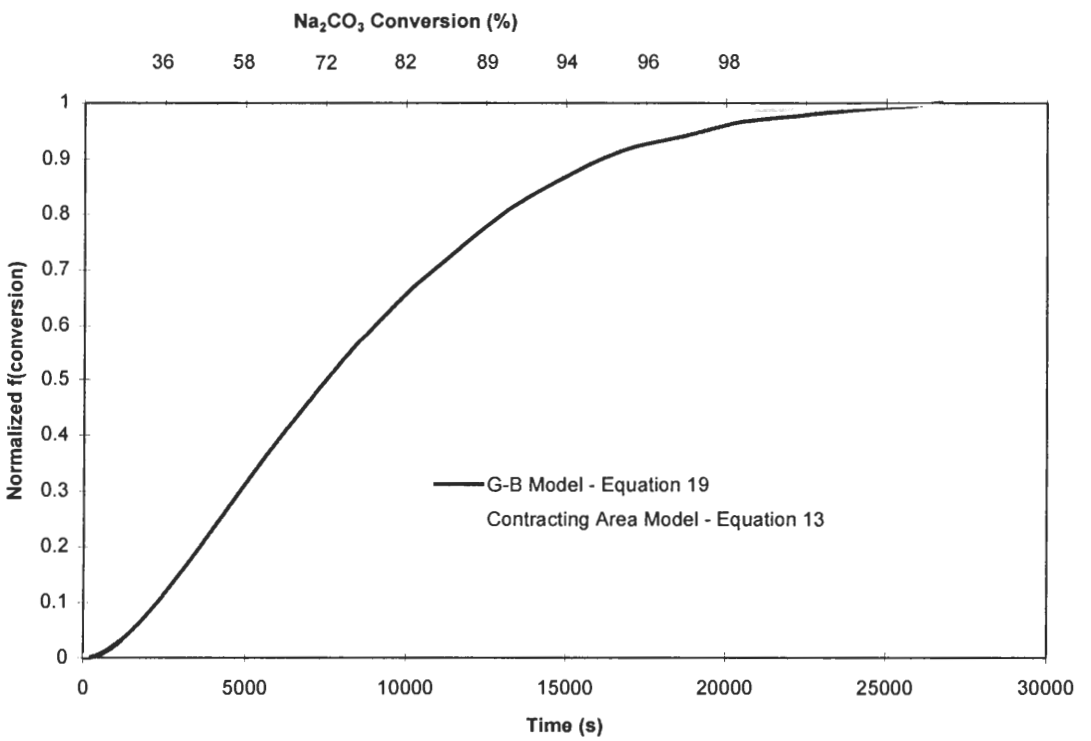

Figure 37 The Ginstling-Brounshtein and contracting area models calculated from the continuous conversion versus time data. 827 °C, Mn_3O_4:Na_2CO_3 = 3:1, medium Mn_3O_4, powdered Na_2CO_3. G-B Model = $1-2/3\alpha-(1-\alpha)^{2/3}$, Contracting Area Model = $1-(1-\alpha)^{1/2}$

The linear range of the G-B model was determined by the method previously described. The derivative of the G-B curve was calculated by taking the slope between each successive data point. It was then graphed versus time. The maximum of the derivative curve indicated the inflection point in the linear region of the G-B versus time curve. A value of 80% of the maximum was selected on both sides of the peak. The

corresponding times, and thus conversions, were set as the limit for applicability of the model. For the example in Figure 38, the limits of 1800-8610 seconds correspond to the 80% times. The conversion range is 28-77% and 9-26% for Na_2CO_3 and Mn_3O_4 respectively.

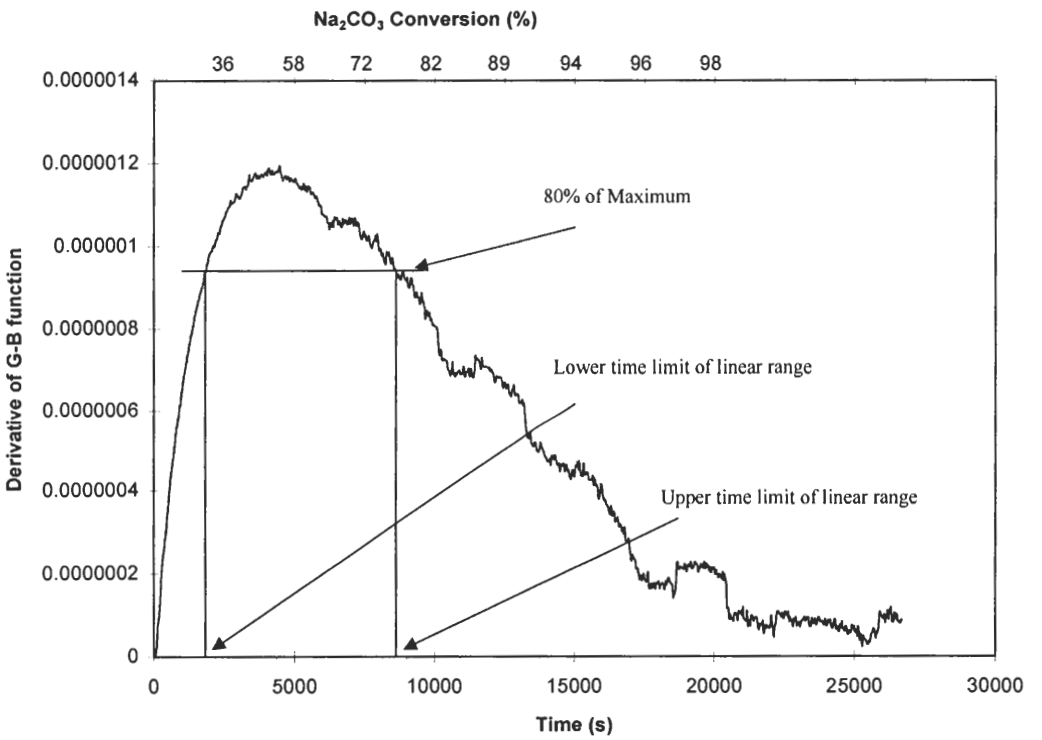

Figure 38 The derivative of the Ginstling-Brounshtein equation versus time. 827 °C, Mn_3O_4:Na_2CO_3 = 3:1, medium Mn_3O_4, powdered Na_2CO_3.

A graph of the G-B model, calculated from the experimental data, applied over Na_2CO_3 conversions from 28-77% is shown in Figure 39. The y-axis scale is different than Figure 37 because the data was not normalized in this case. Excellent linearity is found over the range of 28-77% Na_2CO_3 conversion. The slope of the line is equal to the reaction rate constant, k.

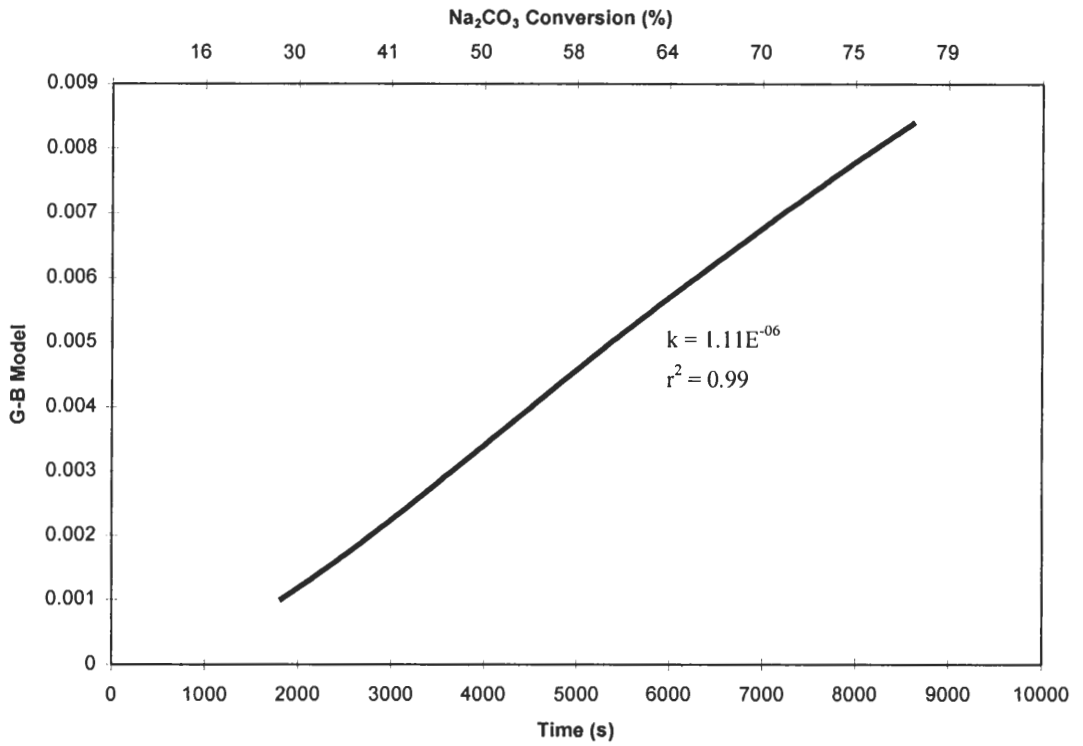

Figure 39 Ginstling-Brounshtein model, calculated from experimentally determined conversion versus time data, applied over 28-77% conversion of Na_2CO_3. 827 °C, Mn_3O_4:Na_2CO_3 = 3:1, medium Mn_3O_4, powdered Na_2CO_3. The line appears continuous because of the high sampling rate of the data acquisition. G-B Model = $1-2/3\alpha-(1-\alpha)^{2/3}$

The G-B model does not provide a linear fit for the initial part of the reaction as previously shown in Figure 37. The initial part of the reaction is assumed to commence after the reactor has reached isothermal conditions. In this example, it is after approximately 240 seconds as shown in Figure 34.

The deceleratory contracting area model, Equation 13, was found to have the best fit for the initial part of the reaction. The contracting area model is applied in the range of 4-28% conversion of Na_2CO_3 and shown in Figure 40. The slope of the line, calculated from the least squares linear fit, represents the reaction rate constant, k.

The reaction rate constant for the initial part of the reaction will be called k_i. The Ginstling-Brounshtein kinetic rate constant refers to a product layer diffusion controlled reaction and will be called k_d. For the above example, $k_i=2.66x10^{-5}$ and $k_d=1.11x10^{-6}$ s^{-1}. The kinetic rate constants can not be directly compared because they are from different physical models.

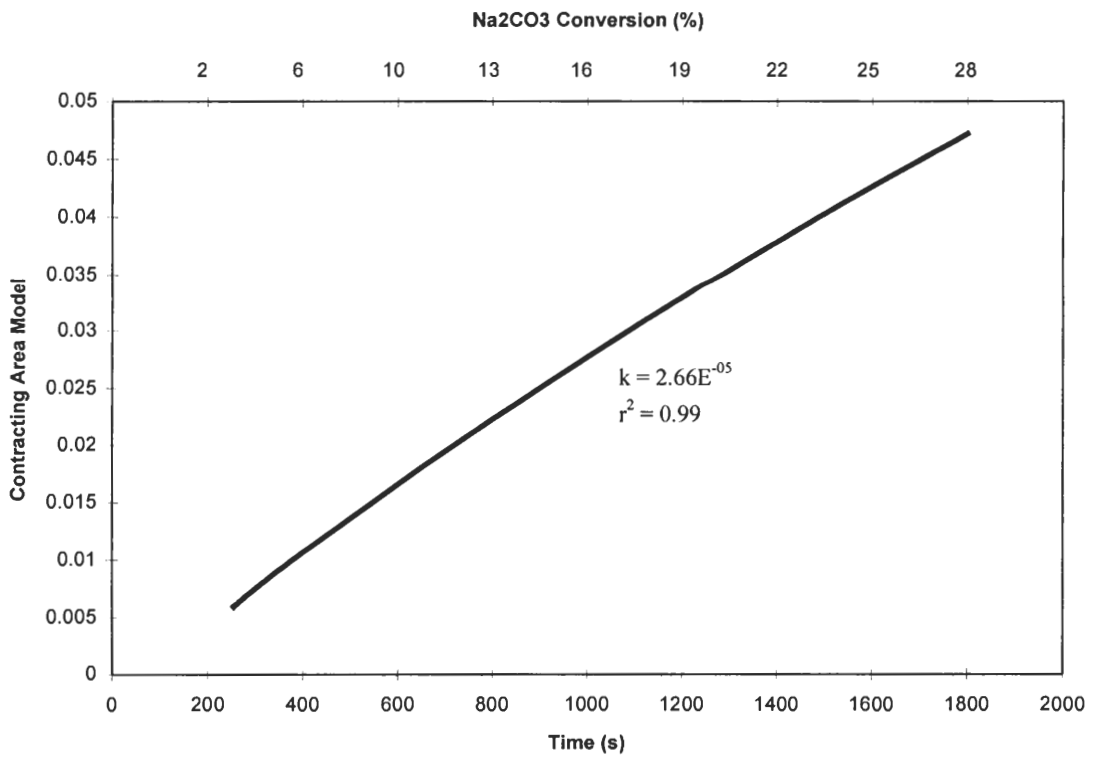

Figure 40 Contracting Area model, calculated from experimentally determined conversion versus time data, applied to the initial part of the reaction. 827 °C, Mn_3O_4:Na_2CO_3 = 3:1, medium Mn_3O_4, powdered Na_2CO_3. The line appears continuous because of the high sampling rate of the data acquisition. Contracting Area Model = $1-(1-\alpha)^{1/2}$

The initiation period was not found with all experiments. It was only found with the medium and large diameter Mn_3O_4 reactions. For the small and powdered Mn_3O_4 particles, the G-B model was generally found to fit the data from the time that isothermal conditions were obtained. Figure 41 shows the G-B model applied to the data for the

experiment at 827 °C with Mn_3O_4:Na_2CO_3 = 3:1, and small Mn_3O_4 with powdered Na_2CO_3. This is similar to the first example except for the particle size. In this example, the 80% range from the derivative of the G-B curve yields a Na_2CO_3 range of conversion from 11-60%.

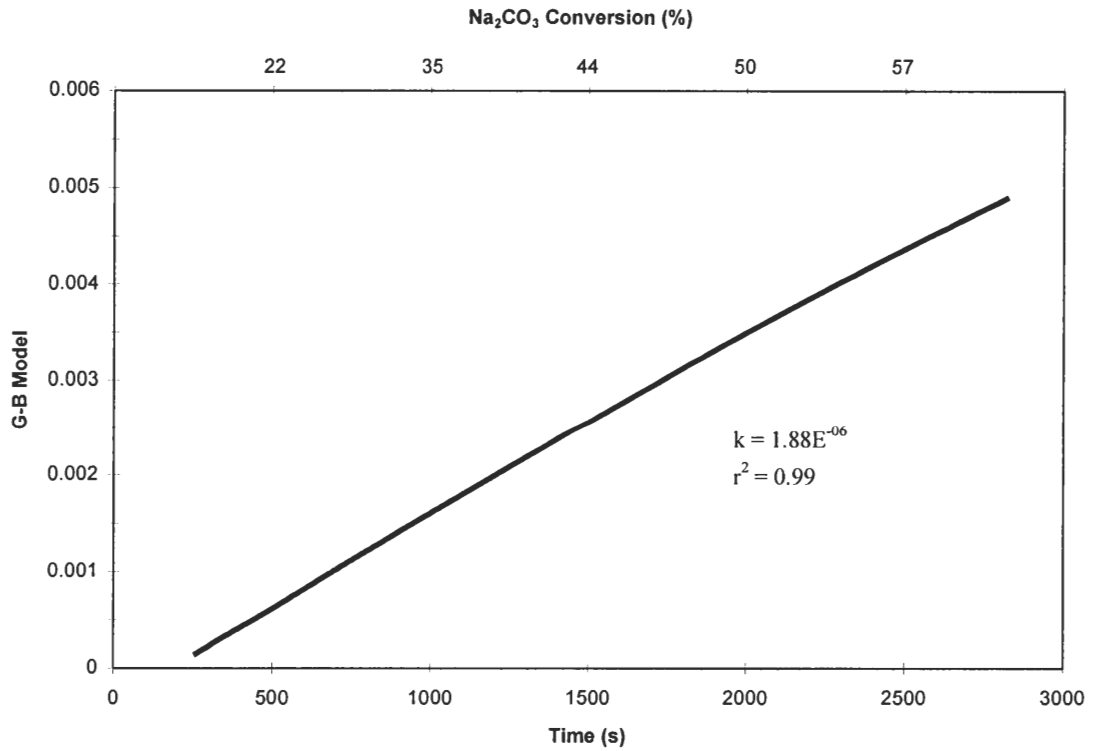

Figure 41 Ginstling-Brounshtein model, calculated from experimentally determined conversion versus time data, applied over 11-60% conversion of Na_2CO_3. 827 °C, Mn_3O_4:Na_2CO_3 = 3:1, small Mn_3O_4, powdered Na_2CO_3. The line appears continuous because of the high sampling rate of the data acquisition. G-B Model = $1-2/3\alpha-(1-\alpha)^{2/3}$

The absence of an initiation period with the small and powdered Mn_3O_4 particles is probably attributed to the differences in morphology as shown in the scanning electron micrographs presented in a previous section. The smaller particle sizes have relatively smooth surfaces when compared to the medium and large Mn_3O_4 particles. The G-B model is based on spherical particles. The smaller particles probably better approximate

spheres than the larger particle sizes. Even though the larger particles are overall spherical in shape, they appear to be comprised of rod-like crystals. These rod-like crystals have a two-dimensional structure. It is believed that the larger particles initial reaction proceeds according to the two-dimensional contracting volume model, reacting with the crystals that are exposed and sticking out from the surface of the particle. Following this initial step, the reaction then continues as if the particle were a sphere, in agreement with the G-B model. Because of the rod-like structures sticking out of the surface of the large and medium particles, there is greater surface area per effective particle diameter, and it takes longer to develop a uniform surface coverage of Na_2CO_3. A schematic of this process is shown in Figure 42.

Using the method described above, kinetic rate constants were obtained for the product layer diffusion controlled regime, and the initial part of the reaction, where appropriate, for all of the isothermal kinetic experiments. These kinetic rate constants were used to evaluate the effects of temperature, particle size, and initial amount of reactants on the direct causticizing reaction.

Small and Powdered Mn_3O_4

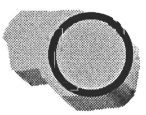

Particles initially approximate spheres, having good agreement with G-B model

Medium and Large Mn_3O_4

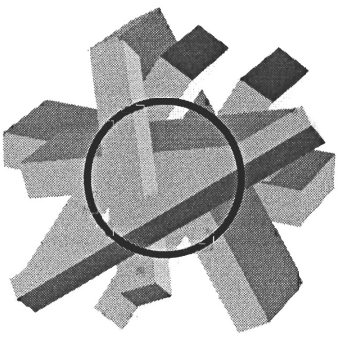

Initially reaction proceeds according to contracting area model, reacting outside of the dark circle, then it changes to the spherical G-B model

Figure 42 Schematic of the proposed reaction mechanisms for different particle morphologies.

Effect of Temperature

An important parameter in chemical reactions is the temperature. For solid-solid reactions, increases in temperature generally lead to an increase in the overall rate of reaction. This occurs because solid-solid reactions are usually limited in rate by the diffusion of the diffusing species through the product layer. The overall rate of reaction is therefore related to the diffusivity of the diffusing species through the product layer. The diffusivity increases with increasing temperature, leading to higher overall rates of reaction.

Additionally, increases in temperature can lead to phase changes such as melting and vaporization. For the Mn_3O_4 and Na_2CO_3 based direct causticizing system, the melting point of Na_2CO_3 is an issue. It occurs at 850 °C and is depressed by the presence

of Na_2S. The melting of Na_2CO_3 will change the reaction system from solid-solid to solid-liquid. However, the reaction mechanism is likely to stay the same. The major difference is that the Na_2CO_3 will diffuse through the product layer as a liquid rather than solid. The barrier to diffusion, the product layer, will still remain. The G-B model is also valid for a diffusing species that is liquid. In fact, it is more likely to quickly satisfy the assumption of complete surface coverage of the reactant particle.

Temperature effects in chemical reactions are commonly described by the Arrhenius equation. It is an established method of reporting and comparing kinetic data.

Equation 28

$$k = Ae^{(-E/RT)}$$

A plot of ln k versus 1/T usually yields a straight line. The slope of the line has the units of T^{-1}. When the slope is multiplied by R, the universal gas constant, an activation energy, E, is obtained. The intercept yields the frequency factor, A.

The significance of the Arrhenius parameters when applied to solid-solid reactions is not exactly the same as for a reaction in the gas phase. The Arrhenius equation was originally developed from Boltzmann's Law and the kinetic theory of gases. When the process is controlled by the chemical reaction itself, the activation energy is the energy barrier that must be overcome for the transformation of reactants into products during the rate-limiting step. However, for a solid-solid reaction, the rate limiting step is controlled by diffusion, not reaction. In this case the activation energy

takes on a meaning related to diffusion. It has been described as the energy of "embrittlement" of the lattice and depends on the force of the bond between its structural elements.[44]

For gas phase reactions, the frequency factor is related to the frequency of collisions between molecules resulting in the reaction configuration. In the solid state, the reactants are essentially immobilized in the lattice structure, giving the frequency factor some other meaning. The value of the frequency factor for solid-solid reactions has been said to depend on the frequency of oscillations in the structural elements of the crystalline lattice and the average distance between their adjacent equilibrium positions.[44]

Others believe that E and A are not adequately described by theory for solid-solid reactions and should be given an empirical rather than theoretical significance.[24] However, because values of E and A are generally reported to describe solid-solid reactions, the convention will be followed here.

In reference to the definition of the G-B kinetic rate constant, Equation 18 on page 20, k is a function of the diffusivity, initial molar concentration of the diffusing species, molar volume of the product layer, and particle radius. The initial molar concentration of the diffusing species in solid-solid reactions is defined as the inverse molar volume of the species. It is a fixed quantity that is not affected by temperature, and is assumed to stay constant during the reaction. The molar volume of the product layer is also a physical parameter that does not change. The particle radius of the non-diffusing

species can be changed but it is not a function of temperature. The diffusivity is therefore the only parameter in the model affected by temperature. Temperature influences on the diffusivity can then be represented by the following relationship.

Equation 29

$$D = Ae^{\left(-E/RT\right)}$$

Experiments were conducted to investigate the kinetics of the reaction between Mn_3O_4 and Na_2CO_3 as solids and a melt. In the solid state, powdered Mn_3O_4 and powdered Na_2CO_3 were used with Mn_3O_4:Na_2CO_3 initial molar ratios of 1:4 and 1:1. The temperature range of 650 to 850 °C was investigated. In the molten state, the large Mn_3O_4 was used with powdered Na_2CO_3 and Mn_3O_4:Na_2CO_3 initial ratios of 1:1. The temperature range was 870 to 950 °C.

Figure 43 shows the Arrhenius plots for the reactions in the solid state. The slopes of –25,251±1047 and –24,468±3295 $°K^{-1}$ yield activation energies of 210±9 and 203±27 kJ/mol respectively. The intercepts of 14.016±1.021 and 11.376±3.213 yield frequency factors of $1.2x10^6$ and $8.7x10^4$ s^{-1} respectively. The difference in activation energies is within experimental error. However, the frequency factors are different as a result of different initial molar ratios of reactants. The larger frequency factor occurred when there was a stoichiometric excess of Na_2CO_3. This suggests that the frequency factor for the diffusivity, A, is a function of the initial molar ratio of reactants. This relationship will be investigated in a later section.

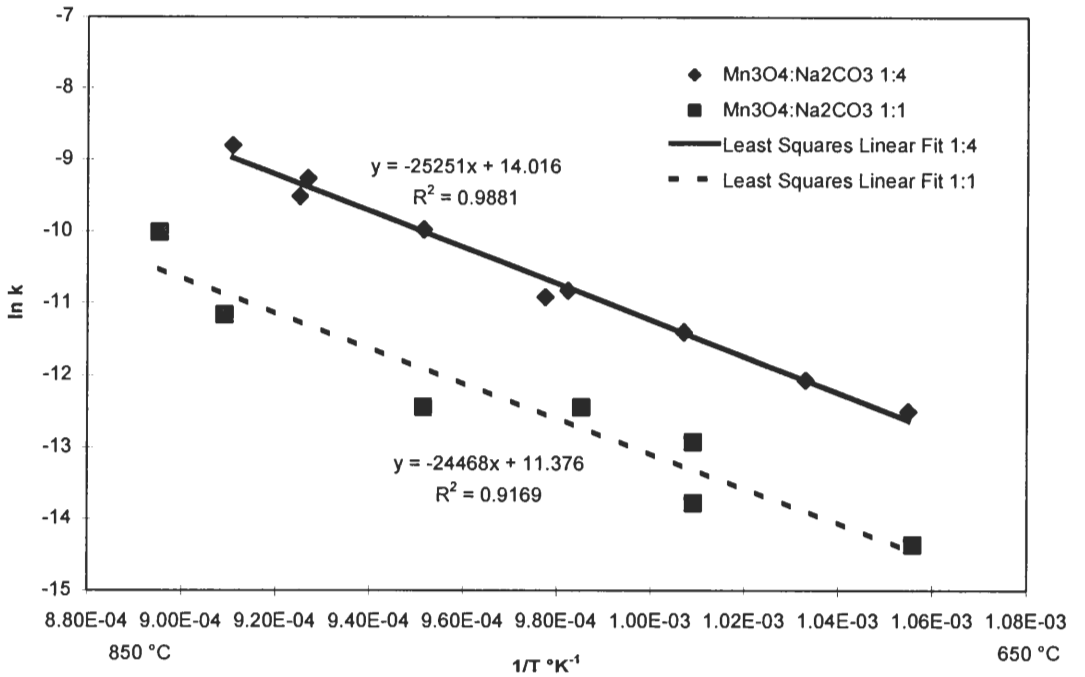

Figure 43 Arrhenius plot for solid-solid reaction. Temperature range 650-850 °C. Mn_3O_4:Na_2CO_3 initial molar ratios of 1:4 and 1:1. Mn_3O_4 and Na_2CO_3 powders.

The Arrhenius plot for the molten experiments is shown in Figure 44. From the slope of –20,872±980, an activation energy of 174±8 kJ/mol is obtained. This indicates that the barrier to diffusion has a smaller temperature dependence when the Na_2CO_3 is molten. However, a large increase in the kinetic rate constant occurs upon melting. The kinetic rate constant at 850 °C, extrapolated from the solid-solid data for a Mn_3O_4:Na_2CO_3 ratio of 1:1 and large Mn_3O_4 particles, is 6.34×10^{-6}. The kinetic rate constant at the same temperature, extrapolated from the molten data, is 2.58×10^{-4}. The transition from solid to molten Na_2CO_3 increases the reaction rate constant by 40 times at 850 °C. The frequency factor for the conditions in Figure 44 is 3.0×10^{4} s^{-1}.

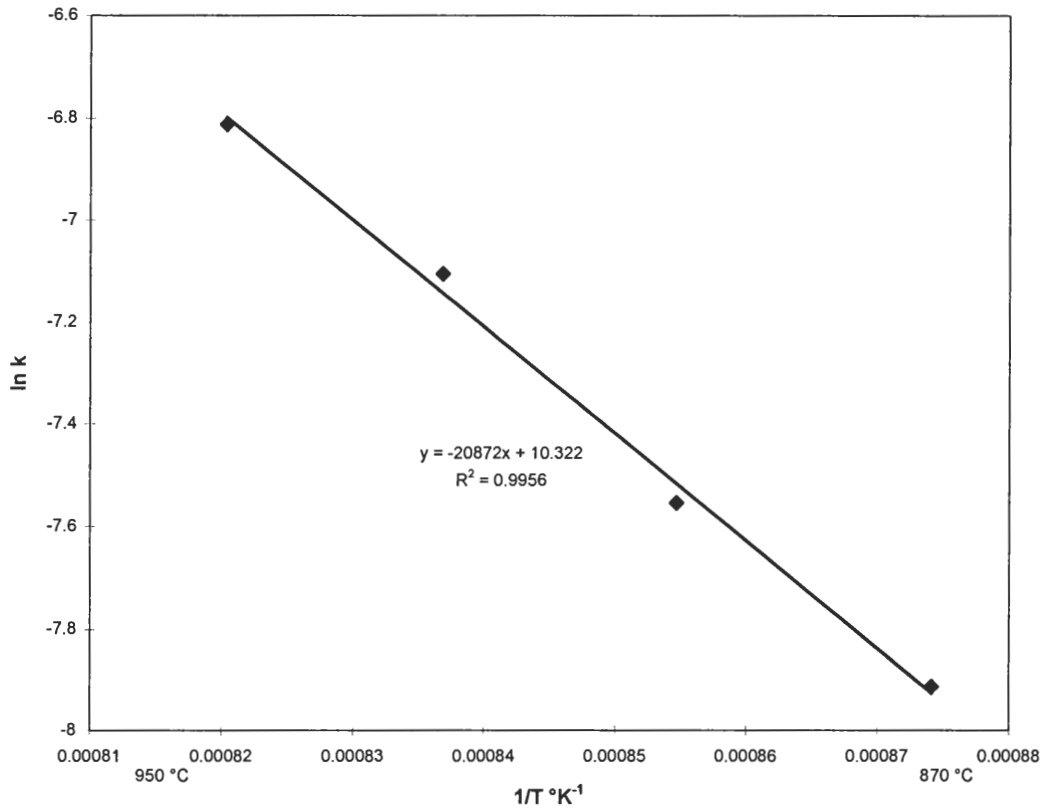

Figure 44 Arrhenius plot for solid-liquid reaction. Temperature range 870-950 °C. Mn_3O_4:Na_2CO_3 initial molar ratio of 1:1. Large Mn_3O_4 and powdered Na_2CO_3.

The values for the activation energies compare to findings of other authors for different systems. Zou reported an activation energy of 216 kJ/mol for the Na_2CO_3 and TiO_2 system.[19] Johnson and Gallagher[45] found that the Li_2CO_3 and Fe_2O_3 system obeyed the Ginstling-Brounshtein equation. A value of 210 kJ/mol for the activation energy was found over the temperature range 380 to 510 °C. They suggested that the Li_2CO_3 migrated to cover the Fe_2O_3 particles, reacted to release CO_2, and the rate limiting process was the diffusion of Li^+ across the $LiFeO_2$ product layer.

Effect of Particle Size

Increasing the particle size of the Mn_3O_4 was hypothesized to reduce the reaction rate for the direct causticizing reaction. A larger particle results in a longer diffusion path for the diffusing species, in order to reach complete conversion of the particle. The longer diffusion path decreases the rate at which the diffusing species can reach the reaction interface, slowing the reaction.

The Ginstling-Brounshtein model was derived for spherical reactants. In the model, the reaction rate constant, k_d, is proportional to $1/r^2$ as shown in Equation 18 on page 20. The proportionality is equivalent to $2DC_oV_M$. If the constants 2, C_o, and V_M are combined with the diffusivity frequency factor, the following equations result.

Equation 30

$$k_d = \frac{A_o e^{-E/RT}}{r^2}$$

Equation 31

$$A_o = 2C_oV_M A$$

Taking the natural logarithm of Equation 30 and letting $A_o e^{-E/RT}$ equal B yields the following.

Equation 32

$$\ln k = \ln B - 2\ln r$$

A plot of ln k versus ln r should yield a straight line with slope –2 for spherical particles. The exponential of the intercept should yield the proportionality, B. Figure 45, Figure 46, and Figure 47 are plots of ln k versus ln r using the volume, number, and Sauter mean

particle sizes, respectively. The small, medium, and large Mn_3O_4 particles with three initial molar ratios were used.

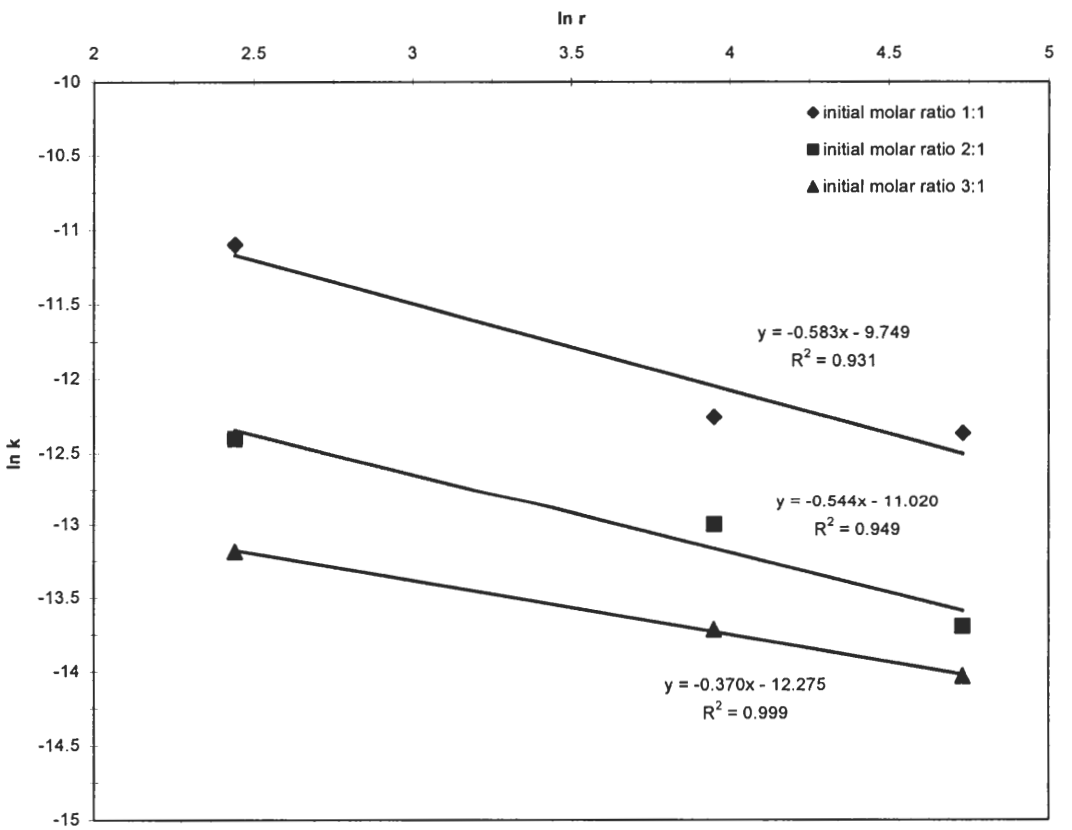

Figure 45 The effect of volume mean particle size on reaction rate. 23, 104, and 227μm Mn_3O_4.

Using the volume mean particle size results in slopes of –0.583±0.158, –0.544±0.126, and –0.370±0.012 for initial molar ratios of 1, 2, and 3 respectively. The average of these slopes is approximately –0.5. This indicates that the particle size dependence is not $1/r^2$ but instead $1/r^{0.5}$.

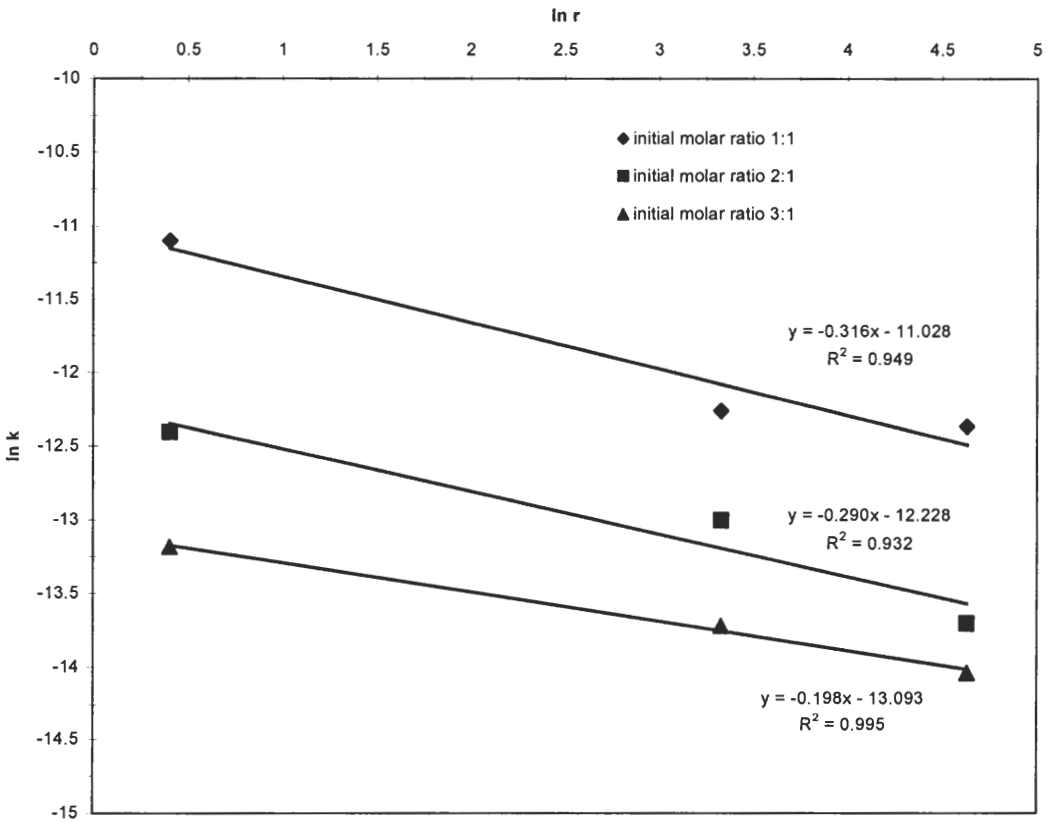

Figure 46 The effect of number mean particle size on reaction rate. 3, 56, and 206μm Mn_3O_4.

Using the number mean particle size results in slopes of –0.316±0.074, –0.290±0.078, and –0.198±0.014 for initial molar ratios of 1, 2, and 3 respectively. The average of these slopes is approximately –0.27. This indicates that the particle size dependence is not $1/r^2$ but instead $1/r^{0.27}$.

Use of the Sauter mean diameter yielded results between those obtained with the volume and number mean particle sizes. The average slope was approximately -0.42.

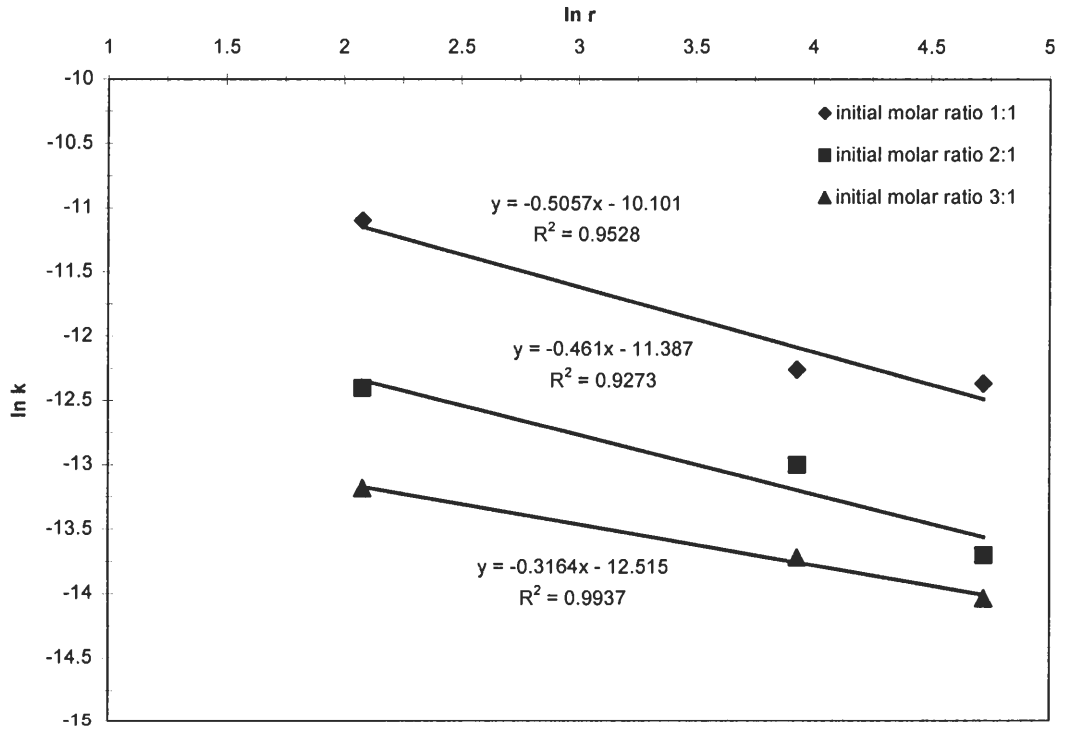

Figure 47 The effect of the Sauter mean particle size on reaction rate. 16, 102, and 225μm Mn_3O_4.

A strong conclusion on the effect of the particle size on reaction rate can not be inferred from these results. The deviation from the theoretical $1/r^2$ dependence is not entirely surprising. The SEM images showed that the starting materials are very rough approximations for spheres. The particle sizes that were reported are based on equivalent spherical diameters. This was used as the characteristic length that should have the $1/r^2$ dependence. The deviation suggests that a different, smaller length scale for diffusion is more appropriate. This could be attributed to the length scale of the individual crystals that make up the overall particle size. In addition, the small Mn_3O_4 was mechanically treated with the mortar and pestle to produce particles with different characteristics than the medium and large fractions. This mechanical treatment was likely to change the

reactivity of the particles by introducing defects in the surface and structure.[44] These defects lead to preferential sites of reaction. If the defect extends into the crystal, the diffusional resistance can be decreased by up to two orders of magnitude[26], also contributing to the deviation. These problems lead to the qualitative conclusion that an increase in Mn_3O_4 particle size results in a decrease in the reaction rate constant.

As the particle size distribution becomes more homogeneous, the number mean particle size approaches the volume mean. The Sauter mean was also found to be very similar to the volume mean. Therefore, the volume mean particle size distribution was used to estimate the proportionality, B. Differences in the value for B, with different initial molar ratios, should indicate the dependence of the diffusivity frequency factor, A, on the initial molar ratio.

From Figure 45, intercepts of -9.75 ± 0.61, -11.02 ± 0.48, and -12.28 ± 0.05, corresponding to initial molar ratios of 1, 2, and 3, were used to determine the proportionality, *B*. Figure 48 shows that *B* has a power law dependence on the initial molar ratio of Mn_3O_4:Na_2CO_3. This implies that the diffusivity frequency factor, *A*, will have a power law dependence on the initial molar ratio. This will be investigated further in the next section.

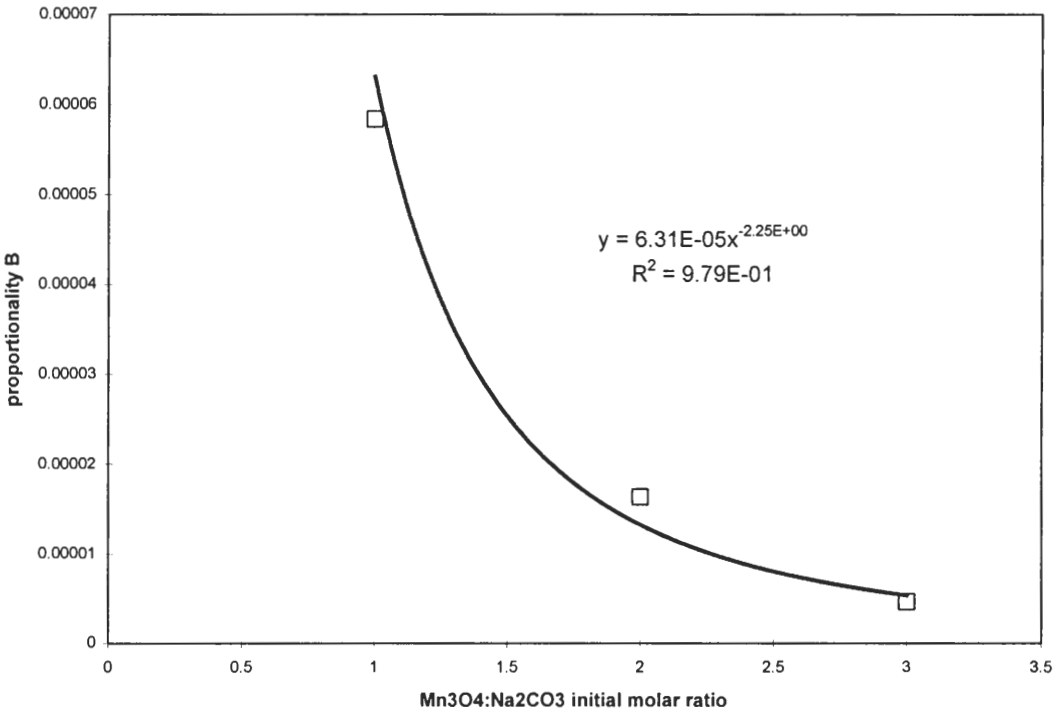

Figure 48 Effect of initial molar ratio on proportionality B. The diffusivity frequency factor, A, is proportional to B.

Effect of Initial Molar Ratio of Reactants

Traditional kinetic models for heterogeneous reactions are written with a concentration dependence. For solid-solid reactions, it is difficult to define the concentration at the reaction interface in the traditional sense. If two pure solids are placed in contact with each other, a mol/cm^3 definition makes no sense. A bulk concentration can be defined, but because of the nature of solids, it needs to be described in a different way.

In gas-solid reactions the surface area of the solid reactant is sometimes used to characterize the availability of reactants. In this situation, the surface of the solid is

accessible to the fluid, and contact with up to 100% of the available surface area is possible. The situation is different for solid reactants. Loosely poured spherical particles will contact each other at an estimated 10^{-6}-10^{-10} of the total surface area available.[44] Differences in particle density, size, internal surface area, and packing density affect the contact surfaces and make it difficult to formulate a theoretical description of reaction rates based on surface area for solid-solid reactions. No theoretical models were found in the literature that described the change in reaction rate associated with varying the initial concentration of reactants in a powdered mixture.

One way to address concentration effects for solid-solid reactions is to state the concentration in terms of the initial molar ratio of reactants. By increasing the number of moles of one reactant relative to the other, the surface area of the reactant is essentially changing. Doubling the number of moles of one reactant will double its surface area too. The species that was doubled will have fewer contacts with the other species because of the same species contacts that will occur.

For the Na_2CO_3 and Mn_3O_4 reaction, Na_2CO_3 is the more mobile substance because of its lower melting point. It is therefore considered the diffusing species. The Mn_3O_4 is the particle being covered. The product layer becomes the barrier that the Na_2CO_3 has to diffuse through.

The overall goal of direct causticizing is to convert Na_2CO_3 to NaOH. High conversions of Na_2CO_3 are desired. Because of the 1:1 stoichiometry of the reaction,

areas of practical interest to study include stoichiometric amounts of reactants, or an excess of Mn_3O_4. With an excess of Na_2CO_3, complete conversion of the component would not occur. However, some experiments were completed with excess Na_2CO_3 to investigate the phenomena.

Figure 49 and Figure 50 show the effect of the initial molar ratio of reactants on the kinetic rate constant for the case where there is a stoichiometric excess of Na_2CO_3. The graph in Figure 49 is for 827 °C with Mn_3O_4 powder and Na_2CO_3 powder. Figure 50 is for similar reactants at 717 °C. Values for the initial molar ratio of reactants below 1 indicate that Mn_3O_4 is the limiting reactant. Both temperatures exhibited a similar trend towards an increase in the reaction rate constant with an increase in the amount of excess Na_2CO_3. A power law equation was selected to represent the dependence of the initial molar ratio on reaction rate.

Having an excess amount of Na_2CO_3 in the reaction mixture results in the Mn_3O_4 particles initially having more contacts with Na_2CO_3. This leads to more nucleation sites and quicker initial coverage of the Mn_3O_4 surface. It is proposed that the excess Na_2CO_3 also gives a thicker and more uniform coating on the Mn_3O_4 particles. This more uniform surface coverage in essence is a stronger driving force for diffusion of Na_2CO_3 into the product layer, toward the reaction interface. The result is an increase in the diffusion controlled reaction rate with an increase in initial amount of Na_2CO_3.

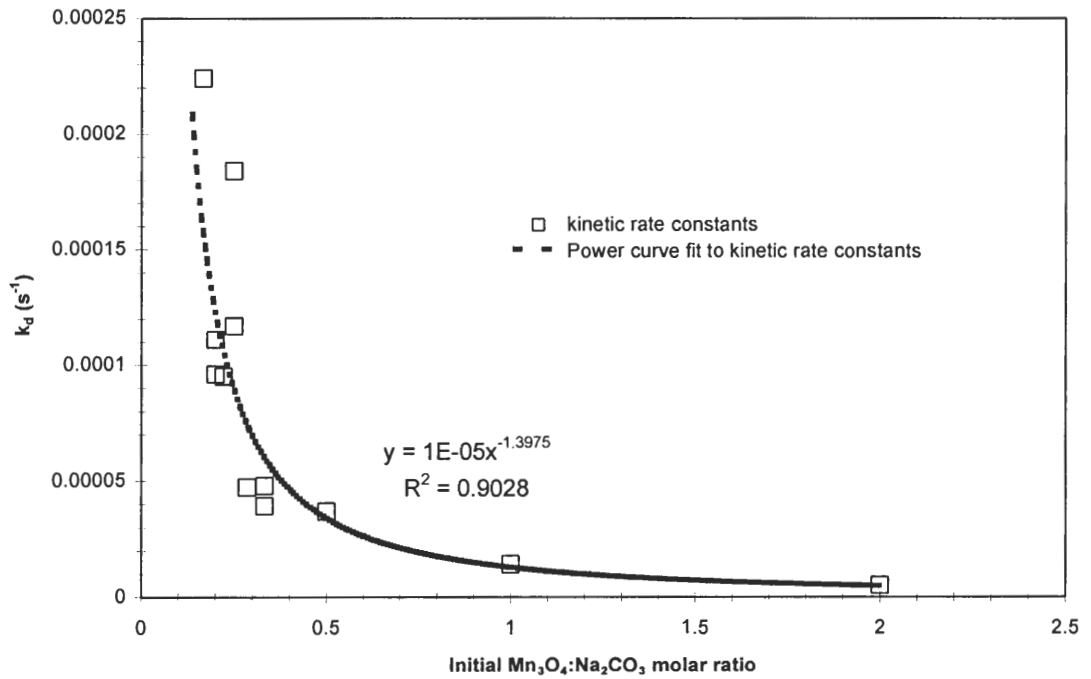

Figure 49 The kinetic rate constant versus the initial molar ratio of reactants. 827 °C. Mn_3O_4 and Na_2CO_3 powders.

A series of experiments was conducted to investigate the effects of stoichiometric excesses of Mn_3O_4 in the reaction mixture. The results are presented in Figure 51 for three particle sizes at 827 °C and also for the small Mn_3O_4 particles at 740 °C. In these experiments, the Na_2CO_3 was the limiting reactant, being entirely consumed. A trend similar to the case of excess Na_2CO_3 developed. When more Na_2CO_3 was initially present in the reaction mixture, the kinetic rate constant was higher. These data also were well described by an empirical fit to the power law.

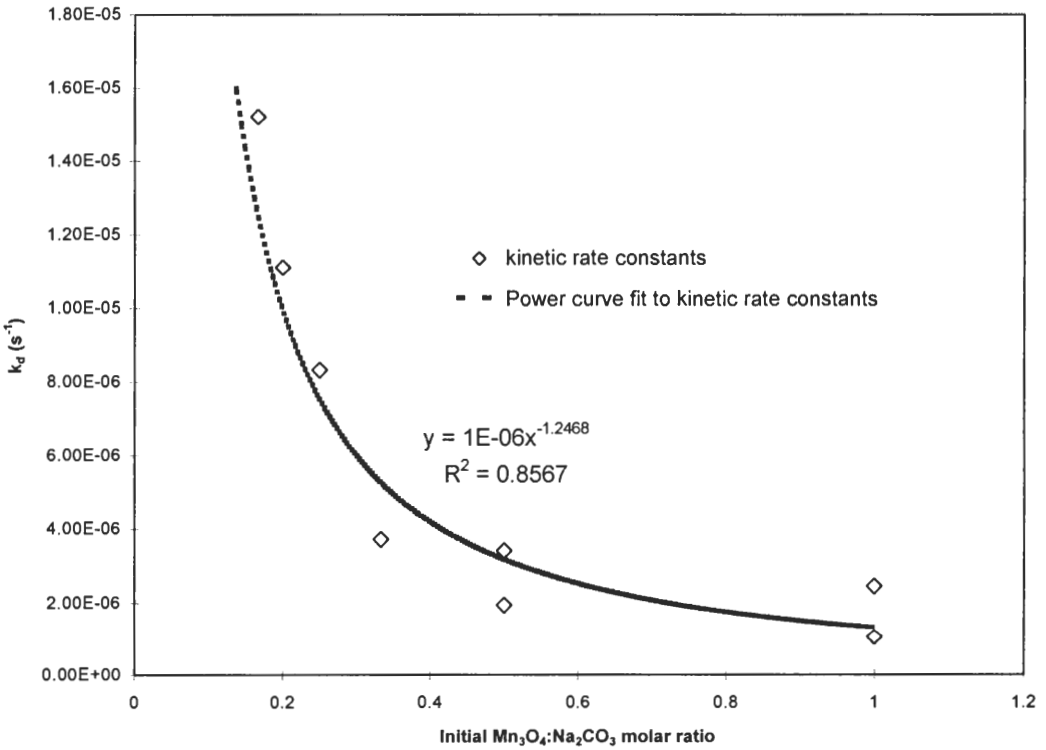

Figure 50 The kinetic rate constant versus the initial molar ratio of reactants. 717 °C. Mn_3O_4 and Na_2CO_3 powders.

The change in the reaction rate constant with different initial molar ratios of reactants suggests that the diffusivity frequency factor has a power law dependence on the initial molar ratio.

Equation 33

$$A = \varphi\left(\frac{Mn_3O_4}{Na_2CO_3}\right)^{\varepsilon}$$

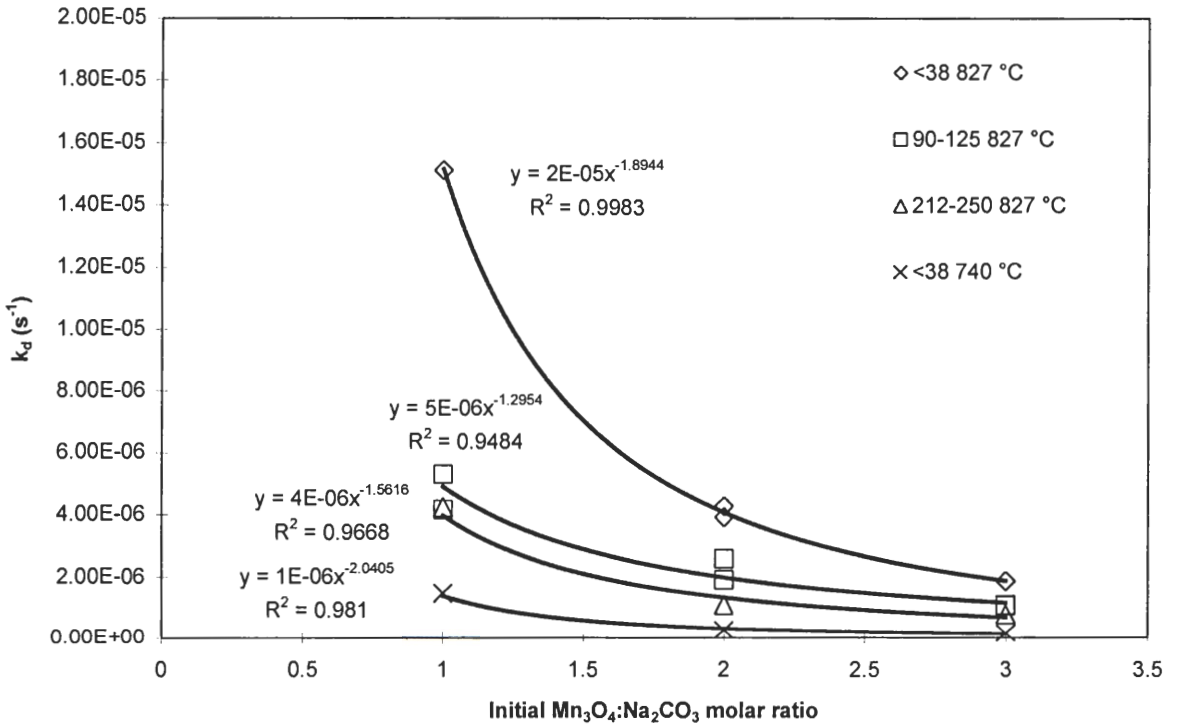

Figure 51 The kinetic rate constant versus the initial molar ratio of reactants. 740 and 827 °C. Various Mn_3O_4 particle sizes and Na_2CO_3 powder.

The power, ε, and pre-power factor, φ, are dependent on the particles used in the reactions. Different particle sizes, pre-treatments, and morphologies appear to change their values.

The Ginstling-Brounshtein kinetic rate constant for the reaction between Mn_3O_4 and Na_2CO_3 can be summarized with the following expression.

Equation 34

$$k_d = \frac{2\varphi\left(\frac{Mn_3O_4}{Na_2CO_3}\right)^{\varepsilon} e^{-E/RT} C_o V_m}{r^{0.5}}$$

E is 206 kJ/mol between 650 and 850 °C and 174 kJ/mol between 850 and 950 °C. φ and ε are functions of the specific reactants used.

Something that is not immediately obvious from Figure 51 is how an excess amount of Mn_3O_4 actually speeds up the overall conversion of Na_2CO_3. An excess amount of Mn_3O_4 in the reaction mixture results in product layers that do not extend completely into the Mn_3O_4 particles at complete conversions of Na_2CO_3. From geometry and stoichiometry it is calculated that an increase in the initial molar ratio of Mn_3O_4 to Na_2CO_3 from 1:1 to 3:1 results in a theoretical decrease in the product layer thickness of 87%. This is shown in Table 2, with the theoretical depth of reactant layer penetration calculated from Equation 16 on page 20. This thin product layer contributes to shorter diffusion paths for the Na_2CO_3. This shorter diffusion path leads to quicker conversions of Na_2CO_3 as shown in Table 3. However, because the Mn_3O_4 is in excess, its rate of fractional conversion is much slower, resulting in smaller kinetic rate constants with the increase in initial amounts of Mn_3O_4.

Table 2 Theoretical depth of reactant layer penetration into spherical Mn_3O_4 particles as function of the initial molar ratio.

Mn_3O_4:Na_2CO_3 initial molar ratio	*Conversion of Mn_3O_4 at 100% conversion of Na_2CO_3*	*Depth of reactant layer penetration as a % of particle radius*
1:1	100%	100%
2:1	50%	20.6%
3:1	33%	12.6%

Table 3 Comparison of times to reach 30% conversion for different initial molar ratios. 827 °C, medium Mn_3O_4, powdered Na_2CO_3.

Mn_3O_4:Na_2CO_3 initial molar ratio	*Time to 30% Conversion Mn_3O_4 (s)*	*Time to 30% Conversion Na_2CO_3 (s)*
1:1	7680	7680
2:1	13890	5520
3:1	18570	4260

OVERALL PROCESS EFFICIENCY

A secondary objective of this work was to determine an overall process efficiency for Mn_3O_4 based direct causticizing. In order to determine the process efficiencies, a sodium mass balance was conducted on the combined direct causticizing and hydrolysis steps. A mass balance on the manganese was also conducted. Separate efficiencies for the direct causticizing and hydrolysis steps were determined, in addition to an overall efficiency.

The hydrolysis step was combined with titrations, gravimetry, SEM, and XRD analysis to determine the chemical species involved in each step, and the overall efficiency of the process. A schematic of the overall process analysis used to close the mass balance is shown in Figure 52.

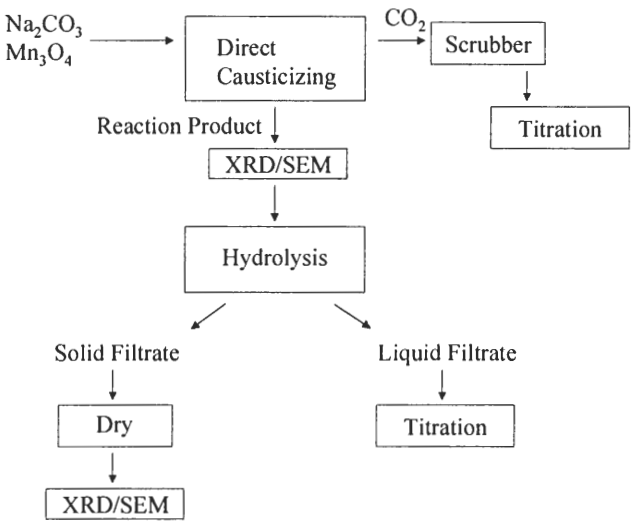

Figure 52 Flow chart for product identification and mass balance.

During the direct causticizing reaction, the product gas was continuously analyzed for the CO_2 content. The product gas was then sent to a gas-liquid scrubber filled with de-ionized water. Following the reaction, the scrubber solution was titrated with HCL to determine the sodium content.

The solid reaction product was weighed following the reaction. The solid product was observed with the scanning electron microscope to qualify the surface morphology of the reaction product. Some of the product was also analyzed with X-ray diffraction to determine which species were created during direct causticizing.

It was not the goal of this research to study the kinetics of the hydrolysis reaction. Therefore, hydrolysis was done under conditions to ensure essentially complete conversion. Zou found that the hydrolysis reaction for the TiO_2 system reached

equilibrium after 90 minutes.[19] For this work, the solid product was dissolved in water and hydrolyzed at 90 °C for five hours. Following hydrolysis, the slurry was filtered and washed. The filtrate was analyzed for NaOH and Na_2CO_3. The solid product was dried, weighed, and then analyzed with XRD and SEM. The weight loss during hydrolysis was used to confirm the reaction mechanism.

The efficiency of the direct causticizing reaction was represented by the Na_2CO_3 conversion as defined in Equation 25 on page 43. This conversion was based on the CO_2 release as a function of the total Na_2CO_3 used in the reaction. The direct causticizing efficiency is presented below.

Equation 35

$$\alpha_{Na_2CO_3} = Eff_{dc}$$

The hydrolysis efficiency, Eff_h, is a measure of the conversion of the direct causticizing reaction product, $NaMnO_2$, into NaOH during the hydrolysis step.

Equation 36

$$\frac{mol\ NaOH_{out}}{mol\ NaMnO_{2\,in}} = Eff_h$$

The number of moles of $NaMnO_2$ for the hydrolysis step was calculated from the Na_2CO_3 conversion of the direct causticizing reaction, assuming that 1 mole of converted Na_2CO_3 produced 2 moles of $NaMnO_2$.

The aqueous filtrate from the hydrolysis step contained NaOH and Na_2CO_3. The overall efficiency was defined in a manner similar to that used for CaO based recovery cycles. With the CaO based recovery system, the causticity, also known as the causticizing efficiency, is an indication of the quality of the pulping liquor leaving the chemical recovery stage. It is based on the conversion of Na_2CO_3 into NaOH. For this work, the overall process efficiency, Eff_o, is defined in a similar manner.

Equation 37

$$\frac{mol\ NaOH}{mol\ NaOH + 2 \times mol\ Na_2CO_3} \times 100 = Eff_o$$

The moles of NaOH and Na_2CO_3 were determined in an aliquot of the filtrate to calculate the overall process efficiency. This is different than the traditional definition of causticity that uses g/L concentrations as equivalents of Na_2O. However, the result is the same.

The amount of make-up chemicals required for miscellaneous losses is a concern in chemical recovery. The sodium and manganese recovery rates were also determined. A mass balance on the total sodium into the process, as Na_2CO_3, and the amount of sodium recovered in the filtrate, as Na_2CO_3 and NaOH, was constructed. It was termed the Total Sodium Recovery and defined as follows.

Equation 38

$$\frac{mol\ Na\ recovered\ in\ filtrate}{mol\ Na\ into\ direct\ causticizing\ reaction\ as\ Na_2CO_3} \times 100 = Total\ Sodium\ Recovery\ (\%)$$

A similar definition was constructed for the manganese, as Mn_3O_4. It is based on the total Mn_3O_4 into the system and the amount of Mn_3O_4 recovered as solid from the hydrolysis step. It is assumed that the solid product is entirely Mn_3O_4.

Equation 39

$$\frac{weight\ of\ solid\ material\ from\ hydrolysis \div MW_{Mn_3O_4}}{mol\ of\ Mn_3O_4\ into\ direct\ causticizing\ reaction} \times 100 = Total\ Manganese\ Recovery\ (\%)$$

The scrubber solution from the direct causticizing reaction was analyzed for sodium species. No significant amounts of sodium were found, indicating that sodium did not leave in the gas phase.

The direct causticizing reaction product was analyzed using XRD. The analysis was not quantitative for determining the materials present. Figure 53 was obtained from a sample that had a large excess of Mn_3O_4 in the reaction mixture. The unreacted Mn_3O_4 is present in the XRD spectrum. In Figure 54, the reaction was limited to 87% conversion of Na_2CO_3 and the excess carbonate is present in the spectrum.

The primary reaction product was identified to be $NaMnO_2$. It was present for all temperatures and initial molar ratios. For reactions with an initial molar ratio of 1:1, MnO was also identified in the reaction product when the reaction was allowed to go to completion, as shown in Figure 55. Based on this, the following reaction sequence is proposed.

Equation 40

$$Na_2CO_3 + Mn_3O_4 \Rightarrow 2NaMnO_2 + MnO + CO_2$$

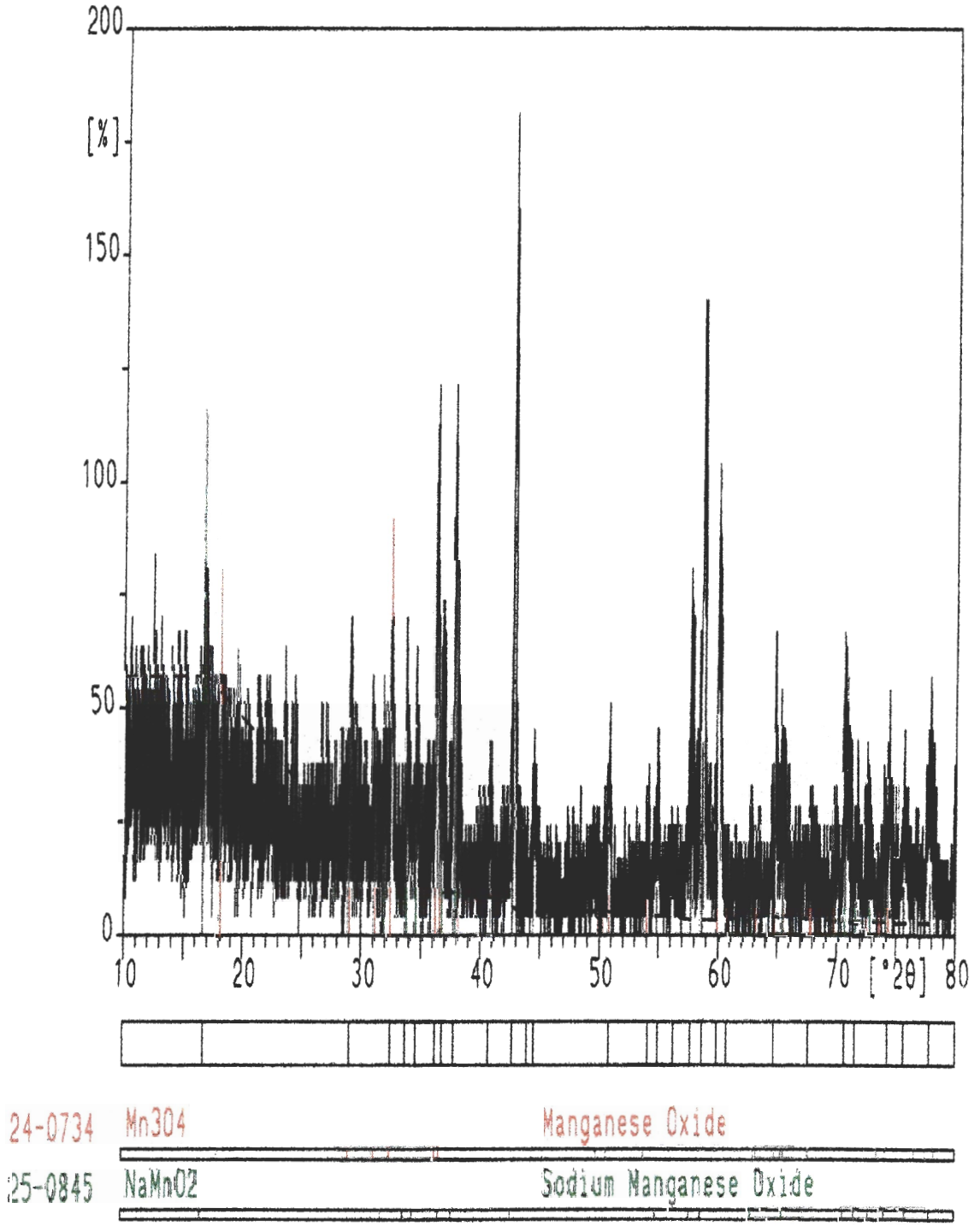

Figure 53 XRD scan of direct causticizing reaction product. 830 °C, large Mn_3O_4, Mn_3O_4:Na_2CO_3 3:1, 100% conversion.

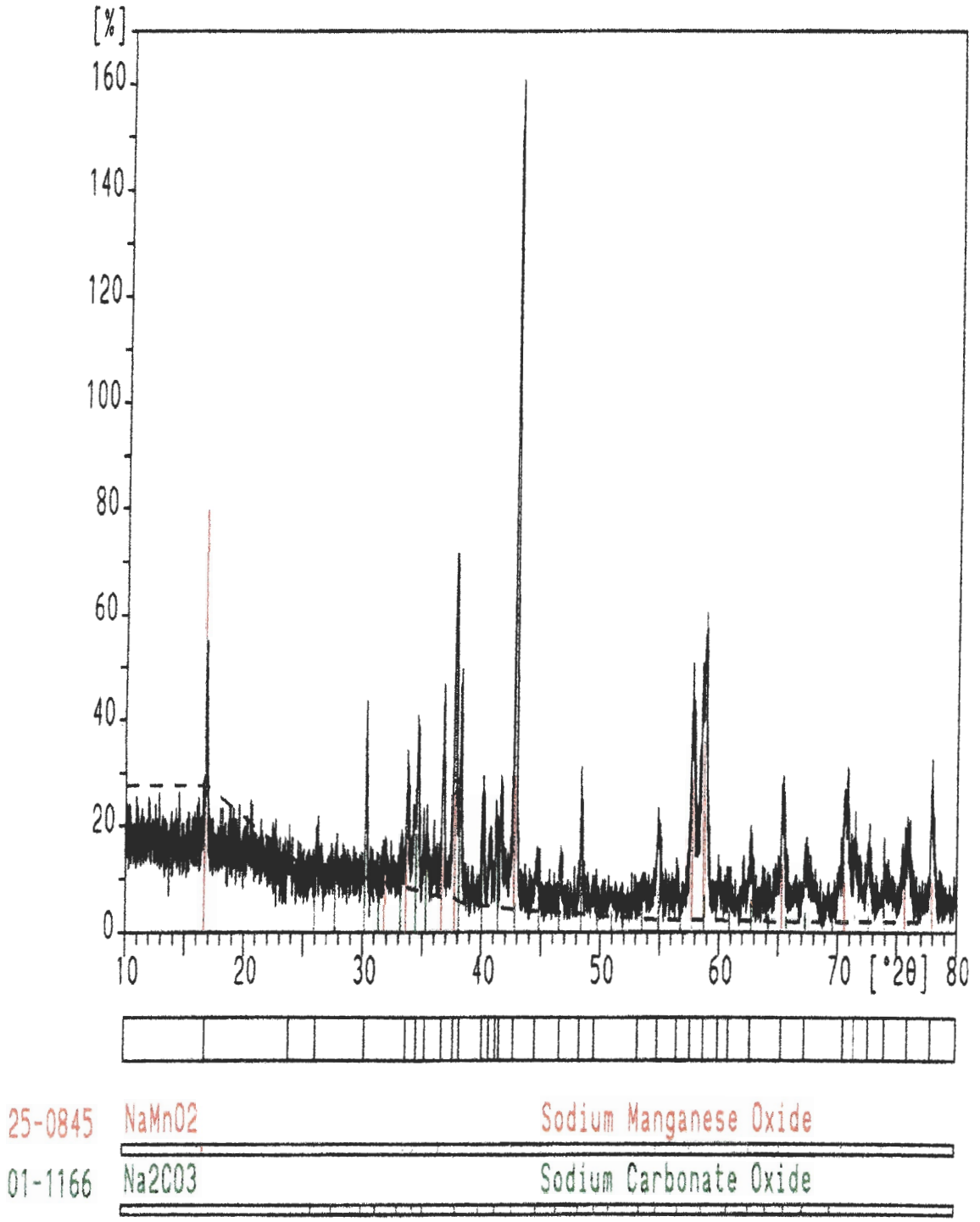

Figure 54 XRD scan of direct causticizing reaction product. 830 °C, large Mn_3O_4, Mn_3O_4:Na_2CO_3 1:1, 87% conversion.

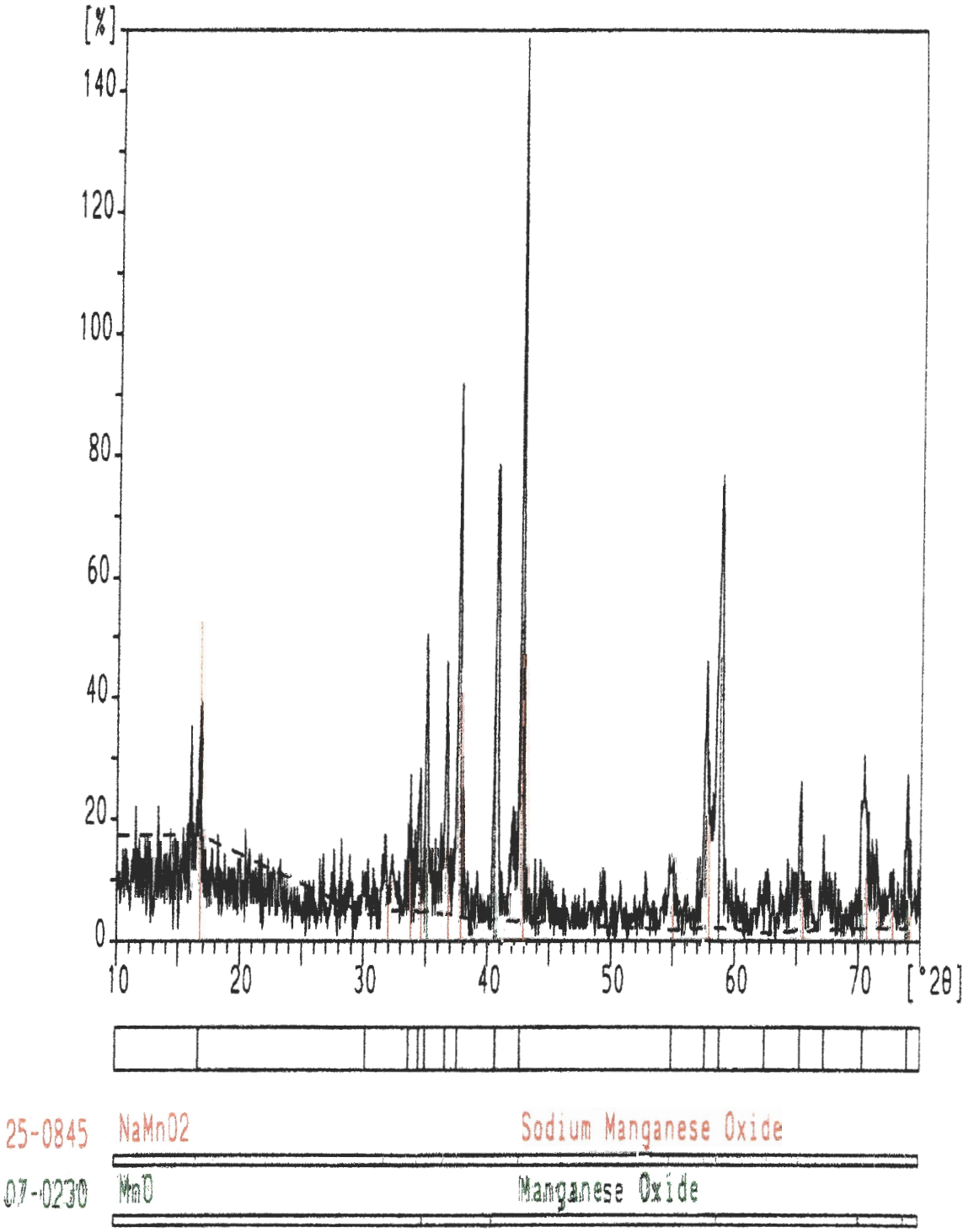

Figure 55 XRD scan of direct causticizing reaction product. 830 °C, small Mn_3O_4, Mn_3O_4:Na_2CO_3 1:1, 97% conversion.

Mn_3O_4 is a mixed oxidation state compound, comprised of Mn^{+2} and Mn^{+3} manganese. It can be considered Mn_2O_3 + MnO. The Mn^{+3} manganese appears to be more reactive than the Mn^{+2}, resulting in the formation of $NaMnO_2$. It is possible for MnO to oxidize to Mn_3O_4 through the following mechanism when exposed to air.

Equation 41

$$6MnO + O_2 \Rightarrow 2Mn_3O_4$$

It was not clear if this oxidation takes place with the reaction product during the XRD analysis. The MnO peaks were not present in all analyses. This could be attributed to the presence of unreacted Mn_3O_4 or Na_2CO_3 masking the MnO. The stability of the MnO in the reaction product at this point was unknown. It was hypothesized to be a separate compound from the $NaMnO_2$, or possibly stabilized and complexed with it to form a mixed solid of $2NaMnO_2 \cdot MnO$.

SEM images of the reaction products show that the Mn_3O_4 particles undergo a morphological change during the reaction. The influence of the reaction temperature, above or below the melting point of Na_2CO_3, had an effect on the product morphology. Figure 56 and Figure 57 show the reaction product for the solid-solid reaction with two magnifications, 50x and 250x. The reaction went to 87% conversion at 830 °C with large Mn_3O_4 and a Mn_3O_4:Na_2CO_3 initial ratio of 1:1. The rod-like structures that are present in Figure 23 and Figure 24 are not as sharp in the reaction product. The particles appeared to have become more spherical in shape and the surface is rougher. A qualitative examination of the micrographs shows that the overall particle diameter is

close to the original size, possibly with a slight increase in diameter. This indicates that the reaction product has a similar or slightly greater molar volume than Mn_3O_4.

Figure 58 and Figure 59 show the product for the reaction occurring above the melting point of Na_2CO_3. The reaction went to 99% conversion at 947 °C with large Mn_3O_4 and an initial molar ratio of 1:1. The particles have taken on a spherical appearance. The reaction product is comprised of fine needlelike structures. In both cases the particles did not appear to sinter together and form agglomerates.

The product layer diffusion controlled model suggests that a reaction interface will advance through the Mn_3O_4. Large particles were encased in epoxy and then ground to investigate the internal cross sectional view. Figure 60 is the cross sectional view of an unreacted large Mn_3O_4 particle. Figure 61 is an image that shows the reaction product at low conversion. The bright region around the edge was hypothesized to be $NaMnO_2$ with MnO. Figure 62 is a cross sectional image of the reaction product clearly showing the penetration of the reaction product into the Mn_3O_4 particle. Figure 63 shows a particle that appears to have undergone complete conversion into the reaction product.

The sample in Figure 62 was analyzed with energy dispersive x-ray spectroscopy (EDS) to identify elements in the two regions. The EDS spectrum in Figure 64 and Figure 65 have peaks for gold and palladium from the sputter coating. Manganese was also identified in both regions. Sodium was found in the hypothesized reaction product, but not in the unreacted core. This series of images suggests that the Na_2CO_3 does

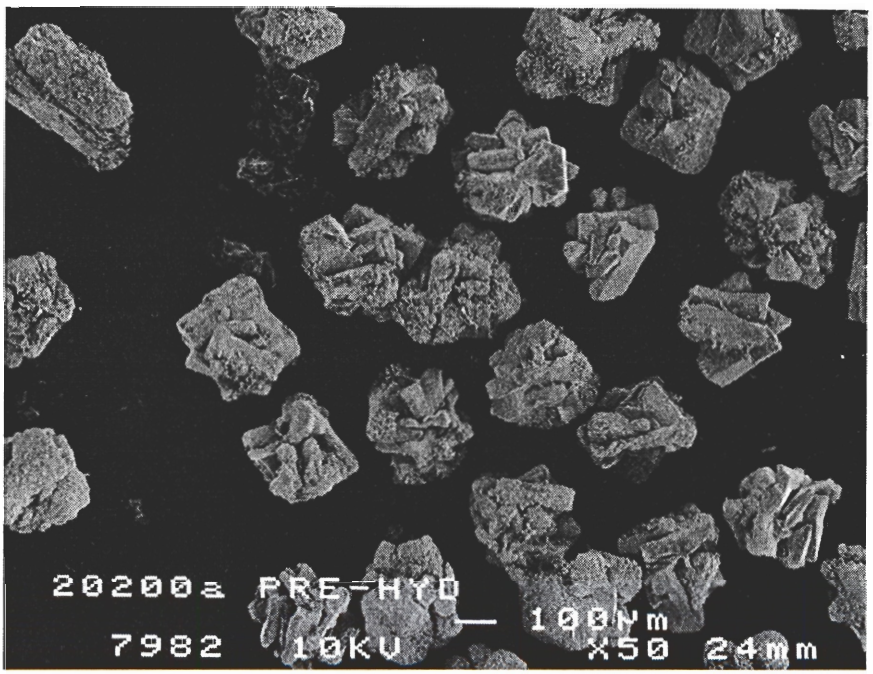

Figure 56 SEM image of direct causticizing product prior to hydrolysis. 50x magnification. 830 °C. large Mn_3O_4, powdered Na_2CO_3. Mn_3O_4:Na_2CO_3 1:1. Reacted until 87% conversion.

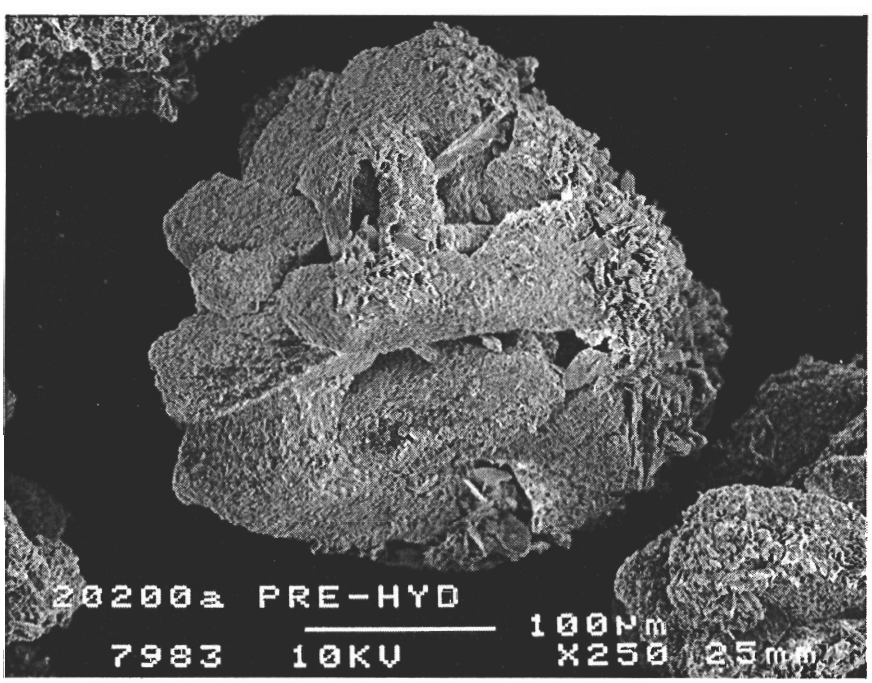

Figure 57 SEM image of direct causticizing product prior to hydrolysis. 250x magnification. 830 °C. large Mn_3O_4, powdered Na_2CO_3. Mn_3O_4:Na_2CO_3 1:1. Reacted until 87% conversion.

Figure 58 SEM image of direct causticizing product prior to hydrolysis. 50x magnification. 947 °C. large Mn_3O_4, powdered Na_2CO_3. Mn_3O_4:Na_2CO_3 1:1. Reacted until 99% conversion.

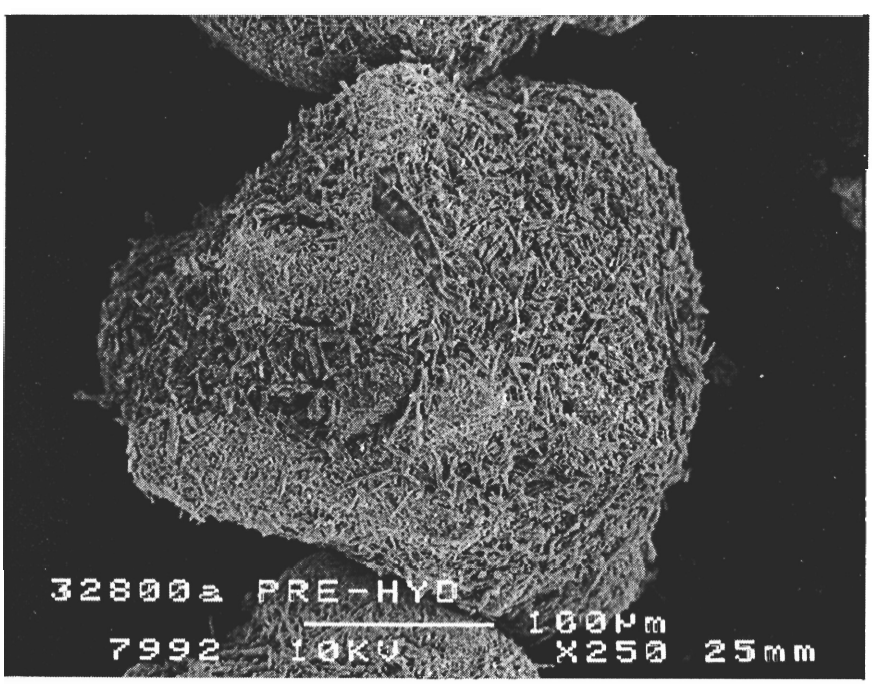

Figure 59 SEM image of direct causticizing product prior to hydrolysis. 250x magnification. 947 °C. large Mn_3O_4, powdered Na_2CO_3. Mn_3O_4:Na_2CO_3 1:1. Reacted until 99% conversion.

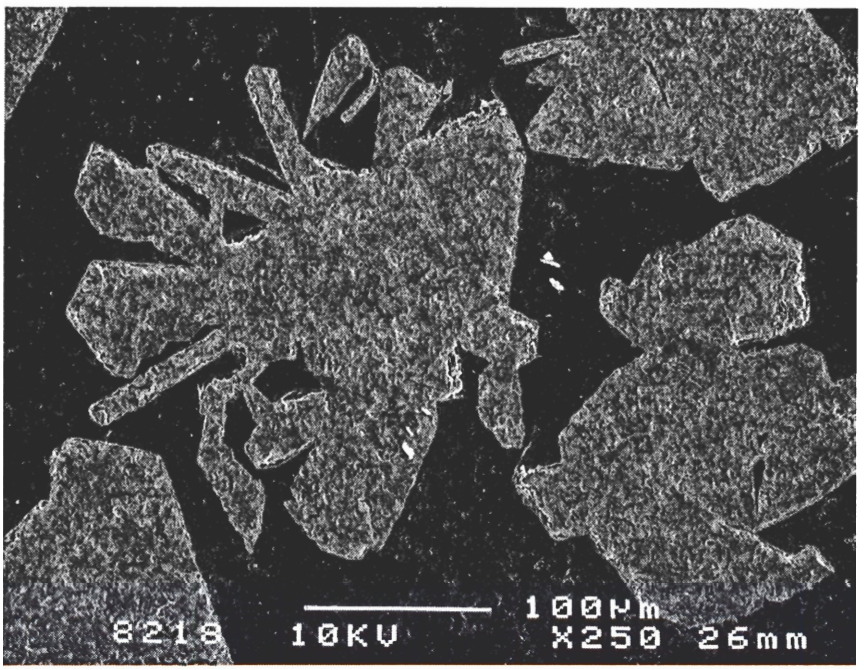

Figure 60 Cross sectional view of unreacted large Mn_3O_4.

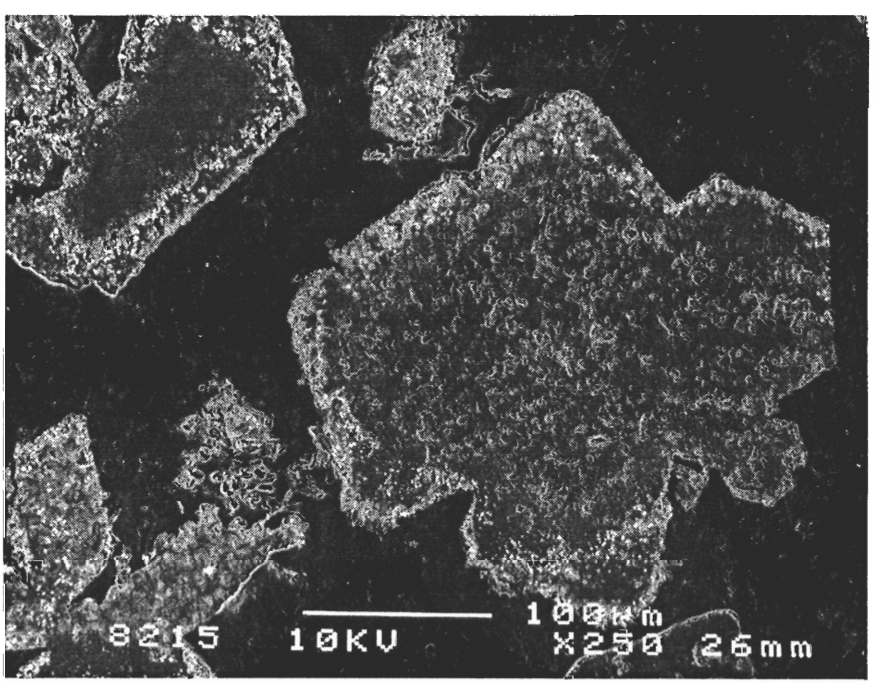

Figure 61 Cross sectional view of large Mn_3O_4 at the initiation of reaction.

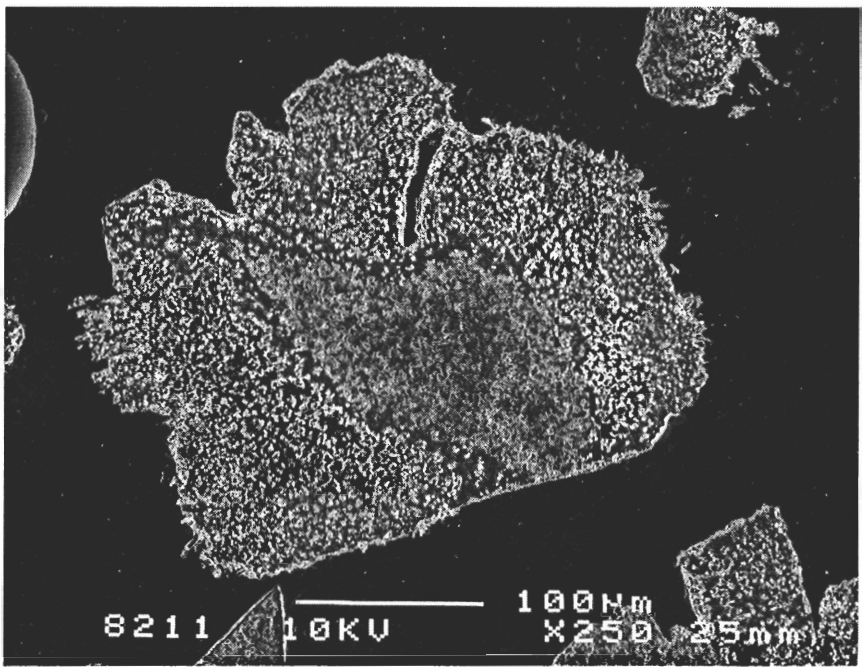

Figure 62 Cross sectional view of Large Mn_3O_4 showing the advancing reaction interface.

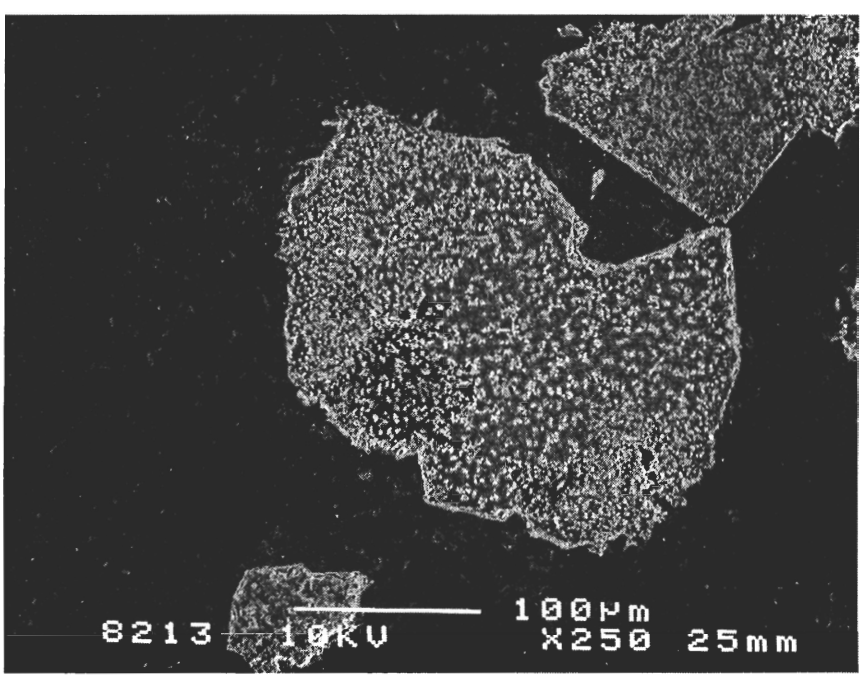

Figure 63 Cross sectional view of large Mn_3O_4 showing complete penetration of reaction product.

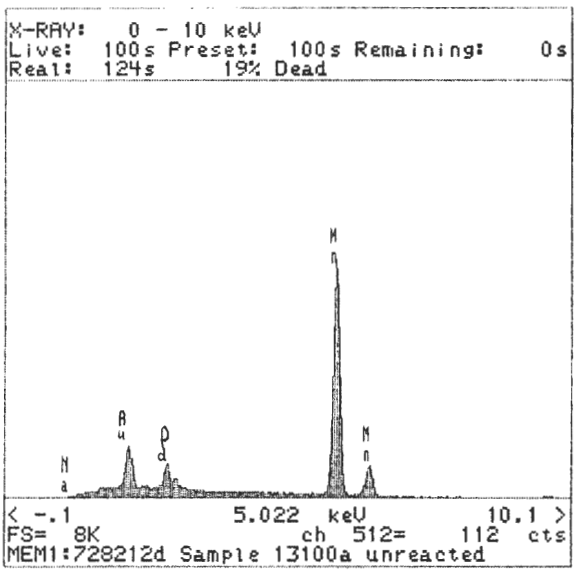

Figure 64 EDS spectrum of unreacted core sample in Figure 62. No sodium detected.

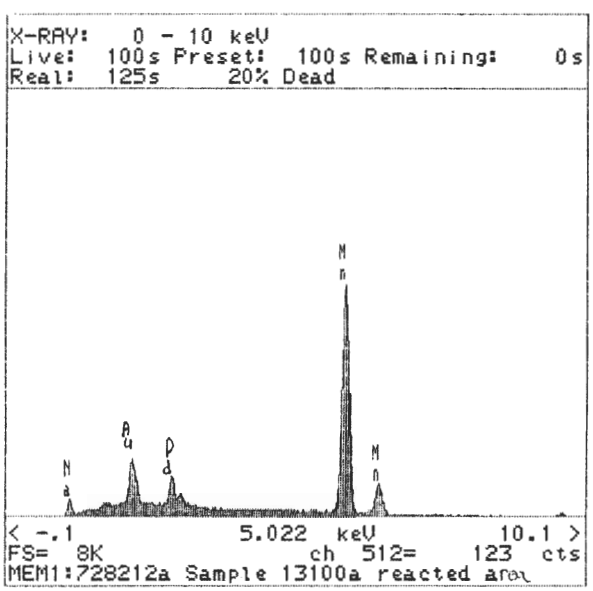

Figure 65 EDS spectrum of product layer in Figure 62. Sodium was detected.

diffuse through the reaction product to react at the $Mn_3O_4/NaMnO_2$-MnO interface.

The reaction product was hydrolyzed in a glass flask with Teflon stir bar. A nitrogen purge was used to preclude CO_2 from entering the solution. The hydrolysis reaction was done for 5 hours at 90 °C. Following the hydrolysis, the solids were filtered, washed, and dried in an atmospheric oven at 105 °C.

A reaction mechanism for hydrolysis was suggested by measuring the weight loss of the solid product during hydrolysis. The following mechanism was hypothesized to occur.

Equation 42 $$2NaMnO_2 + MnO + H_2O \Rightarrow 2NaOH + Mn_3O_4$$

The hypothesis was tested by hydrolyzing reaction products with three different initial molar ratios. For an initial molar ratio of 1:1, if the direct causticizing reaction was completed, Equation 42 would represent the hydrolysis step. If the initial molar ratio was changed, to double the amount of Mn_3O_4, and the reaction went to completion, the reaction product would contain 1 mole of Mn_3O_4 for every 2 moles of $NaMnO_2$. The hydrolysis reaction would then be modified to the following.

Equation 43 $$2NaMnO_2 + MnO + Mn_3O_4 + H_2O \Rightarrow 2NaOH + 2Mn_3O_4$$

Likewise, for an Mn_3O_4:Na_2CO_3 initial molar ratio of 3:1, the hydrolysis reaction could be represented by

Equation 44 $$2NaMnO_2 + MnO + 2Mn_3O_4 + H_2O \Rightarrow 2NaOH + 3Mn_3O_4 .$$

Based on complete hydrolysis of the product, the weight loss should correspond to 21.3, 11.9, and 8.3% respectively for the 1:1, 2:1, and 3:1 initial molar ratios. Table 4 shows that there was good agreement between the theoretical weight loss of the proposed mechanism and the experiments.

Table 4 Theoretical and experimental weight loss during hydrolysis and Mn_3O_4 recovery as functions of the Mn_3O_4:Na_2CO_3 initial molar ratio.

Mn_3O_4:Na_2CO_3 initial molar ratio	*Theoretical Weight Loss From Hydrolysis, %*	*Experimental Weight Loss, %*	*Total Manganese Recovery, %*
1:1	21.3	20.6	100.2
2:1	11.9	11.9	101.7
3:1	8.3	9.1	99.1

This mechanism suggests that the solid product is a mixture comprised of $NaMnO_2$ and MnO. The MnO does not oxidize to Mn_3O_4 during the transfer from the reactor to the hydrolysis step. Additionally, the experimentally determined Total Manganese Recovery is essentially 100%.

The dried hydrolysis samples were analyzed with XRD. The principal component in the samples was Mn_3O_4 as shown in Figure 66. The peak at the 2θ angle of 40.5 is attributed to trace amounts of MnO in the sample. This implies that the recycled product in a commercial application would be Mn_3O_4. The direct causticizing reaction has 1:1 stoichiometry, and the reaction product undergoes complete hydrolysis to return the

essentially pure Mn_3O_4. Manganese oxide based direct causticizing can then be summarized by the following two relationships.

Equation 45 $$Na_2CO_3 + Mn_3O_4 \Rightarrow 2NaMnO_2 + MnO + CO_2$$

Equation 46 $$2NaMnO_2 + MnO + H_2O \Rightarrow 2NaOH + Mn_3O_4$$

SEM images of the dried solid hydrolysis product, Mn_3O_4, show that the material changes significantly during direct causticizing and hydrolysis. Figure 67 and Figure 68 show the hydrolysis reaction product for large Mn_3O_4 reacted at 830 °C. From Figure 67 it is evident that a lot of fines were generated during hydrolysis. These fine particles may have been formed due to the action of the stir bar. The particle size appeared to be smaller than the initial starting material. Figure 68 shows that the particle surface has developed many cracks. The fines material also appears on the surface of the particle.

Figure 69 and Figure 70 show the post hydrolysis products from the reaction at 830 °C with medium Mn_3O_4 and an initial molar ratio of 1:1. Figure 69, at 250x magnification, also shows a large number of fines material. At the top of the image, several particles less than 90μm in diameter are visible. In Figure 70, a 1000x magnification of the fines material is shown. This is presumably Mn_3O_4, yet the structure is different from the starting material. The structure of the material has changed to a material with many cracks.

Figure 71 and Figure 72 show the hydrolysis product from the direct causticizing reaction with molten Na_2CO_3. The fines generation was present for this material also. Some of the needlelike structures characterizing the pre-hydrolysis material from the molten reaction are still present in Figure 72.

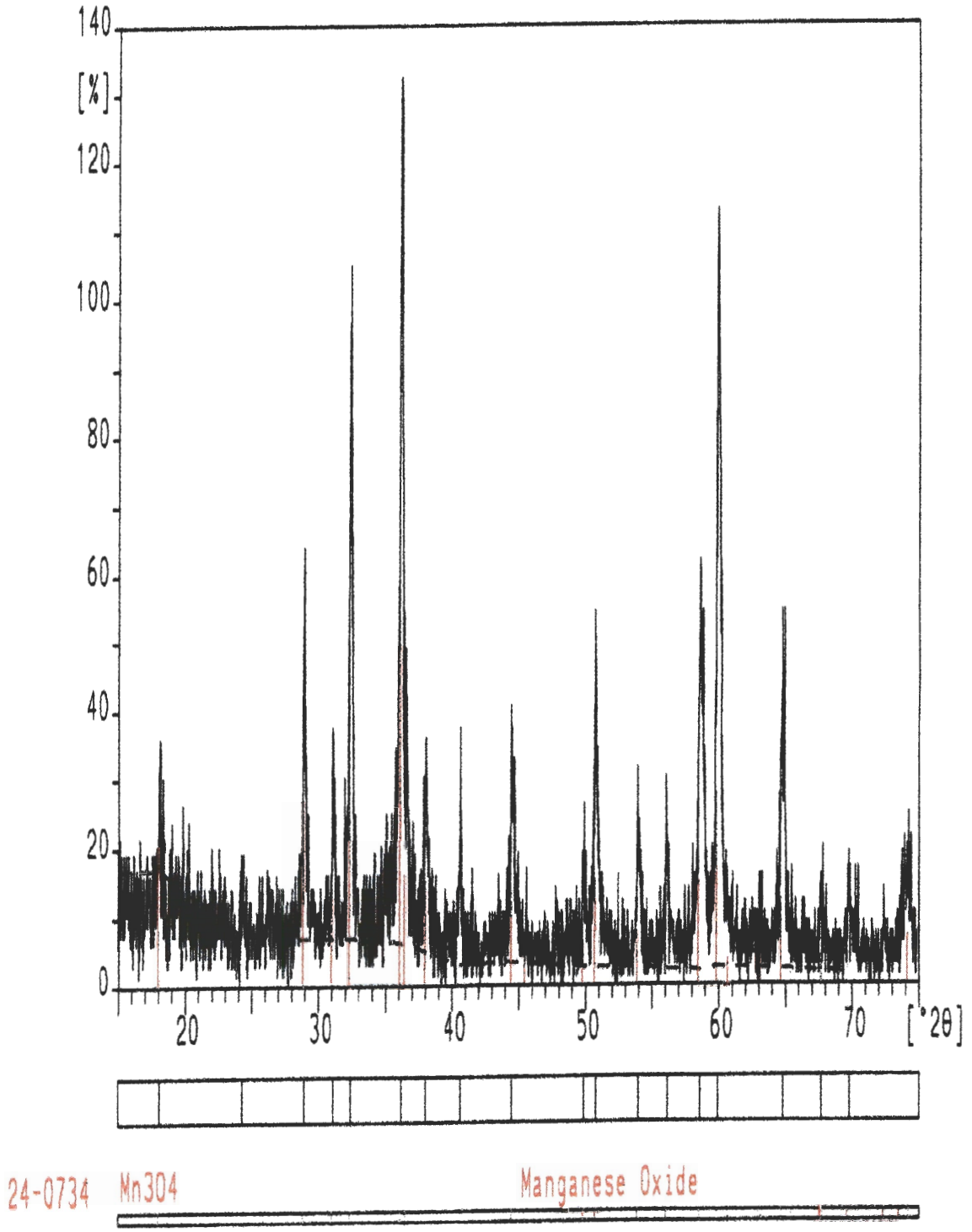

Figure 66 XRD scan of hydrolysis product. 830 °C, medium Mn_3O_4, Mn_3O_4:Na_2CO_3 1:1, 87% conversion.

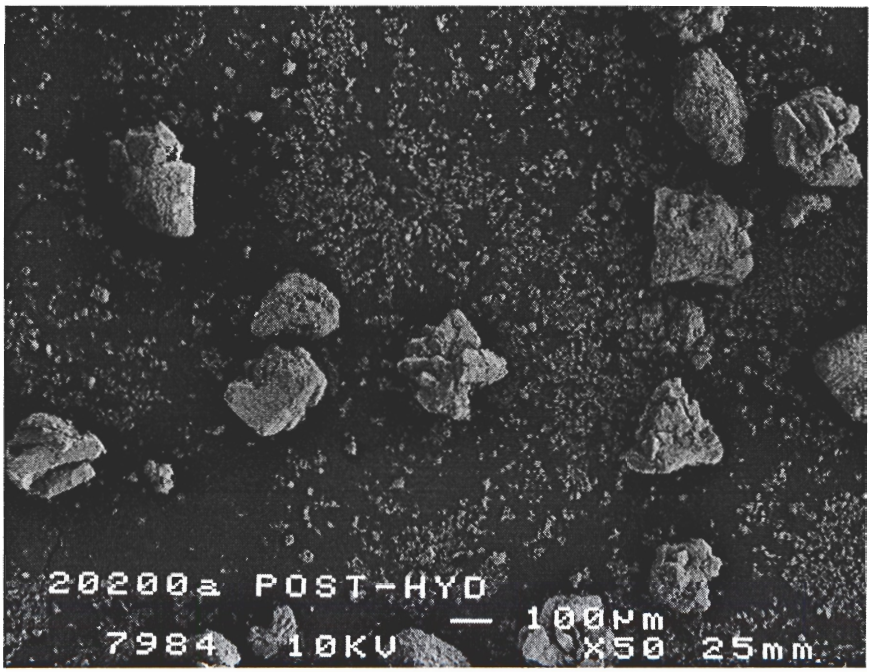

Figure 67 SEM image of direct causticizing product following hydrolysis. 50x magnification. 830 °C. large Mn_3O_4, powdered Na_2CO_3. Mn_3O_4:Na_2CO_3 1:1. Reacted until 87% conversion.

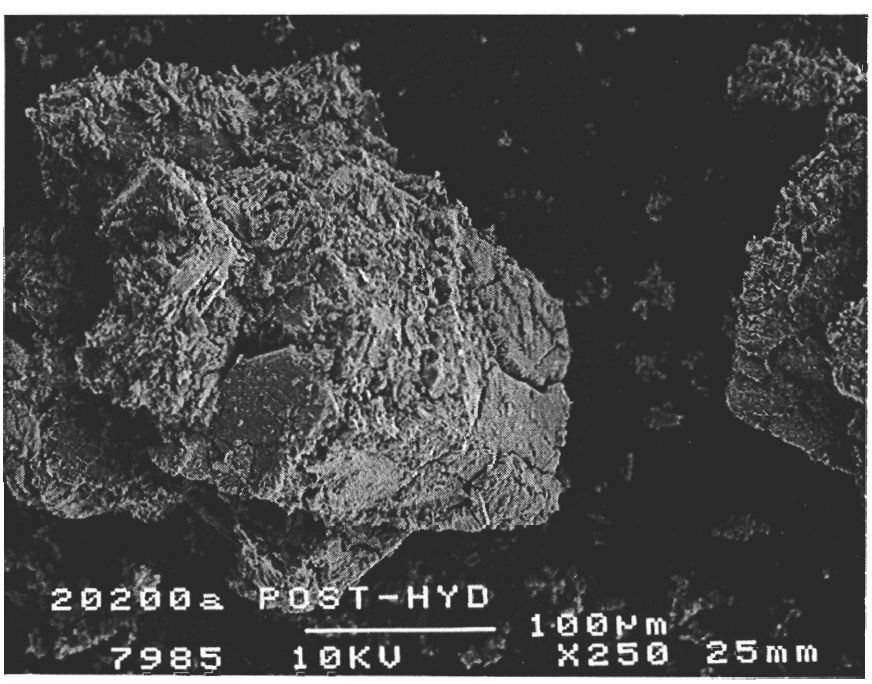

Figure 68 SEM image of direct causticizing product following hydrolysis. 250x magnification. 830 °C. large Mn_3O_4, powdered Na_2CO_3. Mn_3O_4:Na_2CO_3 1:1. Reacted until 87% conversion.

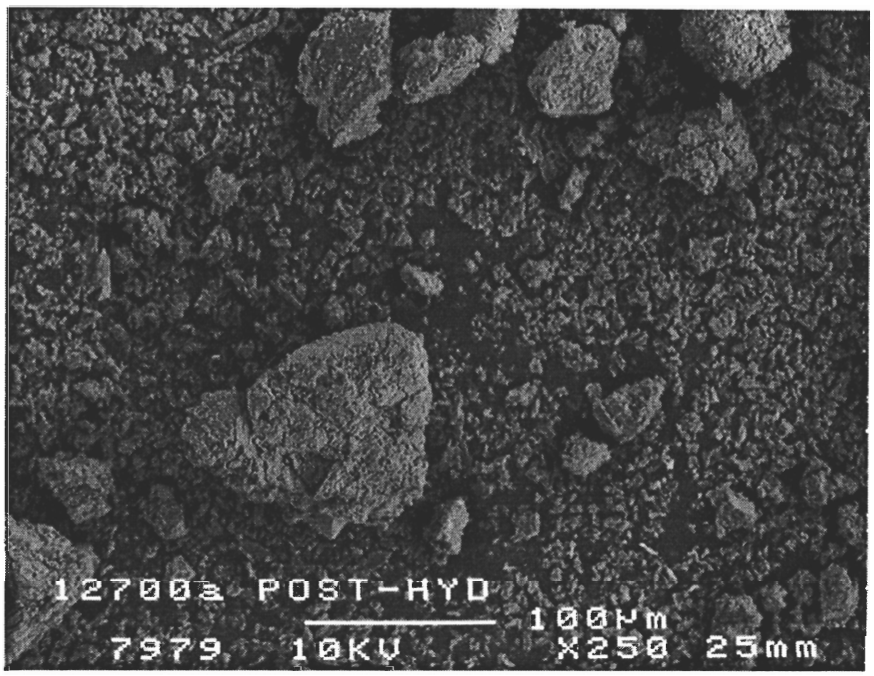

Figure 69 SEM image of direct causticizing product following hydrolysis. 250x magnification. 830 °C. medium Mn_3O_4, powdered Na_2CO_3. Mn_3O_4:Na_2CO_3 1:1. Reacted until 87% conversion.

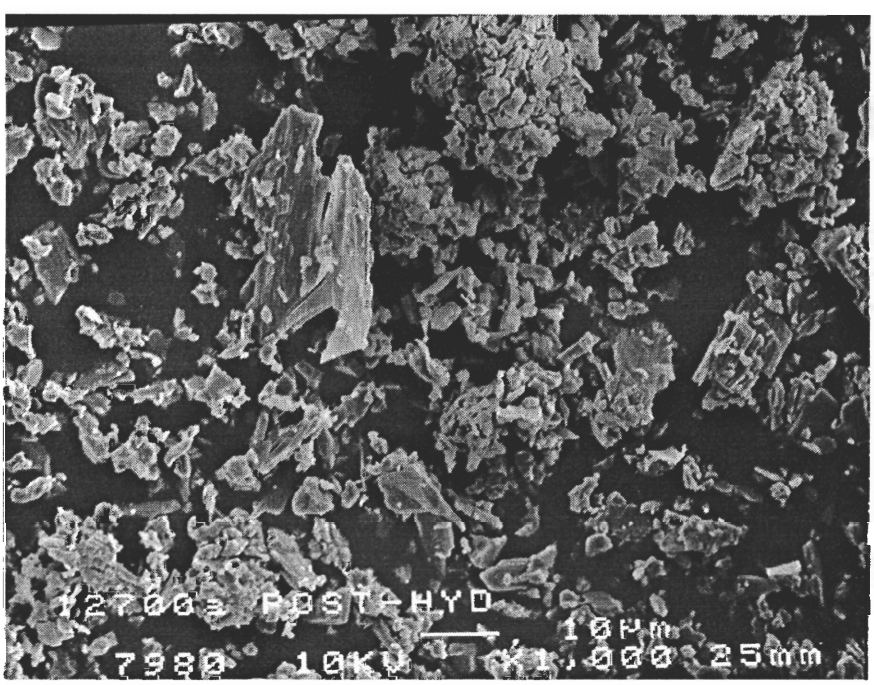

Figure 70 SEM image of direct causticizing product following hydrolysis. 1000x magnification. 830 °C. medium Mn_3O_4, powdered Na_2CO_3. Mn_3O_4:Na_2CO_3 1:1. Reacted until 87% conversion.

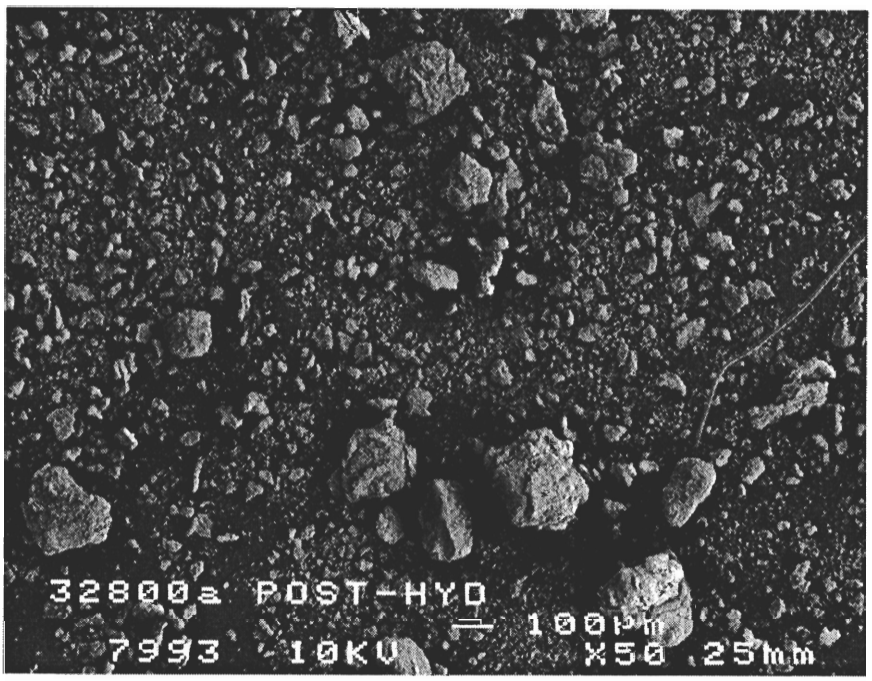

Figure 71 SEM image of direct causticizing product following hydrolysis. 50x magnification. 947 °C. Large Mn_3O_4, powdered Na_2CO_3. Mn_3O_4:Na_2CO_3 1:1. Reacted until 99% conversion.

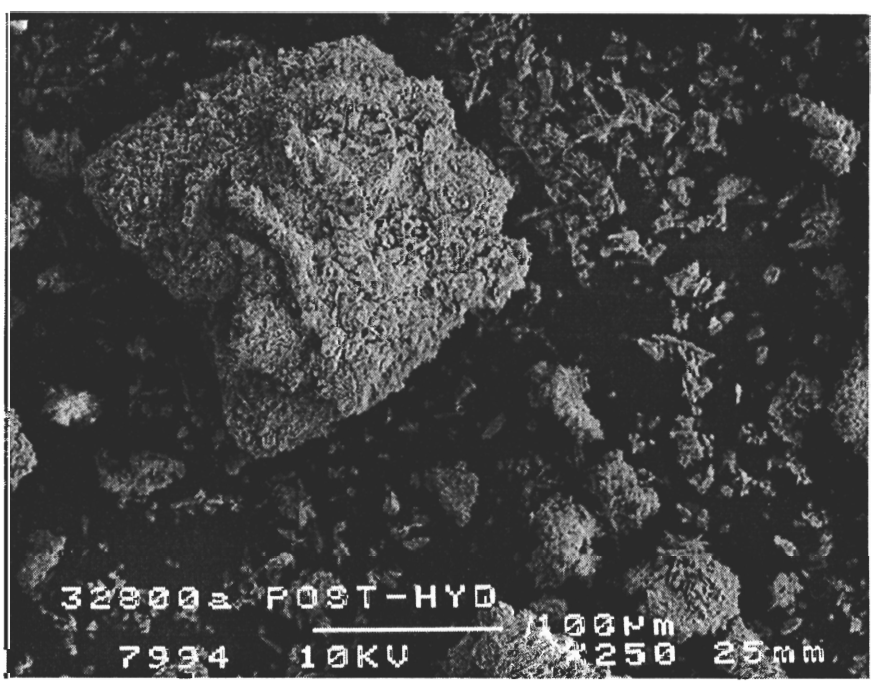

Figure 72 SEM image of direct causticizing product following hydrolysis. 250x magnification. 947 °C. Large Mn_3O_4, powdered Na_2CO_3. Mn_3O_4:Na_2CO_3 1:1. Reacted until 99% conversion.

The direct causticizing reaction and the hydrolysis step do not appear to be equilibrium limited. Values for the various efficiencies are presented in Table 5.

Table 5 Process efficiencies and material balance results for the overall direct causticizing process.

Temp (°C)	*Initial Molar Ratio*	*Mn_3O_4 Particle Size*	*Eff_{DC} (%) $\frac{CO_{2out}}{Na_2CO_{3in}}$*	*Eff_H (%) $\frac{NaOH_{out}}{NaMnO_{2in}}$*	*Eff_O (%) $\frac{NaOH}{NaOH+Na_2CO_3}$*	*Total Sodium Recovery (%)*	*Total Manganese Recovery (%)*
830	1:1	medium	91.2	95.5	86.9	100.2	100.2
830	2:1	medium	99.2	101.8	100.0	100.7	101.7
830	3:1	medium	99.8	94.7	94.6	99.8	99.1
871	1:1	large	98.7	97.7	94.0	102.6	101.4
897	1:1	large	98.1	94.9	93.3	99.7	101.8
922	1:1	large	100.2	97.9	100.0	98.1	99.3
946	1:1	large	99.0	99.8	100.0	98.8	99.4

In the examples in Table 5, the direct causticizing reactions were run essentially to completion. The only exception was the 830 °C, 1:1 reaction. It was stopped prior to completion of the reaction, so complete conversion was not obtained. The discrepancies in the efficiencies are connected to the definitions. The hydrolysis efficiency is based on the amount of $NaMnO_2$, which is calculated from the direct causticizing efficiency. The overall efficiency gives a better representation of the process because it is only based on the final product.

EFFECT OF SODIUM SULFIDE

The previously presented work focused on the direct causticizing reaction for the soda pulping process. In order to be applicable to kraft pulping, sulfur components need to be added to the mix. The sulfur in kraft pulping liquor generally comes from Na_2S. When dissolved in water, Na_2S forms HS^-, the active sulfur component in pulping. When Na_2SO_4 is dissolved in water, $SO_4^=$ is primarily formed. In order to get HS^-, the sulfur species must be in reduced form. Therefore, Na_2S is acceptable for a kraft pulping liquor while Na_2SO_4 is not. Na_2S was selected as the reduced sulfur species to mix with the Na_2CO_3 for the synthetic smelt used in this study.

Anhydrous Na_2S was found to be extremely reactive with air. Even with the precaution of a nitrogen glove bag, the Na_2S was determined to undergo some oxidation while loading the sample into the reactor. This high reactivity made it unsuitable as a reagent because it was too difficult to quantitatively know how much Na_2S was added to the reaction mixture.

$Na_2S \cdot 9H_2O$ was found to be a better alternative for use as a Na_2S source. The compound did not oxidize when exposed to air. This enabled the quantitative addition of Na_2S to the reaction mixture. The additional water was removed during a pre-heating step for the reaction mixture. The reactants were heated at 300 °C for 1 hour in flowing N_2 prior to the start of the reaction. The water removal could be monitored with the IR

CO_2 detector. The CO_2 meter was sensitive to moisture and would record a disturbance if H_2O was present. Following the drying, the CO_2 meter returned to the baseline.

The Na_2S was added to the Na_2CO_3 and Mn_3O_4 reaction mixture with a sulfide initial molar ratio, Na_2S:Na_2CO_3, of 0.33:1. This is similar to what is found in a typical kraft chemical recovery cycle. This sulfide addition was found to depress the melting point of the mixture below 800 °C. In order to conduct the reaction in the solid state, a temperature of 740 °C was chosen to study the effects of Na_2S.

A mixture with small Mn_3O_4 and Mn_3O_4:Na_2CO_3 initial molar ratio of 2:1 was prepared. The Na_2S was added, as $Na_2S \cdot 9H_2O$, with the Na_2S:Na_2CO_3 ratio of 0.33:1. The mixture was reacted at 740 °C for 18 hours in flowing N_2. Following the reaction, the material was transferred to a nitrogen filled container, then immediately analyzed with XRD. The experiment was repeated with the product being immediately transferred to the hydrolysis step instead of the XRD. The hydrolysis was conducted with a nitrogen purge. Following hydrolysis some filtrate was removed directly from the solution for analysis. This was to avoid air contact during a filtering operation. The filtrate was analyzed with the ABC titration and capillary ion electrophoresis.

The XRD analysis of the pre-hydrolysis solid material indicated that some $NaMnO_2$ was formed as seen in Figure 73. Mn_3O_4 was also present. In addition, there was also a strong peak for MnO. There were no peaks for Na_2S or MnS. It was originally thought that the Na_2S may have oxidized during the XRD procedure, resulting

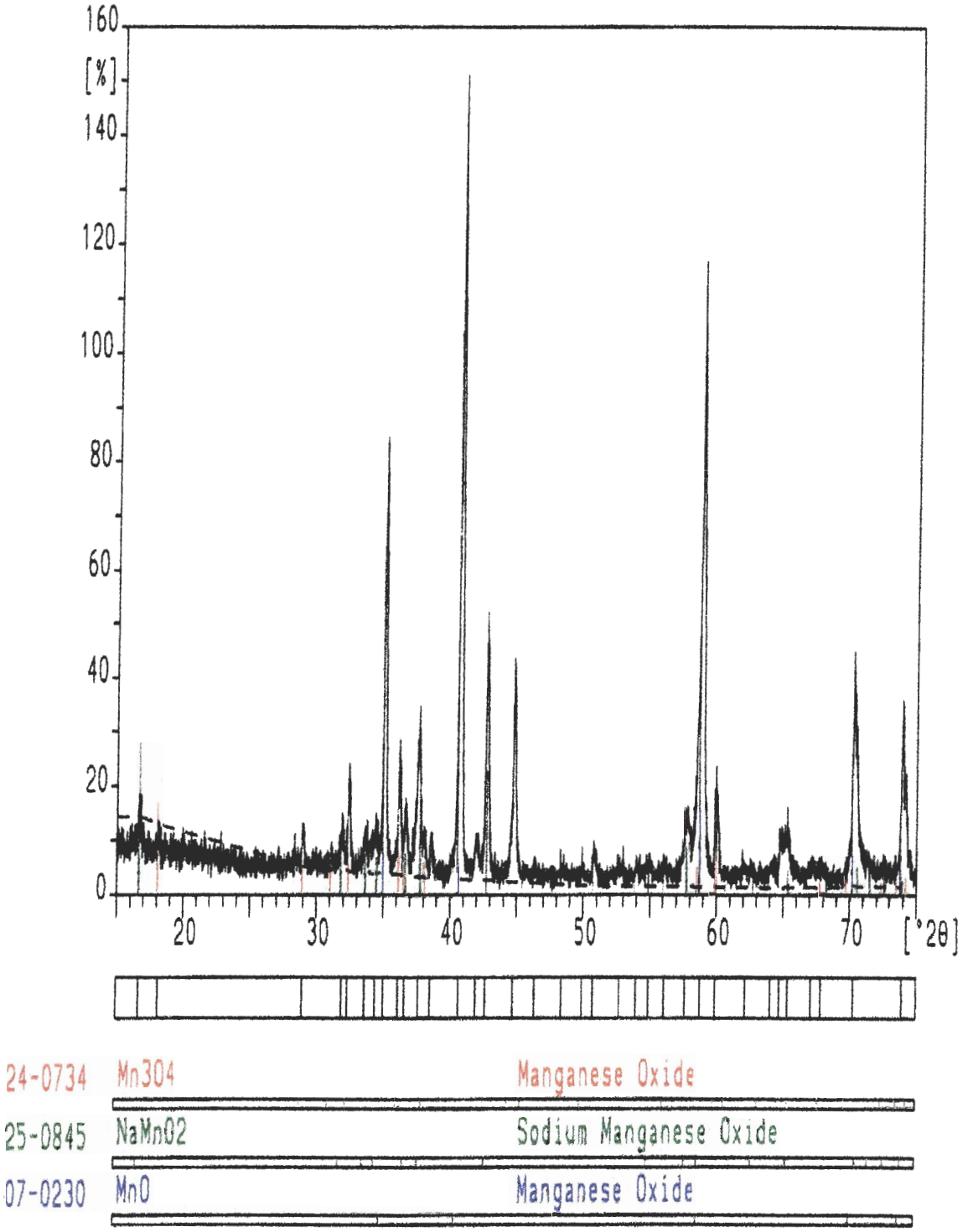

Figure 73 XRD scan of direct causticizing with Na_2S reaction product. 740 °C, small Mn_3O_4, Mn_3O_4:Na_2CO_3 2:1, Na_2S:Na_2CO_3 0.33:1.

in no detection of Na_2S or Na_2SO_4. It is also possible that the relatively small amount of initial sulfide was overwhelmed by the other peaks.

Analysis of the filtrate from hydrolysis with the ABC titration also did not detect any Na_2S. The capillary ion electrophoresis analysis of the filtrate indicated the sulfur species were transformed into sulfate and thiosulfate as shown in Figure 74. The analysis also indicates that the Na_2CO_3 was not completely converted to NaOH. This implies that a detrimental side reaction occurred at a faster rate than the direct causticizing reaction.

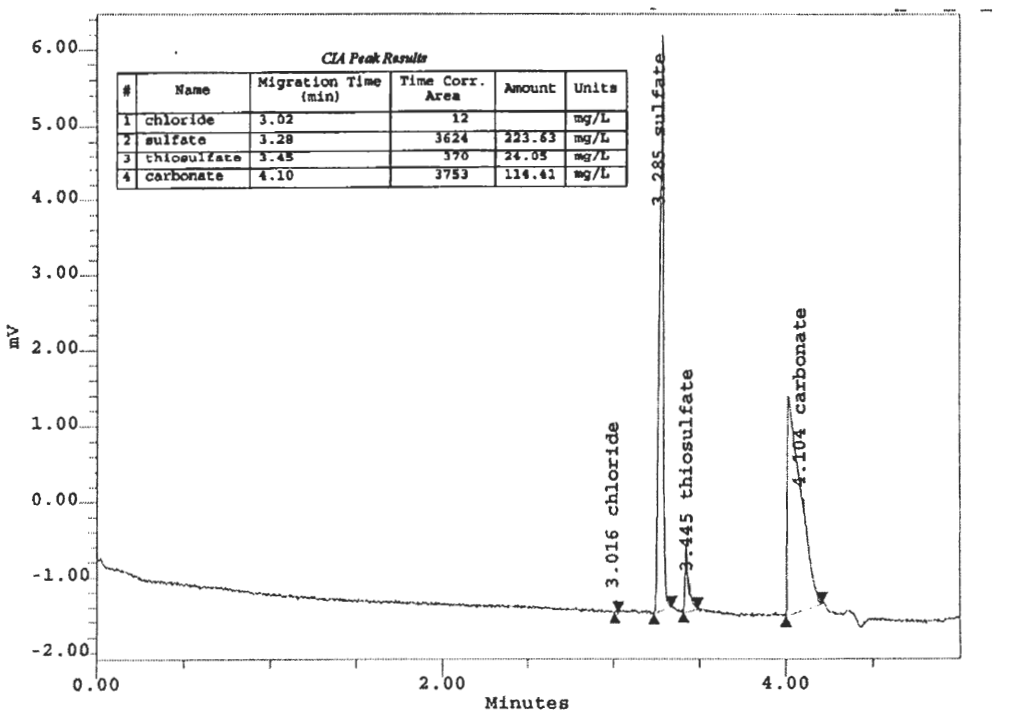

Figure 74 Capillary ion electrophoresis results for post-hydrolysis sulfur containing liquor.

The absence of sulfide in the direct causticizing and hydrolysis products indicated that a detrimental side reaction was taking place. To study it further, an experiment with

only Na_2S and Mn_3O_4 was completed. A Na_2S:Mn_3O_4 1:2 mixture was reacted at 740 °C for 15 hours. The XRD analysis of the direct causticizing product is shown in Figure 75. The dominant peaks were from MnO, with Na_2SO_4 also being identified. The peak at 44.8° is from the low background holder. The amount of MnO relative to Na_2SO_4 was quite large, as judged from the peak intensities. The overwhelming intensity of the MnO signal is probably why Na_2S and Mn_3O_4 were not identified. This result indicated that a reaction was occurring between the Na_2S and Mn_3O_4.

Initially, the concern was that Na_2S would react with Mn_3O_4 to form MnS. This does not appear to be happening. Thermodynamic calculations were performed to determine the Gibbs free energy of reaction between Na_2S and Mn_3O_4. The results are summarized in Table 6.

Table 6 Gibbs free energy of reaction for Na_2S and Mn_3O_4.

Temp (°C)	$Na_2S + 2O_2 \Leftrightarrow Na_2SO_4$ ΔG_f (kJ/mol)	$2Mn_3O_4 \Leftrightarrow 6MnO + O_2$ ΔG_f (kJ/mol)	$Na_2S + 4Mn_3O_4 \Leftrightarrow Na_2SO_4 + 12MnO$ ΔG_f (kJ/mol)
100	-879.5	360.2	-159.0
400	-776.5	289.4	-197.8
700	-682.0	218.5	-245.0
1000	-601.7	147.6	-306.4

The results of the first two reactions in the table above were previously known. Na_2S in air will oxidize to the Na_2SO_4. The large negative free energies of formation indicate that the reaction is thermodynamically possible. The Mn_3O_4 was previously determined to be stable in a nitrogen atmosphere in the temperature range of interest for this study. If the temperature would increase to values beyond that listed in the chart, MnO would be formed.

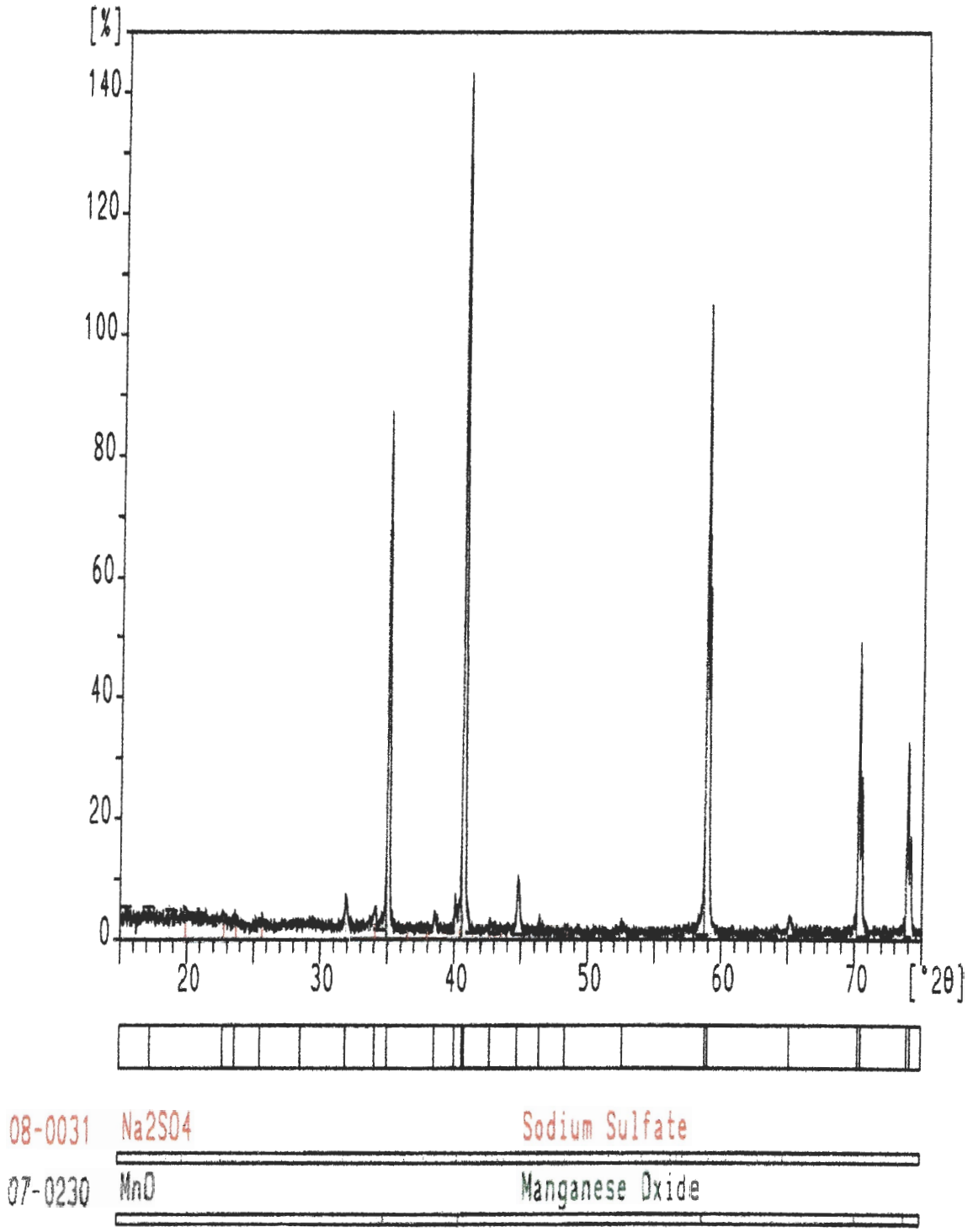

Figure 75 XRD scan of Na_2S and Mn_3O_4 reaction product. 740 °C, small Mn_3O_4, Na_2S:Mn_3O_4 1:2.

The result from the third reaction in Table 6 was not previously known. The thermodynamic calculations suggest that Mn_3O_4 can oxidize Na_2S to Na_2SO_4. It is possible over all temperature ranges of interest. These results appeared to contradict the crucible experiments conducted as a prelude to this work. Those experiments, described in the Problem Analysis, reacted MnO_2, Na_2CO_3, and Na_2S at 800 °C for 60 and 120 minutes. Following hydrolysis, Na_2S was found in the filtrate.

Further analysis of the initial crucible experiments suggested that the Na_2S was actually present. The MnO_2 likely was reduced to Mn_3O_4 with the following stoichiometry.

Equation 47

$$3MnO_2 \Rightarrow Mn_3O_4 + O_2$$

The Mn_3O_4 probably reacted with the Na_2S and Na_2CO_3 simultaneously. The Na_2S reaction is represented by

Equation 48

$$Na_2S + 4Mn_3O_4 \Rightarrow Na_2SO_4 + 12MnO$$

The initial stoichiometry of reactants were MnO_2:Na_2S=3:1 and MnO_2:Na_2CO_3=1:1. If all MnO_2 went to Mn_3O_4, the equivalent Mn_3O_4:Na_2S ratio would be 1:1, and similarly Mn_3O_4:Na_2CO_3=1:1. From Equation 48, 4 moles of Mn_3O_4 are required for 1 mole of Na_2S. Mn_3O_4 is therefore the limiting reactant, leaving excess Na_2S. Following hydrolysis, NaOH and Na_2S were detected. This implies that the selectivity for the Na_2S

reaction during direct causticizing was not 100%. Some Na_2CO_3 reacted with the Mn_3O_4 to produce $NaMnO_2$. The $NaMnO_2$ subsequently produced NaOH during hydrolysis.

With the Mn_3O_4 based direct causticizing system, the reaction between Na_2S and Mn_3O_4 remains a problem. Because the goal of direct causticizing is to convert Na_2CO_3 into NaOH, a high efficiency for that step would be required. Looking at the worst case, if the Na_2S:Na_2CO_3 ratio were 0.33:1, the Mn_3O_4:Na_2CO_3 ratio would need to be 2.3:1 to ensure complete conversion of Na_2CO_3 to $NaMnO_2$. 1 mole would be used for the reaction with Na_2CO_3 and 1.3 moles would react with the Na_2S. This would still result in an unfavorable situation because the Na_2S would be converted to Na_2SO_4. An additional process step or method would be needed to reduce the Na_2SO_4. Similarly, the MnO would need to undergo an oxidation step to form Mn_3O_4 before re-use.

In a conventional recovery boiler, the reduction of Na_2SO_4 to Na_2S primarily occurs through either of the following reactions.

Equation 49 $$Na_2SO_4 + 2C \Rightarrow Na_2S + CO_2$$

Equation 50 $$Na_2SO_4 + 4C \Rightarrow Na_2S + 4CO$$

The carbon is present in the black liquor and results in the production of Na_2S. The Na_2S can also be oxidized by the combustion air, but the reaction becomes mass-transfer limited. At high temperatures, ~1000 °C, Equation 49 and Equation 50 occur at a higher rate than the Na_2S oxidation, resulting in high reduction efficiencies.

The use of carbon as a reducing agent for the Na_2SO_4, while direct causticizing with Mn_3O_4, was investigated at 740 °C. Carbon was added to the reaction mixture with a C:Na_2S ratio of 2:1. Mn_3O_4:Na_2CO_3 and Na_2S:Na_2CO_3 ratios were 2:1 and 0.33:1 respectively. The experiment was allowed to react for 15 hours. Two identical runs were completed with the solid products going to XRD analysis and hydrolysis.

XRD spectra for the pre-hydrolysis direct causticizing product, shown in Figure 76, indicated MnO and $NaMnO_2$ were the dominant species. The peak at a 2θ angle of 44.8° is attributed to the low background holder. Again, Na_2SO_4 and Na_2S were not identified in the direct causticizing reaction product, presumably due to the relatively low concentration of sulfur species and the dominance of the MnO.

The hydrolyzed product was analyzed with the ABC titration and NaOH and Na_2CO_3 were found in the liquor. The presence of Na_2S was not detected. The presence of NaOH is in agreement with expectations because of the $NaMnO_2$ found by XRD of the direct causticizing product. The residual Na_2CO_3 indicates that complete conversion was not achieved. The liquor was not analyzed with capillary ion electrophoresis for $SO_4^{=}$.

The strong MnO peaks from the direct causticizing product, and the lack of Na_2S in the hydrolysis product, indicate that the presence of carbon in the reaction mixture did not keep the Na_2S as a reduced component, for the given reaction conditions. Na_2S appears to react with Mn_3O_4, reducing it to MnO, and deactivating it as a direct

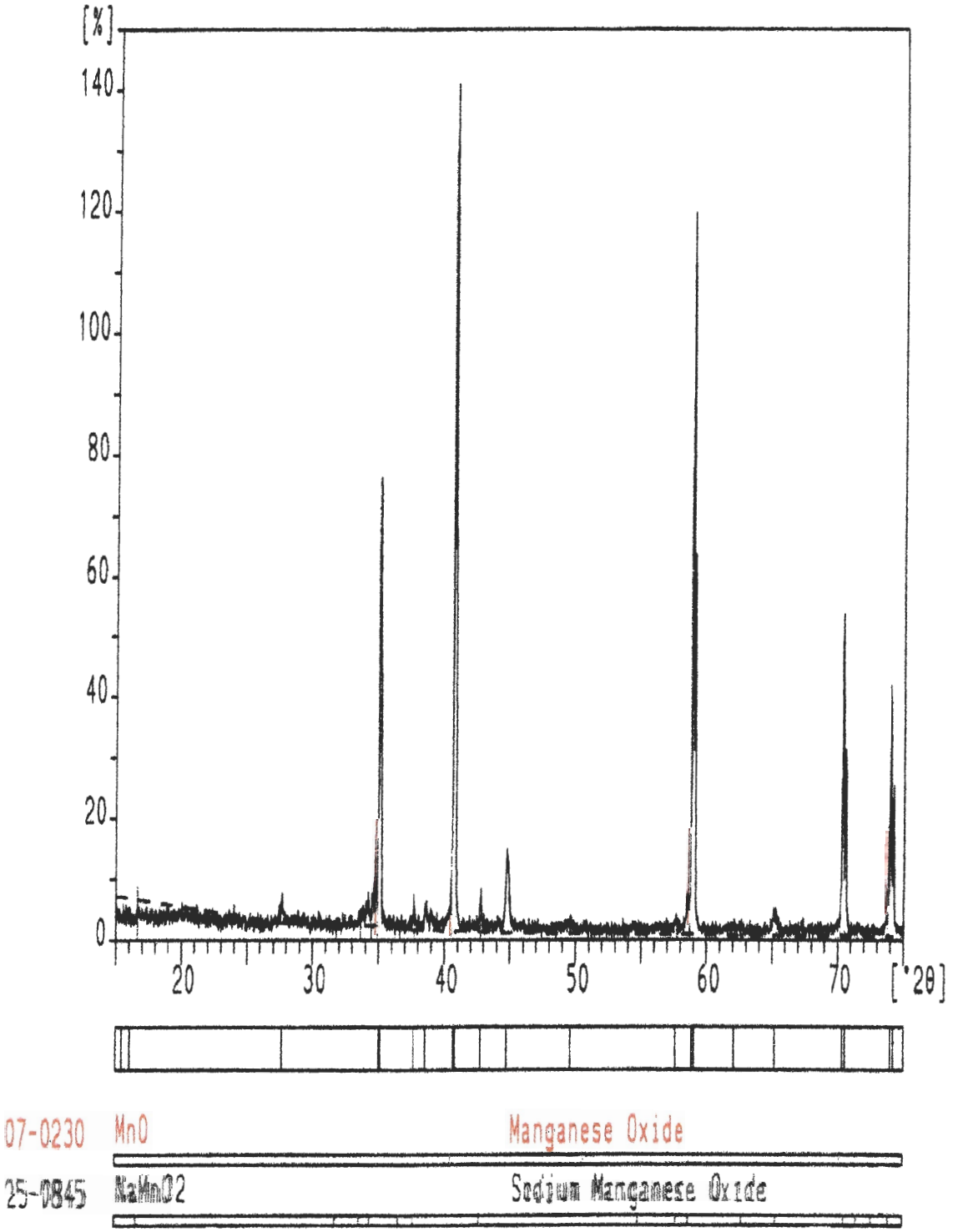

Figure 76 XRD scan of direct causticizing reaction product with Na_2S and carbon initially present. 740 °C, small Mn_3O_4, Mn_3O_4:Na_2CO_3 2:1, Na_2S:Na_2CO_3 0.33:1, C:Na_2S 2:1.

causticizing agent. In addition, Na_2SO_4 is produced, which was not simultaneously reduced to Na_2S with carbon. For a DARS process, the MnO would have to be oxidized to Mn_3O_4 before re-use. Additionally, the Na_2SO_4 would need to be reduced to Na_2S.

CONTRIBUTIONS AND CONCLUSIONS

The overall purpose of this work was to investigate the feasibility of developing a manganese oxide based direct causticizing process for the recovery of kraft black liquors. A specific understanding of the kinetics of the direct causticizing reaction would provide critical information in the design of a commercial process. In addition, the overall process efficiency and how the direct causticizing reaction is affected by the presence of sodium sulfide would also be required information.

Mn_3O_4 was identified as the best choice of the manganese oxides to serve as a direct causticizing agent for the sulfur-free system. MnO_2 and Mn_2O_3 were found to undergo thermal reduction to Mn_3O_4 over the temperature range of 650-950 °C. However, Mn_3O_4 was stable as a reactant at these temperatures.

The direct causticizing reaction between Mn_3O_4 and Na_2CO_3 was determined to occur with a 1:1 stoichiometry.

The temperature, particle size, and initial molar ratio of reactants were studied to see how they affected the reaction kinetics for the direct causticizing reaction between Mn_3O_4 and Na_2CO_3. In the solid state, from 650 to 850 °C, the reaction was found to have an activation energy of 206 kJ/mol. With molten Na_2CO_3, in the temperature range of 850 to 950°C, the reaction had an activation energy of 174 kJ/mol. Transition from

the solid-solid reaction to the solid-liquid reaction increased the reaction rate constant by 40 times.

The overall particle radius of the Mn_3O_4 was found to have an effect on the reaction rate constants. Increases in the particle size slowed the reaction. However, the reaction rate did not follow a $1/r^2$ dependence on particle size as expected. This deviation is attributed to the non-spherical nature of the Mn_3O_4 particles used in this study.

An increase in the initial molar ratio of Mn_3O_4:Na_2CO_3 was found to increase the rate of Na_2CO_3 conversion. This corresponded to a decrease in the reaction rate constant based on the conversion of Mn_3O_4. The effect of the initial molar ratio of reactants on the reaction rate constant followed an empirical power law dependence.

The reaction between Mn_3O_4 and Na_2CO_3 in the temperature range of 650 to 950 °C, is well described by the Ginstling-Brounshtein product layer diffusion controlled model. The model was applicable over Na_2CO_3 conversions of 10 - 80%, depending on the initial Mn_3O_4 particle size. For relatively large particles of non-uniform size and shape, the initial part of the reaction is better described by a contracting area model, followed by a transition to product layer diffusion control.

The direct causticizing reaction and subsequent hydrolysis of the product were found to have very high efficiencies. Neither step was found to be equilibrium limited. In addition, the Mn_3O_4 could be regenerated in the lab with no loss of material.

The presence of Na_2S was found to have a negative impact on the direct causticizing reaction. Na_2S reduced Mn_3O_4 to MnO while being oxidized to Na_2SO_4. For direct causticizing with Mn_3O_4 to be feasible, the deactivated Mn_3O_4 would need to undergo a reoxidation step. In addition, hydrogenation of Na_2SO_4, or some other method of reduction, would be required to regenerate Na_2S.

SUGGESTIONS FOR FUTURE WORK

The results of this work were expected to reveal a direct causticizing system that would be compatible with the kraft pulping process. The presence of Na_2S was found to deactivate the Mn_3O_4 to MnO, an inactive direct causticizing agent. For this reason, kraft based direct causticizing with Mn_3O_4, in the presence of Na_2S, would require separate process steps for the oxidation of MnO, and reduction of Na_2SO_4.

One scenario that could be possible is to direct causticize with an excess of Mn_3O_4. As shown above, a Mn_3O_4:Na_2CO_3 ratio of 2.33:1 is required for Na_2S:Na_2CO_3 ratios of 0.33:1. This would result in complete conversion of Na_2CO_3 to $NaMnO_2$, and the complete conversion of Na_2S to Na_2SO_4. The solid reaction product could then be subjected to hydrogenation to convert the Na_2SO_4 to Na_2S. The hydrogenation of Na_2SO_4 in the presence of sodium titanates was previously studied by Zou.[19] He found that the reaction initially proceeds by a nucleation and growth mechanism and then changes to a shrinking core model with hydrogen diffusion control. This process could

possibly be applied to mixtures of sodium manganates and Na_2SO_4. Following the reduction, hydrolysis and solids separation would yield a solid stream of manganese oxides and an aqueous steam containing the white liquor. The manganese oxides could be simultaneously dried and reoxidized in an air oxidizer.

Another scenario is to remove the Na_2S prior to the direct causticizing step. Low temperature black liquor gasification processes release the reduced sulfides primarily as H_2S. If this were technically feasible, the problem of Mn_3O_4 deactivation by Na_2S would be removed. Currently a major problem with low temperature gasification is how to efficiently recover the H_2S from the product gas. If that problem was solved, then Mn_3O_4 based direct causticizing of the solid gasification product could be of interest.

Another area of interest to direct causticizing in general is the removal of non-process elements. The current CaO based causticizing system has provisions for a mill purge with the dregs and grits streams. A Fe_2O_3, TiO_2, or Mn_3O_4 based direct causticizing process would need some way to accomplish this also.

ACKNOWLEDGEMENTS

I would like to thank many people for their support of this project. I am grateful to Dr. H. "Jeff" Empie for serving as my advisor. His "hands-off" approach to advising of this project made it a very valuable learning experience for me. I was able to work at my own pace, investigate areas that interested me, and make my own mistakes. His accessibility was superb along with his encouragement, which was always welcome. I also wish to thank my thesis committee, Drs. Alan Rudie, Junyong Zhu, and Mary Rezac, for their input during the course of my work.

I would also like to thank the Institute of Paper Science and Technology and its Member Companies for their financial support, without which, this would not have been possible. In addition, the IPST community of students, staff, and faculty made for a very comfortable environment in which to study, grow, and have fun.

Finally, I would like to thank my wife, Momoka, for all of her support and encouragement. Her patience and understanding over the years was truly appreciated.

LIST OF SYMBOLS

Symbols

a	stoichiometric coefficient for reaction
b	stoichiometric coefficient for reaction
A	frequency factor, s^{-1}
C_o	concentration of species O, mol/cm^3
D	diffusivity, cm^2/s
E	activation energy, kJ/mol
Eff_o	overall process efficiency, %
Eff_{dc}	direct causticizing efficiency, %
Eff_h	hydrolysis efficiency, %
k	kinetic rate constant, s^{-1}
n	power dependence
r	initial particle radius, cm
R	universal gas constant, kJ/mol K
s	particle radius of unreacted material following reaction, cm
t	time, s
T	temperature, °K
V_M	molar volume, cm^3/mol
X	product layer thickness, cm
x	stoichiometric coefficient for chemical compound
y	stoichiometric coefficient for chemical compound
z	stoichiometric coefficient for chemical compound

Subscripts

d	diffusion
i	initial
t	time

Greek Symbols

α	fractional conversion
β	number of steps in nucleus formation
ε	power dependence for initial molar ratio in frequency factor
φ	pre-power factor for initial molar ratio in frequency factor, s^{-1}
λ	number of dimensions for nucleus growth
θ	angle

Abbreviations

ATS	Applied Test Systems, Inc.
A-E	Avrami-Erofe'ev
DARS	Direct Alkali Regeneration System
DTA	ifferential thermogravimetric analysis
EDS	energy dispersive x-ray spectroscopy
G-B	Ginstling-Brounshtein
SEM	scanning electron microscopy
TG	thermogravimetry

TGA	thermogravimetric analysis
XRD	x-ray diffraction

Chemical Compounds

C	carbon
$CaCO_3$	calcium carbonate
CaO	calcium oxide
$Ca(OH)_2$	calcium hydroxide
CO_2	carbon dioxide
Fe_2O_3	iron oxide
H_2O	water
MnO	manganese (II) oxide
MnO_2	manganese (IV) oxide
Mn_2O_3	manganese (III) oxide
Mn_3O_4	manganese (II,III) oxide
Na_2CO_3	sodium carbonate
$NaMnO_2$	sodium manganate
$Na_2OFe_2O_3$	sodium ferrite
Na_2S	sodium sulfide
Na_2SO_4	sodium sulfate
TiO_2	titanium dioxide

LITERATURE CITED

[1] Pulp and Paper Manufacture, 3rd ed., Vol. 5 Alkaline Pulping, Grace, T. and Malcolm, E. Eds., Joint Textbook Committee of the Paper Industry, Atlanta, GA, (1989).

[2] Chemical Recovery in the Alkaline Pulping Process, 3rd ed. Green, R. and Hough, G. Eds., Tappi Press, Atlanta, GA, (1992).

[3] Grace, T., "An Evaluation of Nonconventional Causticizing Technology for Kraft Chemical Recovery", IPC Project 3473-3, Progress Report One, Institute of Paper Chemistry, Appleton, WI, (1981).

[4] Covey, G., "DARS – The Direct Alkali Recovery System", The Pacific Section of Tappi, 37th Annual Seminar, Tappi Press, Atlanta, GA, (1984).

[5] Maddern, K., "Mill-Scale Development of the DARS Direct Causticization Process", Pulp and Paper Canada, 87 (10): 78-82, (1986).

[6] Zou, X., Kubes, G., van Heiningen, A., and Avedesian, M., "Autocausticizing of Kraft Black Liquor: Process Implications Based on Chemical Equilibrium Calculations", Proceedings of the 1990 Tappi Pulping Conference, 897-903, Tappi Press, Atlanta, GA, (1990).

[7] Zeng, L. and van Heiningen, A., "Pilot Fluidized-Bed Testing of Kraft Black Liquor Gasification and its Direct Causticization with TiO_2", Journal of Pulp and Paper Science, 23(11): 511-516, (1997).

[8] Budney, J., "Method of Recovering Caustic Soda from Spent Pulping Liquors", Canadian Patent 1,283,256 (1991).

[9] Kiiskila, E. and Virkola, N., "Recovery of Sodium Hydroxide From Alkaline Pulping Liquors by Autocausticizing. Part I. General Aspects", Paperi ja Puu, 60 (3):129-132, (1978).

[10] Janson, J., "The Use of Unconventional Alkali in Cooking and Bleaching. Part1. A New Approach to Liquor Generation and Alkalinity", Paperi ja Pu, 59 (6-7): 425-430, (1977).

[11] Tsukamoto, H., "Direct Causticizing Technology", Japan Tappi, 40 (1): 44-50, (1986)

[12] Kiiskila, E., "Recovery of Sodium Hydroxide From Alkaline Pulping Liquors by Autocausticizing. Part II. Reactions Between Sodium Carbonate and Titanium Dioxide:, Paperi ja Puu, 61 (5): 453-463, (1979).

[13] Kiiskila, E., "Recovery of Sodium Hydroxide From Alkaline Pulping Liquors by Autocausticizing. Part III. Alkali Distribution in Titanium Dioxide Causticizing", Paperi ja Puu, 61 (6-7): 453-463, (1979).

[14] Kiiskila, E., "Recovery of Sodium Hydroxide From Alkaline Pulping Liquors by Autocausticizing. Part V. Causticization of Molten Sodium Carbonate by Ilmenite", Paperi ja Puu, 61 (9): 564-577, (1979).

[15] Kiiskila, E., "Recovery of Sodium Hydroxide From Alkaline Pulping Liquors by Autocausticizing. Part VI. Comparison of Various Causticizing Chemicals", Paperi ja Puu, 61 (10): 639-650, (1979).

[16] Kiiskila, E., "Recovery of Sodium Hydroxide From Alkaline Pulping Liquors by Causticizing Molten Sodium Carbonate with Amphoteric Oxides", Paperi ja Puu, 62 (5): 339-350, (1980).

[17] Kiiskila, E. and Valkonen, N., "Recovery of Sodium Hydroxide From Alkaline Pulping Liquors by Direct Causticizing. Part IV. Causticizing Sodium Carbonate with Ferric Oxide", Paperi ja Puu, 61 (8): 505-510, (1979).

[18] Seymour, C., "The Application of the Direct Alkali Recovery System (DARS) to the Kraft Pulping Process" A-190 Independent Research Study, Institute of Paper Science and Technology, (1991).

[19] Zou, X., "Recovery of Kraft Black Liquor Including Deirect Causticization", Ph.D. Thesis, McGill University, Montreal (1991).

[20] Zou, X., Avedesian, M., van Heiningen, A., "Kraft Black Liquor Combustion and Direct Causticization with Titanium Dioxide", Proceedings of the 1991 Tappi Pulping Conference, 299-308, Tappi Press, Atlanta, GA, (1991).

[21] Zeng, L., "Kraft Black Liquor Gasification and Direct Causticization with TiO2 in a Fluidized Bed", Ph.D. Thesis, University of New Brunswick, Fredericton, NB (1997).

[22] Pels, J., Zeng, L., and van Heiningen, A., "Direct Causticization of Kraft Black Liquor with TiO_2 in a Fluidized Bed – Identification and Analysis of Sodium Titanates", Journal of Pulp and Paper Science, 23(12): 549-554 (1997).

[23] Jones, A., ABB Combustion Engineerring, personal communication. (1996).

[24] Comprehensive Chemical Kinetics Vol. 22 Reactions in the Solid State, Bamford, C. and Tipper, C. (Ed.), Elsevier, Amsterdam, (1980).

[25] Jost, W., Diffusion in Solids, Liquids, Gases. Academic Press, New York, (1952).

[26] Ashby, M. and Jones, D., Engineering Materials 1: An Introduction to their Properties and Applications, Pergamon Press, New York, (1980).

[27] Shewmon, P., Diffusion in Solids. Williams Book Company, Jenks, OK, (1983).

[28] Jacobs, P. and Tompkins, F., in Garner (Ed.), Chemistry of the Solid State, Butterworth, London, (1955).

[29] Young, D., Decomposition of Solids, Pergamon Press, Oxford, 1966.

[30] Avrami, M., "Kinetics of Phase Change, II. Transformation-Time Relations for Random Distribution of Nuclei", J. Chem. Phys, 8, 212-220, (1939).

[31] Erofe'ev, B., Compt. Rend. Acad. Sci. URSS, 52, 511-521, (1946).

[32] Wagner, C., Z. Physik. Chem., B32, 447-456 (1936).

[33] Kubaschewski, O. and Hopkins, B., Oxidation of Metals and Alloys, Butterworth, London, (1962).

[34] Jander, W., Z. Anorg. Allgem. Chem., 163, 1-16, (1927).

[35] Giess, E., Journal of the American Ceramic Society., 46, 374-379 (1963).

[36] Ginstling, A. and Brounshtein, B., J. Appl. Chem. U.S.S.R., 23, 1327-1338 (1950).

[37] Gasik, M., Kucher, A., Khitrik, S., and Ashin, A., "Reaction of Manganese Oxides with Sodium Carbonate" Izv. VUZ, Chernaya Metallurgiya (6) 22-25 (1968).

[38] Colovic, N., Antonijevic, M., and Milic S., "Investigation of the Kinetics of the Reactions Between Sodium Carbonate and Oxides of Transition Metals" Thermochimica Acta, 223, 113-125 (1994).

[39] Giovanoli, R., "Thermogravimetry of Manganese Dioxides", Thermochimica Acta, Vol. 234, pp. 303-313, (1994).

[40] Molten Salt Techniques, Volume 2, Lovering, D. and Gale, R. Eds., Plenum Press, New York, (1984).

[41] "Method 2320, Alkalinity", Standard Methods for the Examination of Water and Wastewater, 18th Edition. Greenberg, A., Clesceri, L., and Eaton, A. (Eds.) Washington (1992).

[42] Foust, A., Principles of Unit Operations, 2nd Edition. Wiley, New York, (1980).

[43] Kirk, R. Encyclopedia of Chemical Technology, Volume 15, 4th Edition. Wiley, New York, (1991).

[44] Budnikov P. and Ginstling A., Principles of Solid State Chemistry: Reactions in Solids, Shaw K., transl. and ed., McClaren, London, (1968).

[45] Johnson, D. and Gallagher, P., "Reaction Kinetics in Heterogeneous Chemical Systems", Journal of the American Ceramic Society, 59 (171) pp 573 (1976).

[46] Bevington P. and Robinson D., Data Reduction and Error Analysis for the Physical Sciences, 2nd ed., McGraw-Hill, New York, (1992).

[47] Kline, S. and McClintock, F., "Describing Uncertainties in Single-Sample Experiments", Mech. Eng., 75, 1, pp. 3-9, January, (1953).

APPENDIX I – DETAILED EXPERIMENTAL PROCEDURE

Isothermal Direct Causticizing Reaction

1. Turn on mass flow meters, furnace, IR detectors, and data acquisition computer.
2. Turn on N_2 purge to low range IR CO_2 detector at 1.0 SLPM.
3. Turn on N_2 carrier gas at 1.0 SLPM.
4. Pre-heat furnace to desired pre-heat temperature.
5. Zero CO_2 detectors.
6. Calibrate CO_2 detectors with 1.0 SLPM 1800 ppm and 9.98% CO_2 for low and high range detectors, respectively.
7. Weigh alumina sample boat.
8. Weigh Na_2CO_3 and Mn_3O_4, mix, place in alumina sample boat.
9. Open cold end of reactor, attach sample boat to plunger.
10. Close reactor with sample boat remaining at cold end.
11. Insert sample boat a fraction of the way into the furnace with plunger until the boat temperature reaches 300 °C.
12. Allow sample to dry for 1 hour.
13. Simultaneously start data acquisition and insert sample boat into pre-heated reaction zone in furnace.
14. Change furnace temperature controller to sample boat thermocouple.
15. Reset furnace temperature controller setpoint to isothermal reaction temperature.
16. Monitor the reaction with the CO_2 detector signal.
17. When finished, shut off furnace.
18. Stop data acquisition.
19. Upon cooling, shut off N2 carrier gas.
20. Withdraw sample from core of furnace with plunger.
21. Open reactor and detach sample boat from plunger.
22. Weigh sample boat.
23. Transfer product to sample bottle, purge with N_2, store in dessicator.

Hydrolysis of Direct Causticizing Product

1. Boil de-ionized water with N_2 purge for 30 minutes.
2. Weigh direct causticizing product.
3. Put material in 250 ml Erlenmeyer flask with 100 ml of water and 1.9 cm stir bar.
4. Attach water cooled condenser to flask and secure apparatus on hotplate.
5. Attach N_2 purge and insert thermometer.
6. Heat for 5 hours at 90 °C with a stir bar rotation of approximately 120 rpm.
7. Weigh 4.7 cm filter.
8. Vacuum filter mixture, adding aliquots of water to rinse out Erlenmeyer flask.
9. Dilute filtrate to 250 ml and store in N_2 purged propylene bottle.
10. Dry filter with solid material overnight at 105 °C.
11. Weigh filter and sample.

APPENDIX II – THERMAL PROFILE OF REACTOR VESSEL

A temperature gradient in the furnace existed because of thermal losses at the ends and the flowing carrier gas. The reactor vessel was profiled to determine the optimal placement of the sample boat. For the profiling experiments, the furnace was controlled by a thermocouple placed on the outside of the alumina retort, at the midpoint of the furnace. The N_2 carrier gas was turned on at 1 SLPM and setpoint temperatures of 600, 700, and 800 °C were studied. A calibrated Type K thermocouple was used in place of the plunger, with gradient markings on it to determine the position within the furnace. Equilibrium readings were obtained throughout the reactor vessel as shown in Figure 77. From the graph, a position of 20.3 cm (8 inches) was selected as the optimum point for the sample boat.

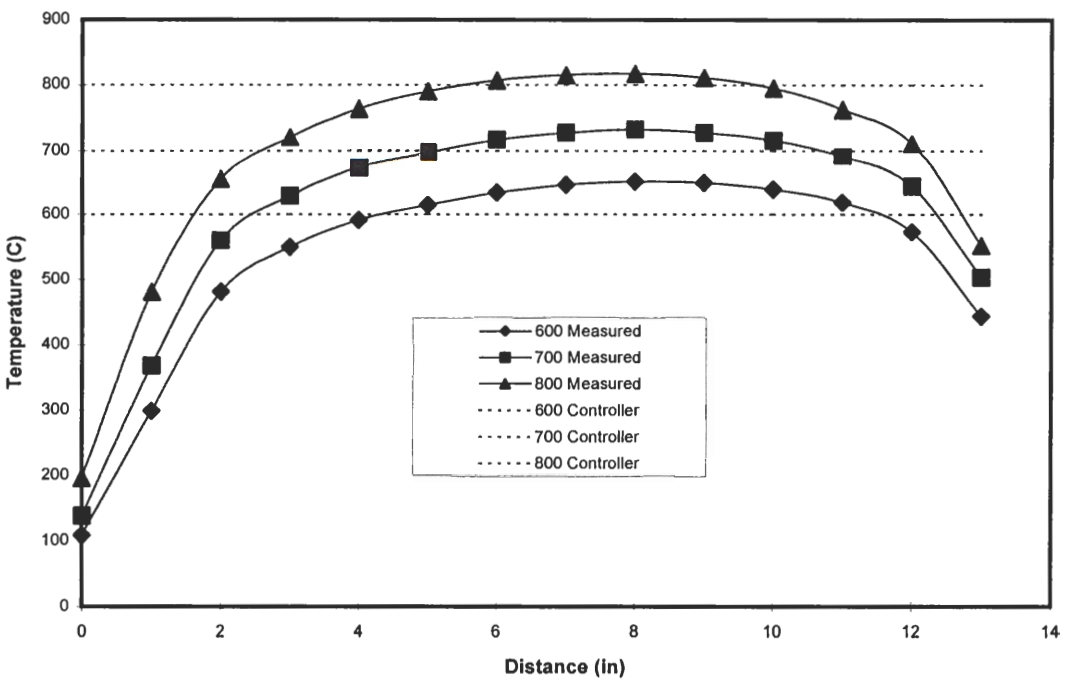

Figure 77 Temperature profile in reactor vessel.

For the experiments, during pre-heating, the reactor temperature was controlled by a thermocouple inside the reactor vessel located 22.9 cm (9 inches) from the cold end (left). It was inserted into the reactor vessel from the hot end (right). At the start of the reaction, the reactor vessel was moved to the reaction zone with the combination plunger/thermocouple. Temperature control was switched to the sample thermocouple to ensure accurate readings.

Statistical analysis of data from 8 experiments showed that there was a standard deviation of ±2 °C in the temperature reading.

APPENDIX III – UNCERTAINTY ANALYSIS FOR k

The measurement of the kinetic rate constant, k, has a certain amount of uncertainty. The uncertainty was estimated with two methods. The first method for estimating the uncertainty in the kinetic rate constant was based on the error propagation equation presented by Bevington and Robinson[46] and further discussed by Kline and McClintock.[47] The second method estimated the uncertainty by performing 11 replicate experiments and determining the average of the standard error in the measurements.

The relative uncertainty of a quantity calculated from independently measured quantities is given by the following.

Equation 51

$$\hat{U}(f) = \left[\sum \left\{ \left({}^{y_i}/_{f} \right) {}^{\partial f}/_{\partial y_i} \right\}^2 \hat{U}(y_i)^2 \right]^{0.5}$$

f is the function used to calculate the desired value. y_i is an independently measured quantity and $\hat{U}(y_i)$ is the uncertainty associated with the measurement. The determination of the kinetic rate constant is derived from a series of calculations, so the uncertainty for k is determined as it propagates through the calculations.

The molar flow rate of CO_2 was determined by multiplying the CO_2 concentration by the carrier gas flow rate.

Equation 52

$$F_{CO_2} = [CO_2] \times SLPM$$

F_{CO_2} is the molar flow rate as moles of CO_2 per minute. $[CO_2]$ is the CO_2 concentration in the carrier gas as moles per liter. SLPM is the carrier gas flow rate as liters per minute. The relative uncertainty in the molar flow rate of CO_2 is then given by

Equation 53

$$\hat{U}(F_{CO_2}) = \left[(1)^2 \times \hat{U}([CO_2])^2 + (1)^2 \times \hat{U}(SLPM)^2 \right]^{0.5}.$$

The relative uncertainties from the CO_2 detector and flow meter manufacturers are $\hat{U}([CO_2]) = \pm 0.01$ and $\hat{U}(SLPM) = \pm 0.01$. The resulting uncertainty in the molar flow rate is $\hat{U}(F_{CO_2}) = \pm 0.014$.

During the experiments the molar flow rate was continuously integrated to give the total moles of CO_2 evolved at any time, CO_{2_T}. This did not introduce any additional

error into CO_{2_T} because the calculation did not involve another variable with uncertainty. Therefore, $\hat{U}(CO_{2_T}) = \pm 0.014$.

The conversion at time t, α_t, was calculated from the following expression.

Equation 54

$$\alpha_t = {CO_{2_T} \times (106 g/mol)} \Big/ {Na_2CO_3 w}$$

$Na_2CO_3 w$ is the weight of sodium carbonate used in the direct causticizing reaction. The relative uncertainty in this measurement was estimated from the balance manufacturer to be $\hat{U}(Na_2CO_3 w) = \pm 0.005$. The relative uncertainty in the conversion is calculated from Equation 55.

Equation 55

$$\hat{U}(\alpha_t) = \left[(1)^2 \times \hat{U}(CO_{2_T})^2 + (-1)^2 \times \hat{U}(Na_2CO_3 w)^2\right]^{0.5}$$

The propagation of measurement errors leads to conversions with relative uncertainties of about 1.5%, $\hat{U}(\alpha_t) = \pm 0.015$.

The Ginstling-Brounshtein equation was used to determine the diffusion limited rate constants. This functionality is

Equation 56

$$k = {\left(1 - \frac{2}{3}\alpha - (1-\alpha)^{2/3}\right)} \Big/ {(t - t_o)}.$$

In the thesis, a plot of the numerator versus time, t, resulted in a line with slope k and offset of t_o. t_o is considered to be the initiation time. The slope of the line was determined over a certain time and conversion range as described in previous sections. From Equation 51 and Equation 56, the relative uncertainty in the kinetic rate constant is estimated as follows.

Equation 57

$$\hat{U}(k) = \left[\left(\alpha \frac{-\frac{2}{3} + \frac{2}{3}(1-\alpha)^{-1/3}}{1 - \left(\frac{2}{3}\right)\alpha - (1-\alpha)^{2/3}}\right)^2 \times \hat{U}(\alpha_t)^2 + \left(-\frac{t}{(t-t_o)}\right)^2 \times \hat{U}(t)^2\right]^{0.5}$$

$\hat{U}(t)$ is the uncertainty in the time measurement. It is the uncertainty in the time difference between the insertion of the sample boat into reaction zone and the time to

start the data acquisition. It was minimized by starting the data acquisition first, then inserting the sample at 55 seconds. It took approximately 5 seconds to complete the insertion. During data analysis, 60 seconds were first subtracted from all times. The error was estimated to be very low, $\hat{U}(t) = 0.01$.

Equation 57 is a function of conversion and time. The α function and t function were evaluated to determine their effects on $\hat{U}(k)$. At low conversions and low times, there is less uncertainty in the kinetic rate constant. The dominant term was the conversion function. A sensitivity analysis of the time showed that it had an insignificant impact on $\hat{U}(k)$. A minimum in the uncertainty occurred between 20 and 25% conversion. The impact of the conversion on uncertainty is shown in Table 7. As the reaction reaches completion, the uncertainty increases to greater than 5%. The average estimated relative uncertainty is approximately 4%.

Table 7 Estimates of the uncertainty in the measurement of the kinetic rate constant, k, as a function of conversion.

α_t	$\hat{U}(k)$
0.1	0.037
0.2	0.034
0.3	0.035
0.4	0.036
0.5	0.037
0.6	0.039
0.7	0.042
0.8	0.047
0.9	0.057

Analysis of the experimentally determined kinetic rate constants for 11 duplicate runs indicated that the average relative standard deviation was 16.4%. This experimental value is higher than the estimated uncertainty. The larger relative standard deviation could be attributed to the mixing of the reactants, prior to placing them in the sample boat. The powders were mixed on a piece of waxed weighing paper with a spatula. The color difference, black and white, gave a visual indication of the degree of mixing. The density and size differences of the reactants may have also contributed to inhomogeneous mixing, resulting in the larger experimental error.

APENDIX IV – REDUCED DATA FROM KINETIC EXPERIMENTS

Because the IR CO_2 detector outputs a continuous signal, and the sampling rate was relatively high, a large amount of data was collected. An efficient means to present the pertinent information was desired. The raw kinetic data, temperature and total CO_2 evolved versus time, were evaluated as outlined in the Mathematical Analysis of the Data section. The important parameters and results for each kinetic experiment are summarized below. Abbreviations are listed first.

Expt #	Experiment reference number, corresponds to the date.
Temp.	Isothermal reaction temperature, °C.
Mn_3O_4	Particle size for Mn_3O_4 used in experiment; large, medium, small, or powdered.
ratio	Initial molar ratio of reactants; Mn_3O_4:Na_2CO_3
$Time_T$	Time for reactants to reach isothermal reaction temperature, s.
$Time_{is}$	Time for start of range of applicability for contracting area model, s.
XNa_{is}	Na_2CO_3 conversion at $Time_{is}$, %.
XMn_{is}	Mn_3O_4 conversion at $Time_{is}$, %.
k_i	Kinetic rate constant for contracting area model, s^{-1}.
$Time_{if/ds}$	Time for end of range of applicability for contracting area model and/or start of range of applicability for Ginstling-Brounshtein model, s.
$XNa_{if/ds}$	Na_2CO_3 conversion at $Time_{if/ds}$, %.
$XMn_{if/ds}$	Mn_3O_4 conversion at $Time_{if/ds}$, %.
k_d	Kinetic rate constant for Ginstling-Brounshtein model, s^{-1}.
$Time_{df}$	Time for end of range of applicability for Ginstling-Brounshtein model.
XNa_{df}	Na_2CO_3 conversion at $Time_{df}$, %.
XMn_{df}	Mn_3O_4 conversion at $Time_{df}$, %.
T_f	Total time of reaction, s.
XNa_f	Na_2CO_3 conversion at T_f, %.

Expt #	Temp.	Mn_3O_4	ratio	$Time_T$	$Time_{is}$	XNa_{is}	XMn_{is}	k_i	$Time_{ids}$	XNa_{ids}	XMn_{ids}	k_d	$Time_{df}$	XNa_{df}	XMn_{df}	T_f	XNa_f
102799a	778	powdered	1:4	226					226	3	12	4.64E-05	1341	15	58	18000	24.8
102899a	808	powdered	1:4	226					226	4	16	7.36E-05	951	15	60	15900	25.1
102999a	806	powdered	1:4	195					195	4	14	9.45E-05	965	17	67	6420	24.9
102999b	750	powdered	1:4	200					210	2	6	1.81E-05	10500	23	91	18720	25.1
110399a	745	powdered	1:4	240					240	2	8	1.98E-05	12480	24	96	19260	25.3
110999a	720	powdered	1:4	230					230	1	4	1.12E-05	10380	19	77	27000	24.0
111099a	695	powdered	1:4	251					251	4	15	5.75E-06	18000	19	75	20880	20.0
111199a	675	powdered	1:4	260					1405	4	16	3.72E-06	24600	18	70	29280	18.9
111599a	825	powdered	1:4	196					196	4	16	1.50E-04	941	19	78	4320	25.0
112999b	742	powdered	1:1	150					4635	32	32	3.94E-06	23085	70	70	24965	72.3
113099a	827	powdered	1:1	140					172	7	7	1.42E-05	5175	66	66	5175	65.6
113099b	674	powdered	1:1	220					1181	6	6	5.81E-07	4725	14	14	6585	18.0
113099c	844	powdered	1:1	140					182	11	11	4.47E-05	474	33	33	1026	53.6
120199a	778	powdered	1:1	256					446	8	8	3.96E-06	3865	33	33	3865	33.0
120199b	718	powdered	1:1	197					607	8	8	2.45E-06	3585	25	25	3585	25.3
120299b	718	powdered	1:6	224					312	2	10	1.52E-05	3605	10	57	3605	9.5
120299c	718	powdered	1:5	188					476	3	14	1.11E-05	3615	10	50	3615	10.0
120399a	718	powdered	1:3	198					954	4	13	3.72E-06	9005	16	47	9005	15.8
120699a	718	powdered	1:4	192					560	3	13	8.32E-06	5475	13	53	5475	13.3
120699b	717	powdered	1:2	207					606	3	7	1.95E-06	9185	18	36	9185	18.0
120699c	717	powdered	1:2	216					746	5	10	3.41E-06	6865	20	40	9235	23.2
120799a	718	powdered	1:1	190					954	7	7	1.04E-06	10805	29	29	10805	28.7
120799b	828	powdered	1:3	138					180	5	14	4.79E-05	676	14	43	3695	28.9
120799c	828	powdered	1:2	145					183	6	12	3.69E-05	2085	33	66	3645	42.3
120999a	828	powdered	1:4	203					212	5	20	1.17E-04	1635	22	87	2465	23.7
120999b	827	powdered	2:1	190					190	8	4	5.19E-06	5485	88	44	5485	88.0
121399a	830	powdered	1:5	154					188	4	21	1.11E-04	848	14	68	3615	20.1
121399b	830	powdered	1:6	170					194	5	29	2.24E-04	890	15	87	1795	16.7
121599a	830	powdered	1:3	156					190	4	13	3.92E-05	2845	25	76	4595	25.3
121599b	830	powdered	1:3.5	164					178	4	13	4.73E-05	986	15	52	3635	24.3
121599c	829	powdered	1:4	182					224	7	29	1.84E-04	1575	24	97	1995	25.1
121699a	829	powdered	1:4.5	166					180	4	18	9.51E-05	941	15	67	3605	20.3
121699b	829	powdered	1:5	188					188	4	18	9.60E-05	934	13	67	2115	16.3

Expt #	Temp.	Mn_3O_4	ratio	$Time_T$	$Time_{ls}$	XNa_{ls}	XMn_{ls}	k_l	$Time_{sds}$	XNa_{sds}	XMn_{sds}	k_d	$Time_{df}$	XNa_{df}	XMn_{df}	T_f	XNa_f
12000a	830	small	1:1	300					300	11	11	1.51E-05	6000	71	71	28800	96.6
12100a	830	small	2:1	254					254	9	5	3.92E-06	3240	60	60	21720	100.0
12200a	830	small	3:1	261					261	11	3	1.88E-06	2820	60	20	15420	100.0
12900a	830	small	2:1	250					250	10	5	4.27E-06	2640	56	28	15240	97.6
12700a	830	medium	1:1	240	240	1	1	3.77E-05	4500	31	31	5.31E-06	30360	85	85	34500	87.0
40700a	830	medium	1:1	240	240	1	1	3.24E-05	4860	30	30	4.16E-06	22860	70	70	72900	91.2
12800a	830	medium	2:1	246	246	3	1	3.49E-05	2460	33	16	2.59E-06	10560	73	37	23970	98.5
33000a	830	medium	2:1	390	390	4	2	2.69E-05	3240	33	16	1.92E-06	13680	81	40	31320	99.2
12600a	830	medium	3:1	240	240	3	1	2.74E-05	1830	28	9	1.11E-06	8610	77	26	26700	100.0
40600a	830	medium	3:1	225	225	4	1	2.54E-05	2160	32	10	1.09E-06	9720	81	27	22320	99.8
20200a	830	large	1:1	230	230	1	1	2.16E-05	10320	38	38	4.25E-06	26880	70	70	75960	87.3
20100a	830	large	2:1	234	234	1	0	1.42E-05	6240	34	17	1.12E-06	22170	78	78	44400	94.4
13100a	830	large	3:1	230	230	2	0	1.17E-05	6150	42	14	8.02E-07	1623	85	85	30630	100.0
20600a	743	small	1:1	314					9300	28	28	1.49E-06	44040	61	61	85260	69.3
20500a	743	small	2:1	255					3000	15	7	2.83E-07	87960	85	42	96420	98.5
20400a	743	small	3:1	236					670	8	2	1.66E-07	45000	72	24	76800	82.1
20700a	743	medium	1:1	285					15240	15	15	4.31E-07	40000	32	32	52140	29.0
32700b	871	large	1:1	446					814	71	71	3.67E-04	1241	96	96	1830	98.9
32700c	897	large	1:1	314					547	65	65	5.24E-04	847	94	94	1800	98.2
32700d	922	large	1:1	288					461	71	71	8.20E-04	650	96	96	1560	100.1
32800a	946	large	1:1	261					384	73	73	1.10E-03	499	94	94	1229	99.1

APPENDIX V – REDUCED DATA FROM MATERIAL BALANCES

The data used to determine efficiencies and recoveries are summarized in the following table. Abbreviations are listed first.

Expt #	Experiment reference number, corresponds to the date.
Temp.	Isothermal reaction temperature, °C.
Mn_3O_4	Particle size for Mn_3O_4 used in experiment; large, medium, small, or powdered.
ratio	Initial molar ratio of reactants; Mn_3O_4:Na_2CO_3
Na_2CO_{3wt}	Weight of Na_2CO_3 used in direct causticizing reaction, g.
Mn_3O_{4wt}	Weight of Mn_3O_4 used in direct causticizing reaction, g.
wt. Loss	Weight loss after completion of direct causticizing reaction, g.
Eff_{DC}	Direct causticizing efficiency as defined by Equation 35, %.
$NaOH_H$	NaOH from titration of hydrolysis filtrate, mmol.
Eff_H	Hydrolysis efficiency as defined by Equation 36, %.
Na_2CO_{3H}	Na_2CO_3 from titration of hydrolysis filtrate, mmol.
Eff_o	Overall process efficiency as defined by Equation 37, %.
TSR	Total sodium recovery as defined by Equation 38, %.
wt. $recov_H$	Total solid material recovered from hydrolysis, g.
TMR	Total manganese recovery as defined by Equation 39, %.

Expt #	Temp.	Mn_3O_4	ratio	Na_2CO_{3wt}	Mn_3O_{4wt}	wt. Loss	Eff_{DC}	$NaOH_H$	Eff_H	Na_2CO_{3H}	Eff_O	TSR	$wt.\ recov_H$	TMR
40700a	830	medium	1:1	0.2519	0.5436	0.0954	91.2%	4.140	95.5%	0.311	86.9%	100.2%	0.5447	100.2%
33000a	830	medium	2:1	0.1527	0.6575	0.0629	99.2%	2.902	101.8%	0.000	100.0%	100.7%	0.6689	101.7%
40600a	830	medium	3:1	0.1101	0.7123	0.0456	99.8%	1.961	94.7%	0.056	94.6%	99.8%	0.7057	99.1%
32700b	871	large	1:1	0.2633	0.5678	0.1079	98.7%	4.787	97.7%	0.154	94.0%	102.6%	0.5757	101.4%
32700c	897	large	1:1	0.2620	0.5656	0.1067	98.1%	4.601	94.9%	0.164	93.3%	99.7%	0.5758	101.8%
32700d	922	large	1:1	0.2624	0.5666	0.1091	100.2%	4.855	97.9%	0.000	100.0%	98.1%	0.5624	99.3%
32800a	946	large	1:1	0.2621	0.5662	0.1077	99.0%	4.887	99.8%	0.000	100.0%	98.8%	0.5628	99.4%

APPENDIX VI – XRD REFERENCE VALUES

The reference pattern data for relevant materials are included below. Tabulated data contains the 2θ angle along with relative intensities. Two sample holders were used for the XRD spectrum collection. The normal holder exhibited peaks at 2θ angles of 42.8, 49.8, and 73.2°. The low background holder had a peak at 44.8°.

Na_2CO_3 Angle	01-1166 Rel. Int	**Mn_3O_4** Angle	24-0734 Rel. Int.	**$NaMnO_2$** Angle	25-0844 Rel. Int.	**Na_2SO_4** Angle	08-0031 Rel. Int.
30.255	8	20.948	30	16.416	35	21.771	60
32.281	12	33.690	40	39.765	30	23.103	30
35.205	80	36.203	17	42.970	18	26.469	90
36.611	2	37.736	85	44.107	85	27.545	90
38.723	20	42.191	100	50.027	100	29.810	80
40.276	60	42.622	20	63.839	3	37.288	100
41.270	60	44.441	20	68.919	60	39.797	90
44.580	100	52.138	20	77.764	14	42.677	10
46.886	40	53.284	1	80.178	6	44.382	80
48.486	60	58.611	7			47.332	30
50.204	4	59.686	25			48.486	20
52.608	14	63.512	10			49.951	40
54.650	40	66.137	8			50.460	30
56.866	40	69.208	25			50.980	40
58.568	2	70.850	50			51.511	30
60.010	4	71.830	2			54.409	80
63.130	25	74.899	3			56.965	60
64.824	12	76.837	20			60.987	30
67.084	12	77.764	3			62.000	80
69.521	25	80.590	4			63.923	30
72.158	8					66.573	10
74.431	16					67.131	30
76.243	6					67.700	20
78.155	4					69.018	70
80.178	8					70.083	70

MnO_2 Angle	30-0820 Rel. Int.	**Mn_2O_3** Angle	24-0508 Rel. Int.	**MnO** Angle	07-0230 Rel. Int.
24.493	1	21.930	1	40.800	30
43.417	65	26.932	18	47.490	100
47.558	2	33.149	1	69.470	60
49.701	35	38.449	100	83.827	20
66.160	100	41.687	2		
79.491	40	44.699	11		
		47.576	1		
		50.321	1		
		52.978	9		
		55.546	1		
		58.005	10		
		62.758	2		
		65.074	27		
		67.353	2		
		69.592	1		
		71.765	2		
		73.924	1		
		76.094	4		
		78.182	11		
		80.296	3		

APPENDIX VII – DATA ACQUISITION PROGRAM

The data acquisition program used a graphical interface to construct the program. Screen shots of the program output, along with the programming interface are included. This is followed by a detailed description of each block shown in the programming interface.

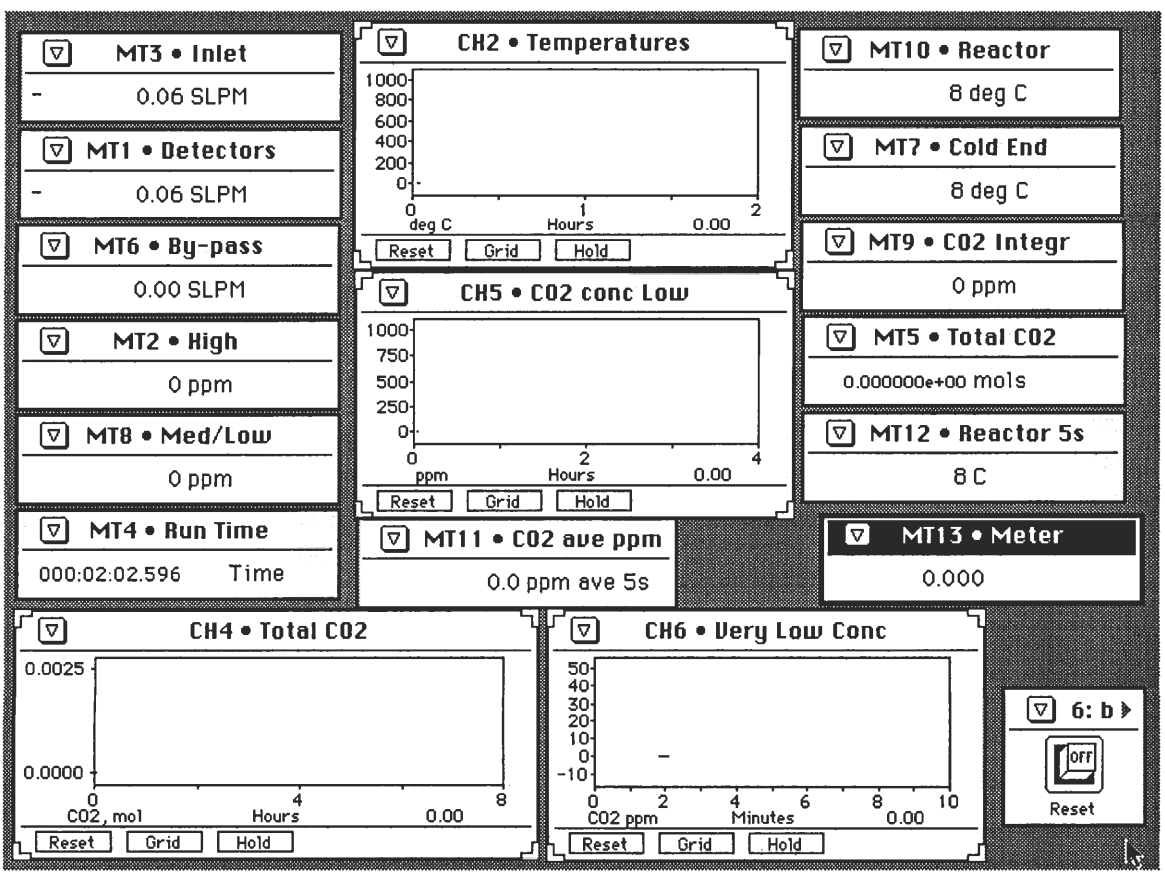

Figure 78 Screen capture of data acquisition program output screen.

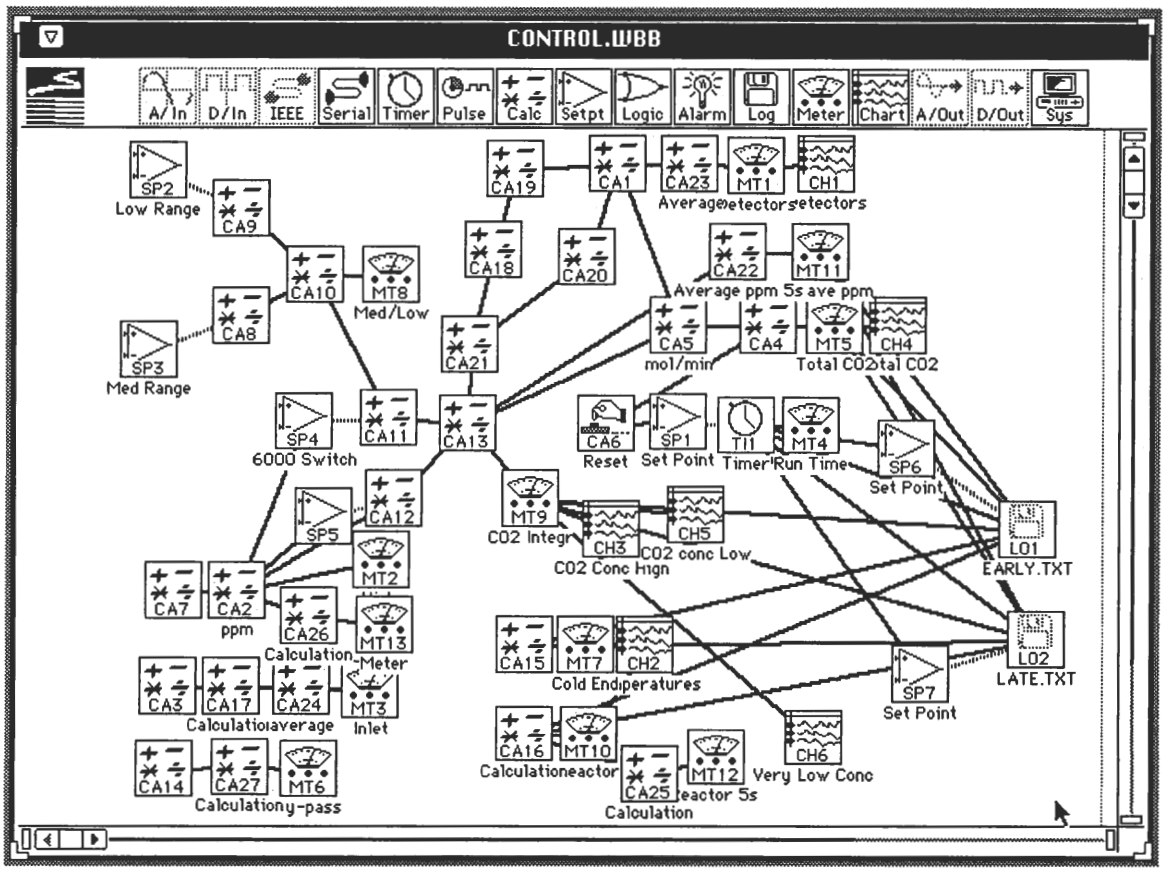

Figure 79 Screen capture of graphical programming interface. Analog input blocks are not shown.

Worksheet Name:	DATA.WBB
Hardware list:	
Name AIs AOs DIOs CTs DIs DOs	
STI WorkMate(tm) 8 2 8 1 0 0	
Maximum icons:	175
Grid size:	16
Snap to grid:	< disabled >
Report Unsynch:	< disabled >
Fast Mode:	< disabled >
Fast Mode samples:	800
Fast Mode rate:	0.0 Milliseconds
Trigger level:	-10.0
Trigger source:	Positive
Trigger slope:	Analog
Trigger mode:	None
Pre-trigger samples:	0
Com ports:	2

Port:	COM 1
Baud rate:	9600
Data bits:	8
Stop bits:	1
Duplex:	Half
Parity:	None
XonXoff:	< disabled >
Echo wait:	< disabled >
Line delay:	< disabled >

Port:	COM 2
Baud rate:	9600
Data bits:	8
Stop bits:	1
Duplex:	Half
Parity:	None
XonXoff:	< disabled >
Echo wait:	< disabled >
Line delay:	< disabled >

IEEE: < disabled >

Type: Analog Input

Name:	AI:1 CO2 High
Card Type:	STI WorkMate(tm)

Channel Number: 1
Range: 200 mV
Resolution: Auto (5us)
Output Type: Voltage
Sample rate: 120.0 Hertz
Fast Mode: < disabled >
Inputs:
< None >
Outputs:
CA7

Name: AI:2 CO2
Card Type: STI WorkMate(tm)
Channel Number: 2
Range: +|-100 mV
Resolution: Auto (5us)
Output Type: Voltage
Sample rate: 120.0 Hertz
Fast Mode: < disabled >
Inputs:
< None >
Outputs:
CA8 CA9

Name: AI:3 Range
Card Type: STI WorkMate(tm)
Channel Number: 3
Range: +|-5 V
Resolution: Auto (5us)
Output Type: Voltage
Sample rate: 0.5 Seconds
Fast Mode: < disabled >
Inputs:
< None >
Outputs:
SP2 Low Range SP3 Med Range

Name: AI:4 Inlet
Card Type: STI WorkMate(tm)
Channel Number: 4
Range: +|-5 V
Resolution: Auto (5us)
Output Type: Voltage
Sample rate: 1.0 Seconds
Fast Mode: < disabled >
Inputs:
< None >
Outputs:
CA3

Name: AI:5 Detectors
Card Type: STI WorkMate(tm)
Channel Number: 5
Range: +|-5 V
Resolution: Auto (5us)
Output Type: Voltage
Sample rate: 0.1 Seconds
Fast Mode: < disabled >
Inputs:
< None >
Outputs:
CA19

Name: AI:6 Cold End
Card Type: STI WorkMate(tm)
Channel Number: 6
Range: K Type T/C +|-50 mV
Resolution: Auto (5us)
Output Type: Celcius
Sample rate: 1.0 Seconds
Fast Mode: < disabled >
Inputs:
< None >
Outputs:
CA15

Name: AI:7 Reactor
Card Type: STI WorkMate(tm)
Channel Number: 7
Range: K Type T/C +|-50 mV
Resolution: Auto (5us)
Output Type: Celcius
Sample rate: 1.0 Seconds
Fast Mode: < disabled >
Inputs:
< None >
Outputs:
CA16 Calculation

Name: AI:8 By-pass
Card Type: STI WorkMate(tm)
Channel Number: 8
Range: +|-5 V
Resolution: Auto (5us)
Output Type: Voltage
Sample rate: 10.0 Hertz
Fast Mode: < disabled >
Inputs:
< None >
Outputs:
CA14

Type: Timer_____

Name: TI1 Timer
Inputs:
SP1 Set Point
Outputs:
MT4 Run Time SP6 Set Point
SP7 Set Point
LO1 EARLY.TXT LO2
LATE.TXT

Type: Calculation_____

Name: CA1
Function: X + Y
X input: CA19
Y input: CA20
"a" constant: 0.0
"b" constant: 0.0
"c" constant: 0.0
Inputs:
CA19 CA20
Outputs:
CA5 mol/min CA23 Average

Name: CA2 ppm
Function: aX + bY
X input: CA7
Y input: 0.0
"a" constant: 1.0e+06
"b" constant: 0.0
"c" constant: 0.0
Inputs:
CA7
Outputs:
MT2 High SP4 6000 Switch SP5
CA12 CA26 Calculation

Name: CA3
Function: aX + bY + c
X input: AI:4 Inlet
Y input: 0.0
"a" constant: 2.0
"b" constant: 0.0
"c" constant: 0.0
Inputs:
AI:4 Inlet
Outputs:
CA17 Calculation

Name: CA4
Function: Integral X dt
X input: CA5 mol/min
Y input: CA6 Reset
"a" constant: 0.0
"b" constant: 0.0
"c" constant: 0.0
Inputs:
CA5 mol/min CA6 Reset
Outputs:
MT5 Total CO2

Name: CA5 mol/min
Function: aX * bY
X input: CA1
Y input: CA13
"a" constant: 0.0166667
"b" constant: 4.46428e-08
"c" constant: 0.0
Inputs:
CA1 CA13
Outputs:
CA4

Name: CA6 Reset
Function: Button(a:type)
X input: 0.0
Y input: 0.0
"a" constant: 2.0
"b" constant: 0.0
"c" constant: 0.0
Inputs:
< None >
Outputs:
SP1 Set Point CA4

Name: CA7
Function: Ave(X) for last (a) seconds
X input: AI:1 CO2 High
Y input: 0.0
"a" constant: 2.0
"b" constant: 0.0
"c" constant: 0.0
Inputs:
AI:1 CO2 High
Outputs:
CA2 ppm

Name: CA8
Function: aX * bY
X input: AI:2 CO2
Y input: SP3 Med Range
"a" constant: 1.0
"b" constant: 1.0
"c" constant: 0.0
Inputs:
AI:2 CO2 SP3 Med Range
Outputs:
CA10

Name: CA9
Function: aX * bY
X input: AI:2 CO2
Y input: SP2 Low Range
"a" constant: 1.0
"b" constant: 1.0
"c" constant: 0.0
Inputs:
AI:2 CO2 SP2 Low Range
Outputs:
CA10

Name: CA10
Function: aX + bY
X input: CA9
Y input: CA8
"a" constant: 20000.0
"b" constant: 60000.0
"c" constant: 0.0
Inputs:
CA9 CA8
Outputs:
MT8 Med/Low CA11

Name: CA11
Function: aX * bY
X input: CA10
Y input: SP4 6000 Switch
"a" constant: 1.0
"b" constant: 1.0
"c" constant: 0.0
Inputs:
CA10 SP4 6000 Switch
Outputs:
CA13

Name: CA12
Function: aX * bY
X input: CA2 ppm
Y input: SP5
"a" constant: 1.0
"b" constant: 1.0
"c" constant: 0.0
Inputs:
CA2 ppm SP5
Outputs:
CA13

Name: CA13
Function: X + Y
X input: CA11
Y input: CA12
"a" constant: 0.0
"b" constant: 0.0
"c" constant: 0.0
Inputs:
CA11 CA12
Outputs:
CA5 mol/min MT9 CO2 Integr CA21
CA22 Average ppm 5s

Name: CA14
Function: aX + bY + c
X input: AI:8 By-pass
Y input: 0.0
"a" constant: 2.0
"b" constant: 0.0
"c" constant: 0.0
Inputs:
AI:8 By-pass
Outputs:
CA27 Calculation

Name: CA15
Function: aX + bY + c
X input: AI:6 Cold End
Y input: 0.0
"a" constant: 1.0
"b" constant: 0.0
"c" constant: 8.0
Inputs:
AI:6 Cold End
Outputs:
MT7 Cold End LO1
EARLY.TXT LO2 LATE.TXT

Name: CA16 Calculation
Function: aX + bY + c
X input: AI:7 Reactor
Y input: 0.0
"a" constant: 1.0
"b" constant: 0.0
"c" constant: 8.0
Inputs:
AI:7 Reactor
Outputs:
MT10 Reactor CA25 Calculation
LO1 EARLY.TXT
LO2 LATE.TXT

Name: CA17 Calculation
Function: aX + bY + c
X input: CA3
Y input: 0.0
"a" constant: 1.0435
"b" constant: 0.0
"c" constant: -0.0563
Inputs:
CA3
Outputs:
CA24 average

Name: CA18
Function: aX + bY + c
X input: CA21
Y input: 0.0
"a" constant: -0.458
"b" constant: 0.0
"c" constant: 1.0089
Inputs:
CA21
Outputs:
CA19

Name: CA19
Function: aX * bY
X input: AI:5 Detectors
Y input: CA18
"a" constant: 2.0
"b" constant: 1.0
"c" constant: 0.0
Inputs:
AI:5 Detectors CA18
Outputs:
CA1

Name: CA20
Function: aX + bY + c
X input: CA21
Y input: 0.0
"a" constant: 0.208
"b" constant: 0.0
"c" constant: -0.0574
Inputs:
CA21
Outputs:
CA1

Name: CA21
Function: aX + bY
X input: CA13
Y input: 0.0
"a" constant: 1.0e-06
"b" constant: 0.0
"c" constant: 0.0
Inputs:
CA13
Outputs:
CA18 CA20

Name: CA22 Average ppm 5s
Function: Ave(X) for last (a) seconds
X input: CA13
Y input: 0.0
"a" constant: 5.0
"b" constant: 0.0
"c" constant: 0.0
Inputs:
CA13
Outputs:
MT11 CO2 ave ppm

Name: CA23 Average
Function: Ave(X) for last (a) seconds
X input: CA1
Y input: 0.0
"a" constant: 5.0
"b" constant: 0.0
"c" constant: 0.0
Inputs:
CA1
Outputs:
MT1 Detectors

Name: CA24 average
Function: Ave(X) for last (a) seconds
X input: CA17 Calculation
Y input: 0.0
"a" constant: 5.0
"b" constant: 0.0
"c" constant: 0.0
Inputs:
CA17 Calculation
Outputs:
MT3 Inlet

Name: CA25 Calculation
Function: Ave(X) for last (a) seconds
X input: CA16 Calculation
Y input: 0.0
"a" constant: 5.0
"b" constant: 0.0
"c" constant: 0.0
Inputs:
CA16 Calculation
Outputs:
MT12 Reactor 5s

Name: CA26 Calculation
Function: Ave(X) for last (a) seconds
X input: CA2 ppm
Y input: 0.0
"a" constant: 5.0
"b" constant: 0.0
"c" constant: 0.0
Inputs:
CA2 ppm
Outputs:
MT13 Meter

Name: CA27 Calculation
Function: Ave(X) for last (a) seconds
X input: CA14
Y input: 0.0
"a" constant: 5.0
"b" constant: 0.0
"c" constant: 0.0
Inputs:
CA14
Outputs:
MT6 By-pass

Type: Set Point_____

Name: SP1 Set Point
Function: X < Y
X input: CA6 Reset
Y input: 0.5
Dead Band: 0.0
Inputs:
CA6 Reset
Outputs:
TI1 Timer

Name: SP2 Low Range
Function: X < Y
X input: AI:3 Range
Y input: 2.5
Dead Band: 0.0
Inputs:
AI:3 Range
Outputs:
CA9

Name: SP3 Med Range
Function: X > Y
X input: AI:3 Range
Y input: 2.5
Dead Band: 0.0
Inputs:
AI:3 Range
Outputs:
CA8

Name: SP4 6000 Switch
Function: X < Y
X input: CA2 ppm
Y input: 6000.0
Dead Band: 0.0
Inputs:
CA2 ppm
Outputs:
CA11

Name: SP5
Function: X > Y
X input: CA2 ppm
Y input: 6000.0
Dead Band: 0.0
Inputs:
CA2 ppm
Outputs:
CA12

Name: SP6 Set Point
Function: X < Y
X input: TI1 Timer
Y input: 1500.0
Dead Band: 0.0
Inputs:
TI1 Timer
Outputs:
LO1 EARLY.TXT

Name: SP7 Set Point
Function: X > Y
X input: TI1 Timer
Y input: 1500.0
Dead Band: 0.0
Inputs:
TI1 Timer
Outputs:
LO2 LATE.TXT

Type: Log_____

Name: LO1 EARLY.TXT
Log Status: < disabled >
Sample Rate: 5.0 Seconds
Gate: SP6 Set Point
Data Format:
Heading: < None >
File Path: C:\WB
File Name: EARLY.TXT
Date Stamp: < disabled >
Time Stamp: < disabled >
Inputs:
TI1 Timer CA16 Calculation
MT5 Total CO2
CA15 MT9 CO2 Integr
MT11 CO2 ave ppm
SP6 Set Point
Outputs:
< None >

Name: LO2 LATE.TXT
Log Status: < disabled >
Sample Rate: 5.0 Minutes
Gate: SP7 Set Point
Data Format:
Heading: < None >
File Path: C:\WB
File Name: LATE.TXT
Date Stamp: < disabled >
Time Stamp: < disabled >
Inputs:
TI1 Timer CA16 Calculation
MT5 Total CO2
CA15 MT9 CO2 Integr
MT11 CO2 ave ppm
SP7 Set Point
Outputs:
< None >

Type: Meter_____

Name: MT1 Detectors
Output Type: Fixed Point
Units: SLPM
Integer: 7
Decimal: 2
Inputs:
CA23 Average
Outputs:
CH1 Detectors

Name: MT2 High
Output Type: Fixed Point
Units: ppm
Integer: 9
Decimal: 0
Inputs:
CA2 ppm
Outputs:
< None >

Name: MT3 Inlet
Output Type: Fixed Point
Units: SLPM
Integer: 7
Decimal: 2
Inputs:
CA24 average
Outputs:
< None >

Name: MT4 Run Time
Output Type: Time
Units: < None >
Integer: 6
Decimal: 3
Inputs:
TI1 Timer
Outputs:
< None >

Name: MT5 Total CO2
Output Type: Exponential
Units: mols
Integer: 3
Decimal: 6
Inputs:
CA4
Outputs:
CH4 Total CO2 LO1 EARLY.TXT
LO2 LATE.TXT

Name: MT6 By-pass
Output Type: Fixed Point
Units: SLPM
Integer: 7
Decimal: 2
Inputs:
CA27 Calculation
Outputs:
< None >

Name: MT7 Cold End
Output Type: Fixed Point
Units: deg C
Integer: 9
Decimal: 0
Inputs:
CA15
Outputs:
CH2 Temperatures

Name: MT8 Med/Low
Output Type: Fixed Point
Units: ppm
Integer: 9
Decimal: 0
Inputs:
CA10
Outputs:
< None >

Name: MT9 CO2 Integr
Output Type: Fixed Point
Units: ppm
Integer: 9
Decimal: 0
Inputs:
CA13
Outputs:
CH3 CO2 Conc High CH5 CO2
conc Low CH6 Very Low Conc
LO1 EARLY.TXT LO2
LATE.TXT

Name: MT10 Reactor
Output Type: Fixed Point
Units: deg C
Integer: 9
Decimal: 0
Inputs:
CA16 Calculation
Outputs:
CH2 Temperatures

Name: MT11 CO2 ave ppm
Output Type: Fixed Point
Units: ppm ave 5s
Integer: 8
Decimal: 1

Inputs:
CA22 Average ppm 5s
Outputs:
LO1 EARLY.TXT LO2 LATE.TXT

Name: MT12 Reactor 5s
Output Type: Fixed Point
Units: C
Integer: 9
Decimal: 0
Inputs:
CA25 Calculation
Outputs:
< None >

Name: MT13 Meter
Output Type: Fixed Point
Units: < None >
Integer: 6
Decimal: 3
Inputs:
CA26 Calculation
Outputs:
< None >

Type: Chart_____

Name: CH1 Detectors
Chart Color: White
X Axis Label: Minutes
X Axis Min: 0.0
X Axis Max: 10.0
Y Axis Label: SLPM
Y Axis Min: 0.0
Y Axis Max: 2.0
Inputs:
MT1 Detectors
Outputs:
< None >

Name: CH2 Temperatures
Chart Color: White
X Axis Label: Hours
X Axis Min: 0.0
X Axis Max: 2.0
Y Axis Label: deg C
Y Axis Min: 0.0
Y Axis Max: 1000.0
Inputs:
MT7 Cold End MT10 Reactor
Outputs:
< None >

Name: CH3 CO2 Conc High
Chart Color: White
X Axis Label: Hours
X Axis Min: 0.0
X Axis Max: 2.0
Y Axis Label: ppm
Y Axis Min: 0.0
Y Axis Max: 1.0e+05
Inputs:
MT9 CO2 Integr
Outputs:
< None >

Name: CH4 Total CO2
Chart Color: White
X Axis Label: Hours
X Axis Min: 0.0
X Axis Max: 8.0
Y Axis Label: CO2, mol
Y Axis Min: 0.0
Y Axis Max: 0.0025
Inputs:
MT5 Total CO2
Outputs:
< None >

Name: CH5 CO2 conc Low
Chart Color: White
X Axis Label: Hours
X Axis Min: 0.0
X Axis Max: 4.0
Y Axis Label: ppm
Y Axis Min: 0.0
Y Axis Max: 1000.0
Inputs:
MT9 CO2 Integr
Outputs:
< None >

Name: CH6 Very Low Conc
Chart Color: White
X Axis Label: Minutes
X Axis Min: 0.0
X Axis Max: 10.0
Y Axis Label: CO2 ppm
Y Axis Min: -10.0
Y Axis Max: 50.0
Inputs:
MT9 CO2 Integr
Outputs:
< None >